University of Stavanger

Faculty of Science and Technology

MASTER'S THESIS

Study program/Specialization: Master of Science in Petroleum Engineering, 5-year Program / Reservoir Engineering	Spring semester, 2016 Open
Writer: Håkon Sunde Bakka	…… (Writer's signature)
Faculty supervisor: Merete Vadla Madland External supervisor(s): Serap Ozoglu-Topdemir	
Thesis title: Examination of Dynamic Stress and Conductivity in the Eldfisk Chalk Field	
Credits (ECTS): 30	
Key words: Pressure Transient Analysis Minimum Horizontal Stress Closure Stress Fracture Initiation Pressure Fracture Propagation Pressure Conductivity Chalk Water Weakening	Pages: 109 + enclosure: 3 Stavanger, …….. Date/year

Examination of
Dynamic Stress and Conductivity
in the
Eldfisk Chalk Field

By

Håkon Sunde Bakka

Master Thesis

Presented to the Faculty of Science and Technology

The University of Stavanger

The University of Stavanger

May 2016

I. Abstract

This thesis work has been conducted in cooperation with ConocoPhillips Norway and looks at the stress development in the Eldfisk chalk reservoir. High injection pressures due to the relatively low permeabilities of chalk reservoirs are known to form tensile fractures (Rod and Jørgensen 2005). Tensile fractures may lead to bypassing of hydrocarbons and early water breakthrough in producers. Knowing when and if tensile fractures will form is therefore important to ensure maximum recovery.

Analysis of 32 minifrac falloff tests have shown that the Eldfisk minimum principal stress (σ_h) conforms to a linear trend as a function of the pore pressure gradient. A linear regression model has been proposed for the closure gradient, with a slope of 0.72 and intercept of 0.31 psi/ft. A linear trend is seen for the closure stress data despite significant pore collapse and inelastic deformation, suggesting that plastically deformed chalk continues to behave partially elastic.

Analysis of 10 minifrac Step Rate Tests have shown that the additional pressure required to initiate a fracture is on average 600 psi above the closure stress. The difference is independent of pore pressure, and indicates relatively uniform redistribution of stress around the horizontal wellbores.

Pressure Transient Analysis of minifrac Step Rate Tests have shown that valuable information on fracture mechanics can be extracted from short test durations. The results indicate that completed zone lengths will influence the fracture development, and suggests that varying fracture half-length may be a consequence in wells with large variation in perforation zone lengths.

Time-lapse Pressure Transient Analysis of two injection wells on the Eldfisk Field (B-22 and B-8 B) has indicated no tensile fracture growth despite high injection rates and pressures. However, up to ~4-times increase in reservoir conductivity was seen in the area around B-8 B, while no significant change was seen around B-22. A conceptual model has been proposed that uses the minimum principal stress to explain the difference in B-8 B and B-22 behavior. The increase in conductivity around B-8 may be a result of natural fracture network expansion when the injection pressures exceed the closure stress. B-22 sees no change as injection pressures are below the local closure stress. Stress arching is believed to be important as it reduced the closure stress on the crest and increases the closure stress on the flanks.

Chemical alterations induced as part of a water weakening mechanism are proposed to influence the conductivity development in areas around injectors. Core experiments indicate that seawater flowing through the natural fracture networks could lead to significant chemical alterations in and around the fractures (Madland et al. 2015). These alterations may lead to partial filling of the fractures, influencing the fracture permeability and reducing the stress dependency of the fracture network conductivity.

II. Acknowledgements

Firstly, I would like to thank Serap Ozoglu-Topdemir, my supervisor at ConocoPhillips Norway, for her dedication, support and interest in this thesis work. A special thanks to her for proposing the project, and always being open and available for discussions. The feedback and discussions have been greatly appreciated.

I would also like to thank Edvard Omdal at ConocoPhillips Norway, for his geomechanics input and interest. I have benefitted greatly from our discussions during the work with this thesis. A special thanks for his contribution to help bridge the gap between field and lab experience.

My thanks also go out to Rune Tveit for arranging this thesis project, and the rest of the staff at ConocoPhillips for their interest and support.

I would also like to thank my faculty supervisor, Professor Merete Madland, for her feedback and support. Her feedback has been instrumental to the quality of this final report. I would especially like to thank her for contributing with lab experience and understanding of the water weakening process in chalk.

I greatly appreciated that ConocoPhillips Scandinavia AS and the PL018 license partners Total E&P Norge AS, Eni Norge AS, Statoil Petroleum AS and Petoro AS gave permission to publish this thesis. The views presented here are those of the Author and do not necessarily represent the views of ConocoPhillips Norway.

My thanks also go out to my family, for their continued support through this project period.

Stavanger 22.05.2016

Håkon Sunde Bakka

III. Objectives

The objectives of this thesis are to

1. Use pressure data from minifrac injection tests on the Eldfisk Field to evaluate changes in minimum horizontal stress as a function of pore pressure.
2. Evaluate fracture mechanics in chalk, and assess mechanisms controlling conductivity and fracture development around water injection wells.

Table of Contents

1 Introduction

1.1 The Project

This thesis examines the fracture and closure stress development in the Eldfisk chalk field as a function of pore pressure. The determined stress correlations are used to develop a conceptual model for permeability development around water injectors in naturally fractured chalk reservoirs. The study also shows the application of Pressure Transient Analysis techniques for evaluation of tensile fracture development in minifrac tests.

The study is motivated by the value created through 40 years of hydrocarbon production from North Sea chalk fields. Research into deformation behavior of chalk has become of primary interest for operator companies due to the unique production and compaction challenges associated with chalk reservoirs (Omdal 2010). Producing from and injecting into high porosity naturally fractured low permeability chalk, has proven to be complicated. From a water injection perspective, the primary issue is uncontrolled fracture growth and bypassing of hydrocarbons. Rod and Jørgensen (2005) showed that in non-structurally trapped low fracture density chalk, water injection fracturing can be controlled to improve and accelerate hydrocarbon recovery. This motivates a study into the mechanics controlling fracture and conductivity growth and development around Eldfisk injection wells, with the aim of improving the field production strategy.

1.2 The Report

This thesis report outlines the most important results of the project. After a brief introduction to the Eldfisk Field in Section 1.3, Section 2 will outline the relevant theories applied and discussed in this thesis. Section 3 highlights the methodology applied in the project, emphasizing where the analysis may deviate from more traditional procedures. Sections 4 and 5 show and discuss the results of the analysis, respectively, where some results are discussed in the results section (4) when most appropriate. The main conclusions and results are summarized in Section 6, while Sections 7 and 8 contain the reference list and appendix, respectively.

1.3 The Eldfisk Field

1.3.1 Development

The Eldfisk Field is a chalk field within the PL018 license area. The field is operated by ConocoPhillips Scandinavia AS with partners Total E&P Norge AS, Eni Norge AS, Statoil Petroleum AS and Petoro AS. The field started production in 1979 and was originally developed with 3 platforms, Eldfisk A, Eldfisk B and Eldfisk FTP (NPD 2016). Water injection started in 1999 with the installation of the Eldfisk E platform, following the successful waterflood implementation on the nearby Ekofisk Field in 1987. The

Eldfisk II redevelopment started production in 2015 after installation of the new Eldfisk S integrated wellhead and processing platform (NPD 2016).

1.3.2 Reservoir

The Eldfisk reservoir is a Paleocene to Late Cretaceous chalk reservoir in Ekofisk, Tor and Hod formations. The Ekofisk Formation is subdivided into Upper (EU), Middle (EM) and Lower (EL) zones, with improving reservoir properties from the EU downwards towards EL. The reservoir contains originally undersaturated oil with 131.2 mill Sm3 of recoverable oil volumes (NPD 2016). Initial reservoir pressure was 6850 psia at 9000 ft TVD SS, with reservoir temperature between 110 – 130 ^{o}C. The reservoir is characterized by high porosities and low matrix permeability, with natural fractures enhancing the flow capacity (NPD 2016). Porosities vary from 25% to 48%, with matrix permeabilities between 1 to 5 mD, and effective permeabilities between 1 to 15 mD (Wade et al. 1998). The reservoir shows extensive faulting which form high conductivity channels. The field consists of three reservoir structures, Alpha, Bravo and Eldfisk East (Figure 1.1) at depths between 8860 – 9500 ft TVD SS. The elongated structure of the field has dictated the development strategy, which is dominated by horizontal wells drilled northwest from the Alpha structure and southeast from the Bravo structure. The waterflooding pattern resembles a line drive with injectors drilled along the reservoir crest.

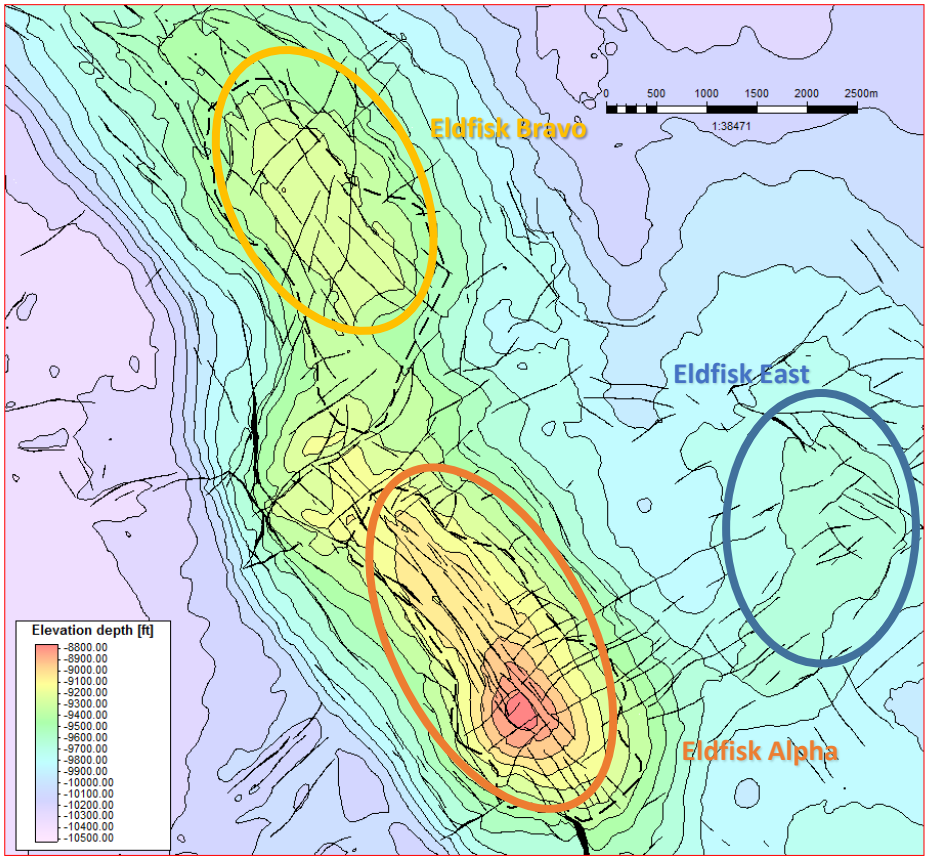

Figure 1.1: Structural map of the Eldfisk Field. The Alpha structure is to the south, the Bravo structure to the north and the Eldfisk East structure to the east.

2 Theory

2.1 Failure mechanics

2.1.1 Stress State – Mohr's-Circle

The stress state of any material in three dimensions (x,y,z) is described by a 3x3 stress tensor, with three normal stress components (σ) and six shear stress components (τ). Through symmetry arguments the number of shear components can be reduced to three, such that the stress state in any point P can be described by six stresses (Equation 2.1) (Fjær et al. 2008).

$$\begin{pmatrix} \sigma_x & \tau_{xy} & \tau_{xz} \\ \tau_{xy} & \sigma_y & \tau_{yz} \\ \tau_{xz} & \tau_{yz} & \sigma_z \end{pmatrix} \tag{2.1}$$

In any point P there will exist three principal stresses that describe the stress state of the material. The principal stresses are found through rotation of the coordinate system in Equation 2.1 such that there are no shear stresses in the material ($\tau = 0$) (Fjær et al. 2008). Projection of the stresses into the reoriented coordinate system gives the principal stresses, and is illustrated for two dimensions in Figure 2.1.

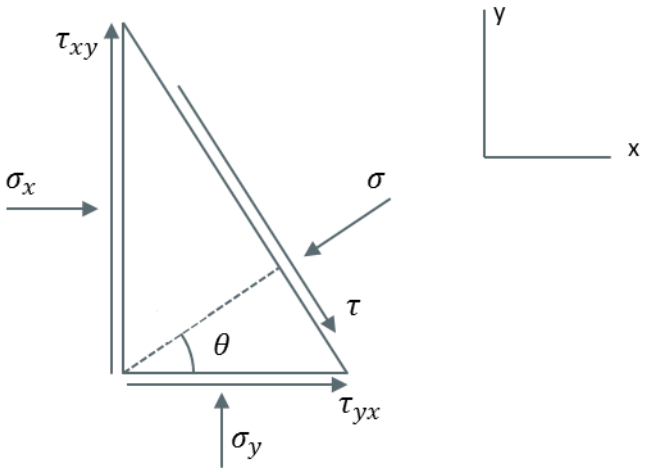

Figure 2.1: Illustration of stress rotation and force balance in two dimensions. The coordinate system is rotated by an angle Θ giving the projected stresses σ and τ. The principal stresses are given by σ when τ=0. All stresses are assumed positive.

The measured stress in a material is therefore a function of the measured stress direction (Figure 2.1), θ in two dimensions (2D). Equation 2.2 shows the equations fully describing the stress state of a material in two dimensions. These give rise to the Mohr's-circle (Figure 2.2), which describes the stress state in any point P as a function of principal stresses and coordinate direction.

$$\sigma = \frac{1}{2}(\sigma_1 + \sigma_2) + \frac{1}{2}(\sigma_1 - \sigma_2)\cos 2\theta$$

$$\tau = -\frac{1}{2}(\sigma_1 - \sigma_2)\sin 2\theta \tag{2.2}$$

σ = Projected normal stress

τ = Projected shear stress

$\sigma_{1/2}$ = Principal stresses (two directions in 2D geometry)

θ = Stress orientation in 2D

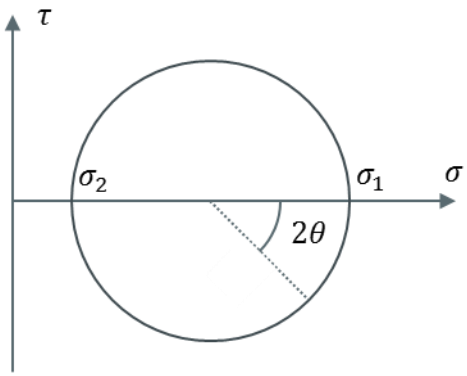

Figure 2.2: The Mohr's-circle is a schematic illustration of the stress state in a material. In a point P with principal stresses σ_1 and σ_2 the stress state lies on the circle outlined in the figure.

The Mohr's-circle concept can be expanded to three dimensions, but the stress state will then be described by a combination of circles. For a point P with the principal stress tensor given in Equation 2.3, the Mohr's-circle construction is given in Figure 2.3. The stress state is fully described by three circles between σ_1, σ_2 and σ_3, with the possible stress states in point P on the circles and in the area encapsulated by the circles (grey area in Figure 2.3) (Fjær et al. 2008). For the failure considerations in Section 2.1.3, it is important to note that maximum shear stress in three dimensions is given by the outer circle between σ_1 and σ_3.

$$\begin{pmatrix} \sigma_1 & 0 & 0 \\ 0 & \sigma_2 & 0 \\ 0 & 0 & \sigma_3 \end{pmatrix} \tag{2.3}$$

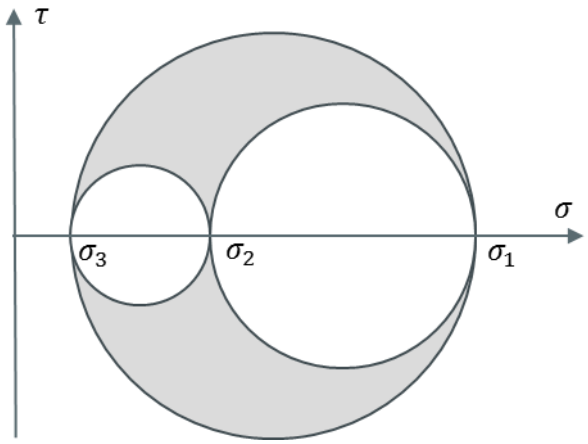

Figure 2.3: Mohr's-circle in three dimensions. The stress state in a point P is described by the circles and the grey area between the circles.

2.1.2 The Effective Stress Concept

The effective stress concept as described in Equation 2.4 was launched by Terzaghi (1923). The concept considers the impact of pore fluid pressure on the overall stress state of a porous media. As pore fluid pressure is increased, the effective stress felt by the rock matrix is reduced as more of the total stress is carried by the fluid. The degree to which the pore fluid pressure affects the effective stress is given by the effective stress coefficient (Biot coefficient, α) (Terzaghi 1923).

$$\sigma' = \sigma - \alpha \cdot p_f \tag{2.4}$$

σ' = Effective stress acting on the rock matrix

σ = Total stress

α = Biot stress coefficient

p_f = Pore fluid pressure

The effective stress concept is important, as it is the effective stresses that cause the rock material to deform.

2.1.3 Rock Failure Modes

Rock material subject to sufficiently large effective stresses will eventually fail. The type of failure will depend on the strength and characteristics of the rock material, as well as stress state at the point of failure (Fjær et al. 2008). Also, any material subject to stresses will deform, with the deformation and nature of deformation depending on the same state specific parameters as failure.

2.1.3.1 Elastic and Plastic Deformation

To understand rock failure, it is of primary importance to understand rock deformation. Simple experiments in triaxial or axial cells show three primary regions of rock deformation (Figure 2.4) (Fjær et al. 2008):

1. Elastic region
2. Ductile region
3. Brittle region

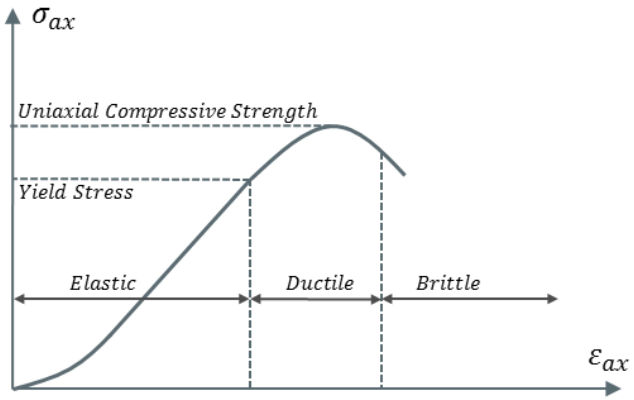

Figure 2.4: Regions of rock material deformation. Elastic deformation is fully reversible, while the ductile and brittle regions include varying degrees of plastic (irreversible) deformation. σ_{ax} is axial stress and ε_{ax} is axial strain.

In the elastic region all deformation is reversible and all deformation is removed if the load is removed. In the ductile region the rock undergoes permanent (plastic) deformation, and parts of the deformation will remain after the load is removed. In ductile deformation the rock still retains an ability to carry loads (Fjær et al. 2008). The brittle region is a region where the rocks ability to withstand stresses is rapidly reduced.

The deformation is generally described as either elastic or plastic, where elastic deformation is reversible and plastic deformation is permanent. In analysis of Stevns Klint high porosity chalk cores, Madland et al. (2009) showed that chalk may not have an elastic deformation phase, and can therefore only be described as a quasi-elastic material (Madland et al. 2009). This combined with load cycle analysis by Risnes and Nygaard (1999) which showed permanent deformation in the so-called “elastic” region of chalk deformation, indicates that chalk is a highly elasto-plastic material exhibiting both linear and non-linear deformation effects (Risnes and Nygaard 1999).

2.1.3.2 The Failure Envelope

In three dimensions the points indicating the stress state of a material at failure will form a three dimensional failure surface. The size of the failure surface will increase with increasing rock strength

(Fjær et al. 2008). For chalk, lab experiments have shown rock weakening with increase in porosity, indicating a smaller failure surface for higher porosity rocks (Teufel and Rhett 1992).

A $q - p'$ plot is similar to the Mohr's-circle plot and is used to represent the failure surface in two dimensions (Figure 2.5). The parameter q is called the generalized shear stress, and p' is identical to the mean effective stress following the effective stress concept described in Section 2.1.2 (Fjær et al. 2008).

$$q = \frac{1}{\sqrt{2}}\sqrt{(\sigma_1' - \sigma_2')^2 + (\sigma_2' - \sigma_3')^2 + (\sigma_1' - \sigma_3')^2}$$

$$p' = \frac{1}{3}(\sigma_1' + \sigma_2' + \sigma_3') \tag{2.5}$$

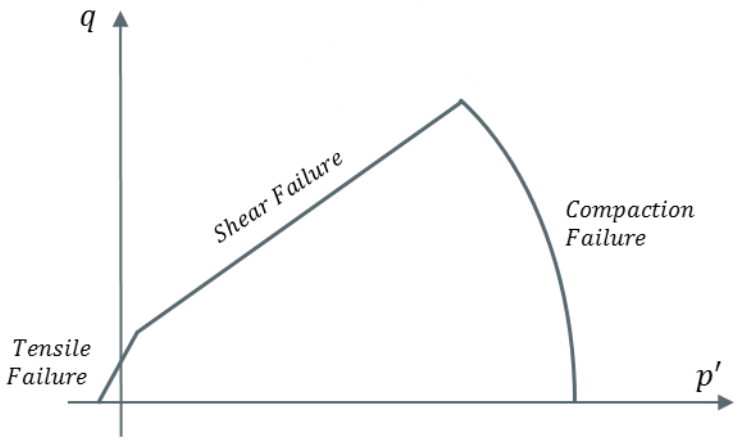

Figure 2.5: A q-p' plot illustrating the three different observed rock failure modes.

The three primary modes of failure are shown in the $q - p'$ plot in Figure 2.5:

1. Tensile failure
2. Shear failure
3. Compaction failure

2.1.3.3 Tensile Failure

Tensile failure is a key failure mode when considering hydraulic fracturing of reservoir rocks. Tensile failure occurs under extensional effective stresses, when the minimum effective stress (σ_3') in the rock reaches the tensile strength of the rock specimen (T_0) (Fjær et al. 2008) (Equation 2.6).

$$\sigma_3' = -T_0 \tag{2.6}$$

The failure mode is illustrated in Figure 2.6, and shows the extension of the failed rock. From the effective stress concept seen in Equation 2.4, extensional effective stresses (negative) occur when the

pore fluid pressure is high, and tensile failure is therefore an expected failure mode around high pressure injection wells.

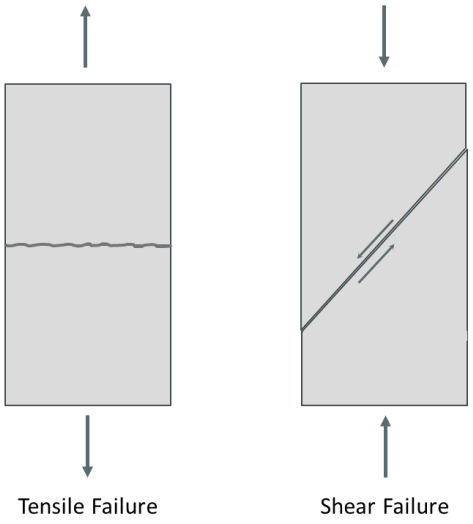

Figure 2.6: Illustration of tensile and shear failure mode. Tensile failure is a result of extensional effective stresses, while shear failure is a result of large differences in principal stresses. Both failure modes are important for the formation of subsurface fractures in reservoir rocks.

2.1.3.4 Shear Failure

Shear failure is also illustrated in Figure 2.6, and is a result of large differences in principal stresses. Shear failure occurs along a plane and is a common cause of faulting (Fjær et al. 2008). Figure 2.7 shows a Mohr's-circle diagram with a failure line indicating shear failure. As the radius of the outer Mohr's-circle is dictated by the difference between the minimum and maximum effective stress (σ_3' and σ_1', respectively), failure occurs at large differences in principal stresses. Shear failure was proposed by Teufel and Rhett (1991) as the key mechanism for fracture network development and permeability preservation in depleting chalk reservoirs. And Risnes (2001) showed that all chalk failure mechanisms (tensile, shear and compaction) can be attributed to shear failure or frictional sliding at grain contacts.

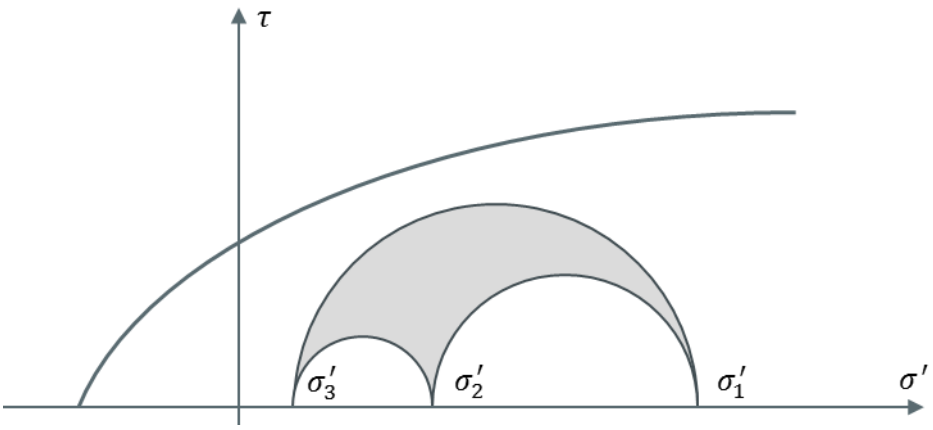

Figure 2.7: Illustration of shear failure line in a Mohr's-circle diagram. Shear failure will occur when the differences between the minimum and maximum effective stress become large enough for parts of the Mohr's-circle to exceed the failure line.

There are several different proposed shear failure criterions in the literature, for a comprehensive overview see Aadnoy and Looyeh (2011). A commonly referenced failure criterion is the Mohr-Columb criterion.

$$|\tau| = S_0 + \mu\sigma' \tag{2.7}$$

S_0 = Inherent shear strength (cohesion) (Fjær et al. 2008)

μ = Coefficient of internal friction

The cohesion is often used as a description of the bond strength between matrix grains, and the shear strength of a rock is seen to increase with increasing cohesion.

2.1.3.5 Compaction Failure

North Sea chalk reservoirs show remarkably high porosities at depth, with as much as 48% porosity at 2.9 km depth in the Ekofisk Field (Goulty 2003). Regular diagenesis would suggest far lower porosities, and Scholle (1977) attributed the high porosities to reservoir overpressure reducing the effective stress on the chalk matrix, and early oil invasion preventing chemical induration of the chalk (Omdal 2010). Due to the high initial porosity and relatively low degree of initial consolidation, compaction failure is an important failure mechanism for chalk reservoirs. Compaction failure is also known as pore collapse, and leads to a progressive decrease in porosity and increase in rock strength (Teufel and Rhett 1991, Teufel and Rhett 1992). Pore collapse is a result of an increase in mean effective stress acting on the rock matrix, and is therefore a consequence of reduced pore pressure (Equation 2.4) during production from chalk reservoirs. Pore collapse is of high importance as it leads to a progressive increase in the yield surface of the chalk during compaction (Figure 2.8). Progressive compaction failure may therefore lead to an overall increase in shear strength in failed parts of chalk reservoirs.

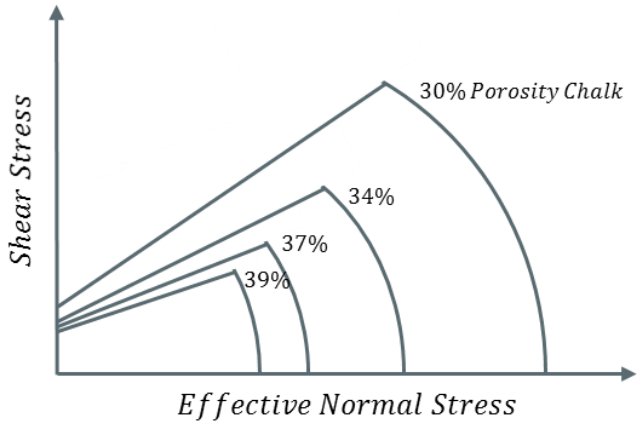

Figure 2.8: Illustration of the yield surface results determined for Ekofisk chalk by Teufel and Rhett (1991). The yield surfaces showed increasing chalk strength with decreasing porosity, as illustrated by increasing failure envelope size for decreasing chalk porosity.

2.2 Fracture Propagation

Injection induced fracturing due to injection of fluids into the reservoir, commonly reference tensile fractures formed due to extensional effective stresses (Fjær et al. 2008). As discussed in Section 2.1.3.4, Teufel and Rhett (1991) also found that shear fracturing was an important mechanism for permeability enhancement in depleted chalk reservoirs.

2.2.1 Hydraulic Fracturing

Hydraulic fracturing is commonly used to describe tensile fracturing, by which high wellbore injection pressures are used to induce extensive effective stresses according to the effective stress concept (Equation 2.4). Hydraulic fracturing is generally characterized by 3 different stages (Fjær et al. 2008):

- Fracture Initiation/Formation Breakdown
- Fracture Propagation
- Fracture Closure

2.2.1.1 Fracture Initiation / Formation Breakdown

The fracture initiation pressure describes the pressure required to induce an initial small fracture extending from the borehole (Detournay and Carbonell 1997). The fracture initiation pressure is a function of the far field stress state of the reservoir, the tensile strength of the formation and stress concentration around the wellbore. The near wellbore stress concentration causes fracture initiation to be a function of both minimum (σ_h) and maximum horizontal stresses (σ_H) (Fjær et al. 2008).

The upper limit for the fracture initiation pressure (p_i) is the Hubert-Willis expression, which is applicable for impermeable rocks, or wells with impermeable mud cakes (Detournay and Carbonell 1997):

$$p_i = 3\sigma_h - \sigma_H + T_0 - p_0 \tag{2.8}$$

p_0 = Far field pore fluid pressure (unaffect by the wellpressure)

The lower limit for fracture initiation pressure is given by the Haimson-Fairhurst expression, and describes permeable rocks with a permeable mud cake (Detournay and Carbonell 1997):

$$p_i = \frac{3\sigma_h - \sigma_H + T_0 - 2\eta p_0}{2(1-\eta)} \tag{2.9}$$

η = Poro-elastic constant (1/2*A_{pe}, with A_{pe} from Section 2.4.1)

p_0 = Far field pore fluid pressure (unaffect by the wellpressure)

Fjær et al. (2008) outlined that the actual fracture initiation pressure is normally between these two extremities, due to either local borehole defects or time-dependent pressure transfer between the borehole and the formation. As a general rule it may therefore be hard to use the fracture initiation pressure to quantify the stress field heterogeneity.

Formation breakdown was examined at length by Detournay and Carbonell (1997), and was shown to deviate from the fracture initiation pressure when the initial formed fracture was stable. Unstable fracture formation, as characterized by dropping well pressure (p_w) in Figure 2.9, is characteristic of formation breakdown where the growing fracture volume exceeds the injection volume. This feature can be used as a clear indication of a formed fracture (Detournay and Carbonell 1997). Initial fracture stability has been shown to be a function of pressurization rate and initial fracture length, and the results indicate that formation breakdown pressure under normal circumstances cannot be used as a reliable estimate for the fracture initiation pressure (Detournay and Carbonell 1997).

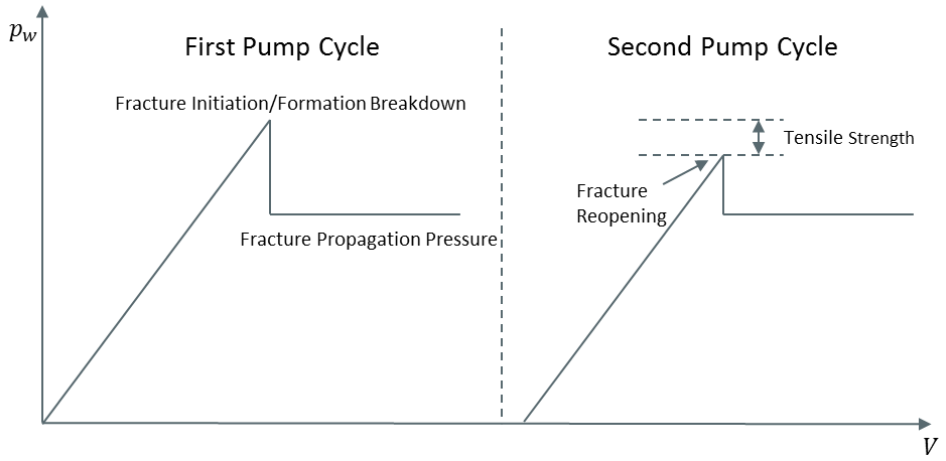

Figure 2.9: Idealized pumping cycle, wellbore pressure (p_w) plotted against pumped volume (V). The example shows fracture initiation pressure equal to the formation breakdown pressure, indicating an unstable initially formed fracture. Fracture reopening pressure is lower than the fracture initiation pressure if the formation has initial tensile strength. A difference may also be experienced if Lost Circulation Material (LCM) has been used during drilling.

2.2.1.2 Fracture Propagation

The fracture propagation pressure is the pressure required for the fracture to extend into the formation. In an ideal situation with no pressure loss in the fracture, the fracture propagation pressure will be equal to the minimum effective stress in the formation, which is the minimum horizontal stress when the vertical stress is a principal stress. Stable fracture propagation pressure is therefore indicative of the fracture propagating beyond the near field stress effect of the wellbore. However, generally flow induced pressure drop in the fracture due to fluid leakoff, along with fracture tip resistance and fracture geometry, causes the fracture propagation pressure to exceed the minimum effective stress (Fjær et al. 2008). A fracture will continue to propagate as long as the injection rate exceeds the fracture leakoff rate.

2.2.1.3 Fracture Closure Pressure

Fracture closure pressure determination will be discussed in Section 2.9. The closure pressure is the pressure required for the induced fracture to close, and is a direct measurement of the minimum effective stress in the formation (Fjær et al. 2008). Fracture closure is a gradual process as discussed by several authors (Fjær et al. 2008, ConocoPhillips and Cramer 2015, McClure et al. 2016), and may describe both mechanical and hydraulic closure (Figure 2.10). Mechanical closure describes the first contact between the two surfaces of the formed fracture, and McClure et al. (2016) argued that this is a measurement of the lowest closure stress in the contacted formation. Traditional fracture closure analysis such as that outlined by Barree et al. (2007), uses a pressure closer to hydraulic closure as a measurement of the fracture closure pressure. Studies in this thesis have shown that in softer formations, such as chalk reservoirs, the deviation between these two closure pressure measurements is small and in the region of ~100 psi (Section 3.2).

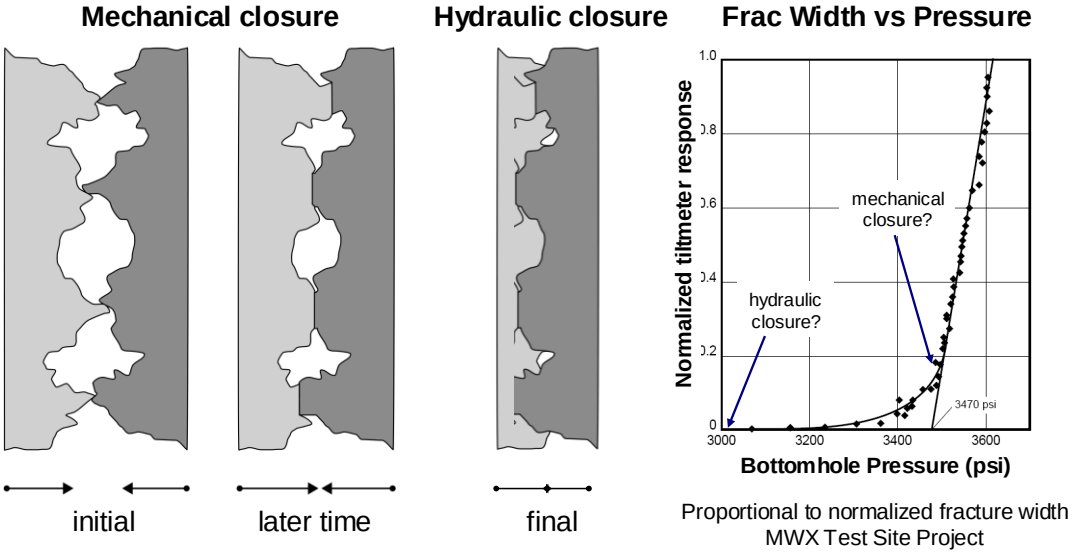

Figure 2.10: Illustration of mechanical and hydraulic closure. In harder formations the difference between the two pressures is expected to be significant. Softer formations, such as chalk reservoirs have less deviation between the two pressures (Illustration from ConocoPhillips and Cramer (2015)).

2.2.1.4 Fracture Reopening

The fracture reopening pressure is the pressure required to open a previously induced fracture (Figure 2.9). In naturally fractured reservoirs, such as North Sea chalk fields, the tensile strength of the formation will be close to 0, and tensile fracturing is believed to open existing natural fractures (Rod and Jørgensen 2005, Fjær et al. 2008). Injection wells in chalk reservoirs are traditionally subject to acid stimulation above the fracture pressure, and the fracture reopening pressure is therefore the pressure controlling injection fracture development after stimulation.

Fractured chalk reservoirs can be observed to have an initial tensile strength if the mud cake contains Lost Circulation Material (LCM), in which case the fracture initiation pressure will be higher than the fracture reopening pressure due to the bonds created by the LCM.

2.2.1.5 Wellbore Geometry

Modern field developments use horizontal wells. The wellbore geometry and borehole orientation will primarily have an impact on the fracture initiation pressure as outlined by Fjær et al. (2008). The fracture initiation pressure will then also be a function of the overburden stress (σ_v). As a general rule the fracture initiation pressure will vary as a function of wellbore orientation relative to the in-situ stress field, with the initial induced fracture growing in the direction of least resistance (Fjær et al. 2008). Wellbore effects hence govern the direction of least resistance, which may deviate from the direction of lowest in-situ stress (σ_h). However, a propagating fracture will eventually align itself with the in-situ stress field and give a correct estimate of the minimum in-situ formation stress, assuming the fracture is propagated long enough to allow for the alignment (Fjær et al. 2008).

2.2.1.6 Thermal Effects

Due to injection of cold water into hot reservoirs, the reservoir rock will be subject to cooling which will result in induced thermal stresses. Around injectors in sandstone reservoirs, cooling is known to cause the rock matrix to contract resulting in reduced effective stresses and therefore reduced fracture gradients (Fjær et al. 2008). The thermal effect is limited to the cooled zone, which under normal reservoir conditions correspond to 30%-50% of the injection flood front (Fjær et al. 2008).

Eltvik et al. (1992) showed that in low permeability chalk reservoirs, such as the Valhall, Eldfisk and Ekofisk fields, poroelastic effects dominate over thermoelastic effects. Thermoelastic stresses may therefore be neglected in chalk reservoirs when considering fracture development (Eltvik et al. 1992). Madland et al. (2002) stipulated that the impact of chemical rock-fluid interactions on chalk strength is temperature dependent, indicating that temperature may still impact the fracture development in chalk.

2.2.2 Shear Fracturing

As previously referenced, Teufel and Rhett (1991) indicated that shear failure during reservoir compaction was the primary reason for permeability maintenance during depletion of the Ekofisk Field. Shear fracturing will not create large single fractures as caused by tensile fracturing, but will create smaller fractures enhancing the natural chalk fracture network (Teufel and Rhett 1991). As a consequence, shear fracturing will primarily lead to a reservoir permeability increase. As shear failure may occur before the minimum effective stress becomes extensional, shear fracturing may occur at injection pressures below the fracture closure gradient.

2.3 Biot Stress Coefficient

The Biot stress coefficient (α) is a key parameter for understanding the impact of pore pressure on formation stresses (Equation 2.4). Omdal et al. (2009) discovered axial strains in chalk cores under hydrostatic loading with constant differential stress ($\sigma_{ext} - p_f$), which did not correspond with a Biot stress coefficient close to unity (Figure 2.11). This observation formed the basis for experiments on a total of 8 core samples. All showed Biot stress coefficients deviating from unity, with the surprising trend of lower coefficient values for higher porosities (Omdal et al. 2009).

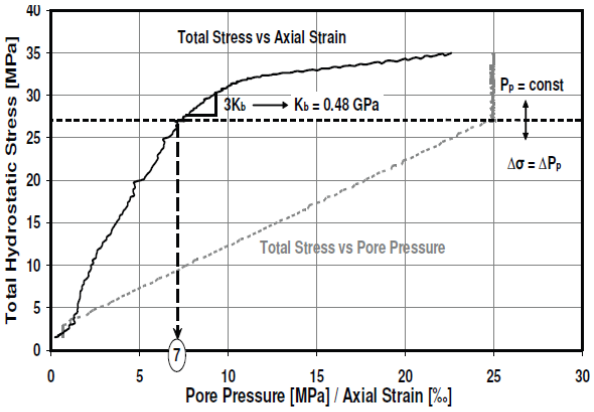

Figure 1. Simultaneous increase of total stress and pore pressure, Stevns Klint core, porosity 0.489.

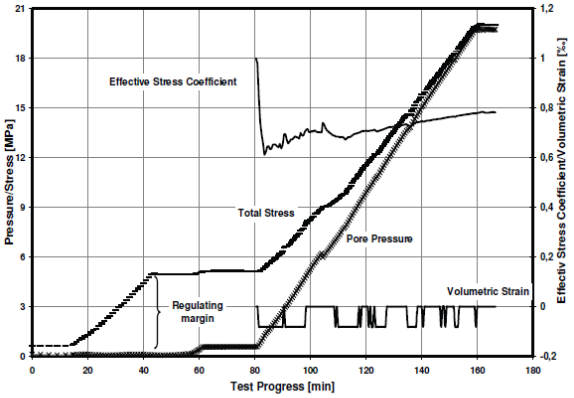

Figure 2. Constant bulk volume test for core 1, tested pre yield with distilled water as pore fluid.

Figure 2.11: Results from Omdal et al. (2009). Initial observations during hydrostatic loading in triaxial load cells showed up to 7 percentiles axial strain under constant differential stress (Figure 1). This lead to experimental investigations under constant volumetric strain, indicating chalk effective stress coefficients significantly lower than unity (0.6-0.8, Figure 2) (Illustration from Omdal et al. (2009)).

These results directly contradict the results of Teufel and Warpinski (1990), where experiments on Ekofisk chalk with porosities ranging from 15%-36%, showed α ranging from 0.72 to unity, respectively. This was explained by lower degree of consolidation in higher porosity chalks. The Biot stress coefficient can be understood as the ratio of chalk grain area exposed to pore fluid, to the total chalk grain area. As the degree of consolidation increases, less grain area is exposed to the pore fluid, and as a consequence the Biot factor decreases (Omdal 2010).

The results of Omdal et al. (2009) also showed that in the elastic stress regime the stress coefficient trend was increasing (Figure 2.11), while in the plastic stress regime the trend was decreasing. This was suggested to be an impact of particle cohesion, where an increasing trend indicated a decreasing degree of cohesion, exposing more grain surface area to the pore fluid (Omdal 2010).

Biot (1941) underlined that the effective stress relation given by Equation 2.4 is limited to elastic deformation, and as a result Omdal et al. (2009) also indicated that the experimental deviations may be due to inelastic deformation effects.

The deviation from earlier data seen in Omdal et al. (2009), led to an examination by Madland et al. (2009) of effective yield stress as a function of total yield stress. The results showed no variation in effective yield stress with total yield stress (Figure 2.12), which supported a Biot stress coefficient close to unity when considering chalk strength (Madland et al. 2009).

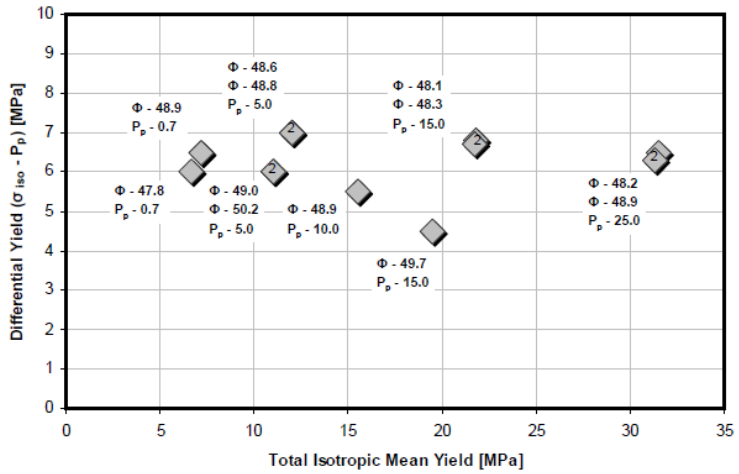

Figure 2.12: Chalk yield strength as a function of total isotropic stress vs differential stress. The differential stress is the difference between the total isotropic stress and the pore pressure (Omdal 2010). The yield strength is constant as a function of total isotropic stress, indicating a Biot stress coefficient close to unity in terms chalk yield strength (Illustration from Omdal (2010)).

In common reservoir rock mechanics theory, the ratio of modulus of the bulk and solid is used to describe α (Charlez 1991):

$$\alpha = 1 - \frac{K_b}{K_s} \tag{2.10}$$

K_b = Modulus of the bulk

K_s = Modulus of the solid

Studies conducted by Walls et al. (1998) on the Ekofisk Field, showed log derived modulus of the solid (K_s) equal to 65 GPa and modulus of the bulk (K_b) for 40 % porosity chalk equal to 4 GPa, which gives a Biot stress coefficient of 0.94 following Equation 2.10. Analysis by Risnes et al. (2005) of ≈ 40 % porosity outcrop chalk with varying water-glycol mixtures, showed chalk bulk moduli ranging from 0.35 – 1.20 GPa. These results show that chalk Biot stress coefficients evaluated with Equation 2.10 will be close to unity for high porosity chalk.

However, the results shown by several different studies (Teufel and Warpinski 1990, Madland et al. 2009, Omdal et al. 2009), indicate that the conception of a Biot stress coefficient close to unity for all reservoir chalks may be too simple. The degree of cohesion seems to play a key role, and could be impacted by reservoir rock-fluid interactions. As water is injected into the reservoir, pore pressure will

increase, which for lower porosity chalks with higher degree of consolidation may lead to an increase in the Biot stress coefficient. Precipitation and dissolution may also lead to change in the cohesion between matrix grains, resulting in a potential decrease or increase in Biot stress coefficient over time as a function of flooded pore volumes of seawater. These effects could impact the measured reservoir closure stress trend as described in Section 2.4.

2.4 Pore Pressure Impact on Horizontal Stress

Goulty (2003) outlined that changes in horizontal stresses within a reservoir may relate to changes in pore pressure by three different compaction mechanisms: poroelastic behavior, normal faulting and normal compaction. For a comprehensive overview of the different mechanisms, see Goulty (2003). Poroelastic compaction is governed by elastic chalk deformation (Section 2.1.3.1), while normal faulting compaction is controlled by shear failure (Section 2.1.3.4) and activation of faults in the reservoir (Goulty 2003). Normal compaction is primarily controlled by plastic porosity loss under increased mean effective stresses (Goulty 2003).

Goulty (2003) compared Ekofisk and Valhall stress trends to laboratory measurements of chalk properties, and showed that both Ekofisk and Valhall depletion stress trends conformed to behavior expected from normal faulting or poroelastic mechanisms. In spite of significant reservoir pore collapse evident from seabed subsidence at the Ekofisk Field (Nagel 1998, Jensen et al. 2000, Doornhof et al. 2006, Nermoen et al. 2015), the horizontal stresses did not conform to trends expected for plastic yielding (Goulty 2003). Poroelastic deformation or normal faulting were therefore the best mechanisms to describe the observed stress trends in the Ekofisk and Valhall fields (Goulty 2003), but discrimination between the two deformation mechanisms could not be made by Goulty (2003).

Since Goulty (2003) showed that Ekofisk depletion stress trends could conform to poroelastic behavior, poroelastic compaction models will be used in this thesis to discuss the observed Eldfisk depletion stress trend. The normal faulting model is highlighted as a potential alternative mechanism, but not discussed further.

2.4.1 Poroelastic Compaction

Poroelastic compaction describes reservoir compaction controlled by elastic deformation. As highlighted in Section 2.1.2, the effective stresses control rock deformation and therefore reservoir compaction. The effective stress concept outlined in Equation 2.4 (Section 2.1.2) is only valid for elastic conditions (Biot 1941), and may therefore be applied when evaluating stress changes under poroelastic conditions. Following the traditional assumption of Biot stress coefficient (α) close to unity, means that α can be assumed constant in Equation 2.4. The change in effective stress as a function of change in total stress and pore pressure can then be expressed as seen in Equation 2.11.

$$\Delta\sigma' = \Delta\sigma - \alpha \cdot \Delta p_f \tag{2.11}$$

Equation 2.11 represents the conventional difference effective stress relation outlined in the literature (Fjær et al. 2008). However, as outlined in Section 2.3, Omdal et al. (2009) conducted laboratory experiments that contradicted the general conception of unity Biot stress coefficient in high porosity chalk. If variations in Biot stress coefficient are to be considered (Section 2.3), then a new relation can be derived that accounts for the impact of changes in the Biot stress coefficient (α) during depletion (Equation 2.12).

$$\Delta\sigma' = \Delta\sigma - \overline{\alpha} \cdot \Delta p_f - \Delta\alpha \cdot \overline{p_f} \tag{2.12}$$

$\overline{\alpha}$ = Arithmetic average Biot stress coefficient over analyzed pressure interval

$\overline{p_f}$ = Arithmetic average pore pressure

The relations seen in Equation 2.11 and 2.12 assume elastic behavior, such that the changes in stresses are linear functions of the induced strain. Any linear elastic media will conform to Hooke's law of linear elasticity (Fjær et al. 2008), as shown in Equation 2.13 assuming the vertical stress direction to be a principal stress direction.

$$E\varepsilon_h = \sigma_h' - \nu(\sigma_H' + \sigma_v')$$

$$E\varepsilon_H = \sigma_H' - \nu(\sigma_h' + \sigma_v')$$

$$E\varepsilon_v = \sigma_v' - \nu(\sigma_h' + \sigma_H') \tag{2.13}$$

ε = Strain

E = Young's modulus

ν = Possion's ratio

h = Minimum horizontal stress direction

H = Maximum horizontal stress direction

v = Vertical stress direction

Reservoir compaction studies normally assume uniaxial compaction conditions (Goulty 2003, Fjær et al. 2008), where pore pressure depletion is assumed to only induce vertical strain (ε_v). This assumption may apply if the lateral dimensions of the reservoir are significantly larger than the vertical reservoir thickness (Goulty 2003). Under these assumptions, Equation 2.13 can be written on the difference form seen in Equation 2.14.

$$0 = \Delta\sigma_h' - \nu(\Delta\sigma_H' + \Delta\sigma_v')$$

$$0 = \Delta\sigma_H' - \nu(\Delta\sigma_h' + \Delta\sigma_v')$$

$$E\Delta\varepsilon_v = \Delta\sigma_v' - \nu(\Delta\sigma_h' + \Delta\sigma_H') \tag{2.14}$$

The equations for horizontal stresses then simplify to the form seen in Equation 2.15,

$$\Delta\sigma_H' = \Delta\sigma_h'$$

$$0 = \Delta\sigma_h' - \nu(\Delta\sigma_h' + \Delta\sigma_v') \tag{2.15}$$

which gives the uniaxial stress relation for the effective minimum horizontal stress (Equation 2.16).

$$\Delta\sigma_h' = \frac{\nu}{1-\nu}\Delta\sigma_v' \tag{2.16}$$

Equation 2.11 shows that under the assumption of constant Biot stress coefficient (α), both the change in effective minimum horizontal stress ($\Delta\sigma_h'$) and effective overburden stress ($\Delta\sigma_v'$) can be expressed in terms of total stress and pore pressure changes.

$$\left(\Delta\sigma_h - \alpha \cdot \Delta p_f\right) = \frac{\nu}{1-\nu}\left(\Delta\sigma_v - \alpha \cdot \Delta p_f\right) \tag{2.17}$$

Following the normal derivation of the uniaxial compaction model, the total overburden stress is assumed to only be a function of the overburden weight and therefore constant (Fjær et al. 2008).

$$\Delta\sigma_v = 0 \tag{2.18}$$

This is a common assumption for deep reservoirs such as the Eldfisk and Ekofisk fields, due to the large weight of the overburden dominating the stress regime (Fjær et al. 2008). However, the domal trap structure of both the Eldfisk and Ekofisk fields may cause stress arching over some or larger parts of the reservoir (Nagel 1998), resulting in a reduction of the total overburden stress.

The uniaxial compaction model for change in total minimum horizontal stress ($\Delta\sigma_h$, closure pressure) as a function of pore pressure, under the assumption of constant total vertical stress ($\Delta\sigma_v = 0$), is then given by Equation 2.19 (Hagoort et al. 1980).

$$\Delta\sigma_h = \frac{1-2\nu}{1-\nu}\alpha \cdot \Delta p_f$$

$$\Delta\sigma_h = A_{pe} \cdot \Delta p_f$$

$$A_{pe} = \frac{1-2\nu}{1-\nu}\alpha \tag{2.19}$$

A_{pe} = Poroelastic constant (Hagoort et al. 1980)

Equation 2.19 shows that under linear elastic assumptions with constant Biot stress coefficient and uniaxial compaction, the measured change in closure stress (pressure) is a linear function of the change in pore pressure. This poroelastic model was shown by Goulty (2003) to give a good match of compaction behavior on the Ekofisk and Valhall fields.

For varying Biot stress coefficient (α) the relation is given in Equation 2.20, under same assumptions as in Equation 2.12.

$$\Delta\sigma_h = \frac{1-2\nu}{1-\nu}\overline{\alpha} \cdot \Delta p_f + \frac{1-2\nu}{1-\nu}\overline{p_f} \cdot \Delta\alpha \tag{2.20}$$

Equation 2.20 shows that the closure stress can be a linear function of pore pressure with varying Biot stress coefficient, if the Biot stress coefficient (α) is a linear function of pore pressure (p_f).

2.4.2 Stress Arching

As mentioned in Section 2.4.1, stress arching may be a factor in reservoirs with significant pressure gradients and extensive depletion. Nagel (1998) used finite element modelling of Ekofisk subsidence to show that stress arching could be required to match the observed field subsidence. In a reservoir with significant stress arching, the overburden stress on the flanks will increase during depletion, while the overburden stress towards the crest will be partially released. Assuming linear elasticity, this will impact the minimum horizontal stress in accordance with Equation 2.21.

$$\Delta\sigma_h = \frac{\nu}{1-\nu}\Delta\sigma_v + \frac{1-2\nu}{1-\nu}\alpha \cdot \Delta p_f \tag{2.21}$$

2.4.3 Stress Path K

The stress path parameter K is often used to analyze and express stress changes during depletion and repressurization (Teufel and Rhett 1991, Fjær et al. 2008, Omdal et al. 2010). The parameter is defined as the ratio of change in horizontal effective stress to change in vertical effective stress, and is therefore under elastic uniaxial compaction conditions defined as seen in Equation 2.22:

$$K = \frac{\Delta\sigma_h'}{\Delta\sigma_v'} = \frac{\nu}{1-\nu} \tag{2.22}$$

Teufel and Rhett (1991) indicated that $K = 0.2$ was found to be the most representative stress path for Ekofisk Field fracture test.

2.5 Stress Hysteresis

Stress hysteresis considers the impact of stress history on rock failure and stress paths. Teufel and Rhett (1992) outlined the difference between depletion and repressurization behavior in Ekofisk chalk (Figure 2.13). Depletion led to pore collapse and an overall increase in the Mohr's-circle size. Due to the pore collapse, the chalk behaved as a stronger lower porosity material during repressurization than it had during the depletion phase (Teufel and Rhett 1992). In addition, the repressurization was suggested to follow a stress path K closer to unity, corresponding to isotropic conditions (Figure 2.13B). The repressurization would then lead to shear failure in significantly depleted regions of the reservoir (Teufel and Rhett 1992). This analysis indicated that a uniaxial compaction model may not be representative for reservoir repressurization.

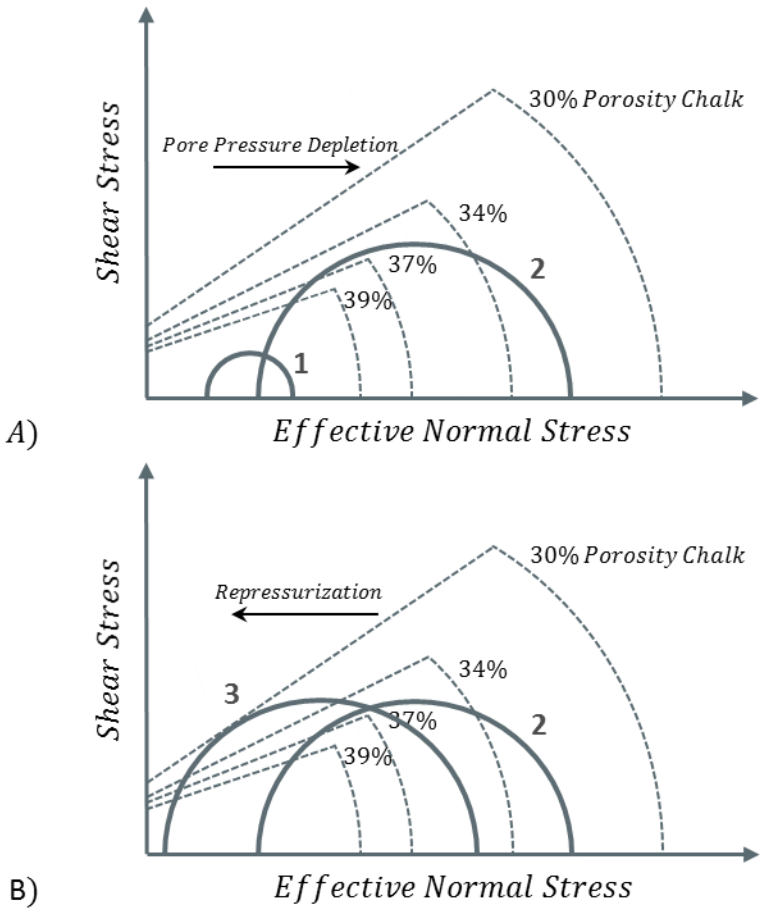

Figure 2.13: Illustration of stress hysteresis in the Ekofisk Field as outlined by Teufel and Rhett (1992). Figure A shows increase in Mohr's-circle during pore pressure depletion, with pore collapse of porosities exceeding 34 % when depleting from 7000 psia to 3500 psia (Teufel and Rhett 1992). Teufel and Rhett (1992) determined the depletion stress path K for Ekofisk to 0.2. Figure B shows repressurization following a stress path equal to unity, resulting in chalk shear failure during injection.

The stress hysteresis outlined by Teufel and Rhett (1992) describes a fracture initiation pressure hysteresis (ref. Section 2.2.1.1), where the fracture initiation pressure is decreased as the failure mode changes from tensile to shear failure. Results by Madland et al. (2002), Omdal et al. (2009) and Teufel and Warpinski (1990) indicate that there may be changes in Poisson's ratio and Biot stress coefficient during production from chalk reservoirs, which may result in changes in the closure pressure in accordance with Equation 2.20.

Experiments on Liège outcrop chalk by Madland et al. (2002), suggested a fluid dependency of chalk Poisson's ratio due to rock-fluid interactions. The experiments were conducted on several cores saturated with water and glycol (Figure 2.14). The glycol saturated chalk was proven to have yield properties comparable to oil, and could be used as an oil substitute (Madland et al. 2002). The results showed a decrease in Poisson's ratio of the chalk when glycol was replaced by water. This would indicate that as water displaces oil in the reservoir, the slope of the closure pressure trend would be increased in accordance with Equation 2.19. In accordance with Equation 2.4 and 2.22, a change in the Poisson's ratio will impact the stress path and not the stress state of the rock material.

Table 8. Elastic properties, water and glycol saturated Liège chalk.

Fluid	Water		Glycol	
T (°C)	20	130	20	130
E-mod. (GPa)	0.83 (13)	0.77 (8)	1.96 (11)	1.42 (8)
ν	0.21 (11)	0.16 (8)	0.31 (11)	0.24 (6)

Figure 2.14: Impact of rock-fluid interactions on rock properties, the number of experiments are given in parenthesis. The results show a significant reduction in Poisson's ratio at Ekofisk reservoir temperature (130 °C) for water compared to glycol. Experiments also showed that glycol behaved similarly to oil in terms of chalk strength (Table from Madland et al. (2002)).

Omdal et al. (2009) demonstrated during loading under constant differential stress, that chalk cores indicated Biot stress coefficients significantly lower than unity (Section 2.3). Water saturated Stevns Klint cores with a porosity of ~44%, showed Biot stress coefficients as low as 0.6 - 0.8. A constant differential stress regime indicates isotropic change of the total stress, and may indicate a stress path dependence of the Biot stress coefficient. Following the stress path change suggested by Teufel and Rhett (1992), this could indicate different Biot stress coefficients during repressurization compared to depletion. Omdal et al. (2009) also postulated a potential impact of inelastic deformation on the Biot stress coefficient. Combined with the quasi-elastic chalk behavior indicated by Madland et al. (2009), changes in closure stress in response to reservoir stress history appears likely.

Teufel and Warpinski (1990) showed variations in Biot stress coefficient as a function of porosity for Ekofisk cores (Section 2.3). The variation was explained by changes in degree of cohesion. In high porosity reservoir rocks which experience pore collapse during depletion, this may result in a decrease in Biot stress coefficient with decreasing reservoir pressure (Teufel and Warpinski 1990). Assuming only limited reversibility of the porosity loss during repressurization, this will lead to a permanent lowering of the Biot stress coefficient. However, the results also indicated that the changes in Biot stress coefficient will be limited (Teufel and Warpinski 1990), as porosities are unlikely to decrease below 30 - 34 % due to pore collapse (Teufel and Rhett 1992). Potential changes in Biot stress coefficient can be assumed to be gradual, as it would otherwise lead to sharp changes in rock stress state (Equation 2.4).

2.6 Water Weakening

The type of pore fluid is known to have a significant impact on chalk failure surface and rock strength (Risnes 2001, Madland et al. 2002, Risnes et al. 2003, Risnes et al. 2005, Omdal 2010). In producing reservoirs, the majority of measured closure stresses will for economic reasons be from oil filled zones. Limited measured data is therefore available from water weakened zones. Understanding water weakening mechanisms may therefore be important in order to understand stress and conductivity development around water injection wells.

As described in Section 2.5, experiments by Madland et al. (2002) showed that water saturated chalk has significantly different elastic properties compared to glycol saturated chalk. Risnes (2001) and Risnes et al. (2003) showed that water weakening leads to a significant decrease in the size of the failure surface of chalk. The result is increased pore collapse during depletion (Risnes 2001). Both mechanisms will impact the elastic properties of the chalk as well as cause inelastic deformation effects.

Multiple mechanisms have been proposed that may control the water weakening process. The mechanisms, as outlined by Gutierrez et al. (2000), can be subdivided into capillary (physical), physio-chemical and chemical. Chemical mechanisms are of particular interest for changes in chalk mechanical properties. Comprehensive studies by several authors (Heggheim et al. 2005, Korsnes et al. 2006a, Korsnes et al. 2006b, Korsnes et al. 2008, Madland et al. 2008, Zangiabadi et al. 2009, Madland et al. 2011, Megawati et al. 2011, Megawati et al. 2013, Megawati et al. 2015) have shown that chemical rock-fluid interactions can impact the mechanical properties of the rock and control the water weakening process. Madland (2005) indicated that temperature is a key controlling parameter in the degree of water weakening in chalk. Korsnes et al. (2006b) suggested that the water weakening process was controlled by substitution of calcium (Ca^{2+}) ions by magnesium (Mg^{2+}) ions from the injected seawater. Several authors (Heggheim et al. 2005, Madland et al. 2008, Hiorth et al. 2011, Madland et al. 2011, Megawati et al. 2011, Megawati et al. 2015) have also indicated that precipitation and dissolution are key chemical processes controlling water weakening. Core floods conducted by Madland et al. (2011), Megawati et al. (2015) and Madland et al. (2015) all showed precipitation of minerals which could not be explained by substitution alone.

Hiorth et al. (2011) presented a method for upscaling of chemical alterations from core flood experiments to field level. The study looked at core flood results by Madland et al. (2011), which showed reduction in Mg^{2+} and SO_4^{2-} concentrations and increase in Ca^{2+} concentration in the effluent when flooding chalk cores with Synthetic SeaWater (SSW). The core flood experiments were compared with produced water samples from a flooding pattern in the Ekofisk Field. The produced water samples showed a similar retention of Mg^{2+} and SO_4^{2-}, and an increase in Ca^{2+} in the produced water compared to the injected water (Hiorth et al. 2011). Madland et al. (2011) used scanning electron microscopy with X-ray microanalysis (SEM-EDS) on some of the flooded cores, which indicated precipitation of magnesium-bearing minerals and anhydrite ($CaSO_4$) when flooding with Synthetic SeaWater. Flooding with $MgCl_2$ solution suggested that the magnesium-bearing minerals were combinations of both silicates and carbonates, indicating a dependency on the silica content of the chalk (Madland et al. 2011). Dissolution of calcite and precipitation of magnesium-bearing minerals were also shown by Megawati et al. (2011) and Megawati et al. (2015). A precipitation and dissolution model was therefore

used by Hiorth et al. (2011) to predict the produced water composition in the analyzed Ekofisk flooding pattern. The model observations fit the trends seen from the field experience, suggesting that mineralogical alterations are occurring in the reservoir as a result of dissolution and precipitation (Hiorth et al. 2011). Hiorth et al. (2011) suggested that a region around the injection well would see an increase in dolomite concentration and a decrease in calcium concentration. The altered zone ranged from 40 – 300 m (130 – 1000 ft) from the wellbore, depending on the activation energy.

As the primary conduits of flow in the reservoir are the fractures, the majority of the chemical alterations are therefore expected to take place along fractures (Hiorth et al. 2011) and extend from the fracture face (Madland et al. 2015). This was also indicated by Feazel (2007) in SEM-analysis of cores taken from the K-09 A replacement injector on Ekofisk. K-09 A was drilled within 50 m (165 ft) of K-09 T3, which injected ~200 million barrels of seawater from 1988 to 2007. Despite the large volumes of injected seawater in the K-09 A area, the cores revealed only limited amounts of dolomite in the chalk matrix, suggesting only small amounts of precipitated magnesium-bearing minerals (Feazel 2007). Feazel (2007) primarily studied the chalk matrix, and Hiorth et al. (2011) clearly showed alterations in produced water composition on Ekofisk, suggesting that chemical alterations are primarily taking place in and around the fractures. Teufel et al. (1993) showed that the composition of the natural fracture networks on Ekofisk controlled the stress dependency of the fracture conductivity. Tectonic natural fracture networks have geometries which suggest shear failure of the chalk, and have highly stress dependent permeability (Teufel et al. 1993). Stylolite associated extension fractures show partial filling and as a result very limited stress dependent permeability (Teufel et al. 1993). Chemical alterations such as those described by Madland et al. (2011), may therefore change fracture surface geometry and composition, altering the stress dependency of the reservoir conductivity.

Madland et al. (2015) conducted experiments on cores with dual porosity/permeability aimed at mimicking the difference between natural and artificially induced fractures in chalk. An “artificial” transverse fracture was generated with a saw, while a “natural” longitudinal tensile fracture was generated with a Brazilian cell. After flooding with Synthetic SeaWater (SSW), SEM analysis revealed that both the “natural” and the “artificial” fracture were closed by precipitated minerals (Madland et al. 2015). The “natural” fracture had sealed so completely that it could not be identified. The precipitated minerals concentrated in the visible transverse fracture were both phyllosilicates and magnesium-bearing minerals. The precipitated minerals reduced the fracture conductivity (Madland et al. 2015), and indicated that the majority of the chemical alterations were seen in the fractures. This conclusion was further supported by analysis by Madland et al. (2015) on cores with a longitudinal hole (2 mm in diameter) meant to mimic a fracture. The core was flooded with SSW for two months at 1 pore volume/day and analyzed with SEM. After the flooding, chemical alterations could be seen in a

local zone extending a few millimeters from the hole (Madland et al. 2015). Beyond the altered zone the chalk was unaffected by the flooding, and in the altered zone the grain surfaces were stripped of clay minerals compared to the unaltered zone. In-situ clay minerals had formed and coated the hole wall, and aggregates of precipitated minerals were found to partly plug the previously clean hole (Madland et al. 2015). The results clearly showed that the primary zone of chemical alteration was in the fracture and in the area around the fracture. Clay minerals appeared to be mobilized and moved from the matrix into the fracture (Madland et al. 2015). In the reservoir, a change in fracture composition may lead to a change in fracture conductivity, but could also influence the stress dependency of the reservoir conductivity. As previously referenced, Teufel et al. (1993) showed that partially filled fractures showed a less stress dependent permeability, suggesting that seawater induced chemical alterations in fractures may reduce the stress dependency of the reservoir conductivity. The results also showed that the clay content of the reservoir matrix could influence the chemical composition of the fractures, potentially impacting the reservoir conductivity.

In addition, as the solubility of calcite ($CaCO_3$) and anhydrite ($CaSO_4$) decreases with increasing temperature, the chemical composition of the minerals making up the fracture network will also be dependent on the position of the thermal front (Hiorth et al. 2011). The fracture networks ahead of the thermal front will contain more anhydrite than the cooled fracture networks behind the thermal front (Hiorth et al. 2011). How this change may impact the conductivity of the fracture networks, is as of yet unknown.

2.7 Inelasticity

Inelasticity has been discussed in previous sections (2.1.3.1, 2.4.1, 2.5 & 2.6) as a potential factor causing deviation from linear elastic stress behavior as outlined in Equation 2.19 (Section 2.4.1). Inelastic effects will be of primary importance in high porosity chalk where depletion may lead to rock failure (Teufel and Rhett 1991).

2.7.1 Creep

Creep describes deformation under constant stress, and is a result of inelastic time dependent strain (Omdal 2010). Figure 2.15 shows the three common stages of creep. The transient (primary) creep stage shows decreasing creep rate, and may be associated with spreading of stable microfractures (Fjær et al. 2008). Fjær et al. (2008) pointed out that transient creep is reversible and therefore associated with elastic deformation. Steady state (secondary) creep shows stable creep rate with inelastic deformation. Teufel and Rhett (1991) showed that chalk compaction and creep results in pore collapse, leading to an overall increase in rock strength. The increase in strength makes accelerating creep (tertiary) unlikely in chalk (Omdal 2010).

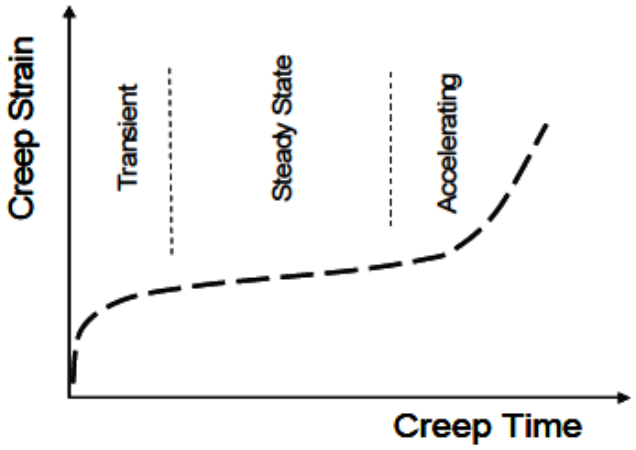

Figure 2.15: Typical creep vs time curve with the three stages of creep (Illustration from Omdal (2010)).

Omdal et al. (2010) studied the load rate dependency of creep in chalk core experiments. Core SKS 20 in Figure 2.16 was loaded at a lower rate than cores SKS 11, SKS 13 and SKS 17. The reduced loading rate led to a significant reduction in the transient creep strain, while all cores showed similar steady state creep rates (Omdal et al. 2010). This indicated a load rate dependency for the transient creep stage in chalk core experiments. Due to time constraints, laboratory experiments will tend to use higher loading rates than those observed in producing hydrocarbon reservoirs. The results by Omdal et al. (2010) therefore suggest that producing chalk reservoirs primarily see steady state plastic creep effects, without significant transient or accelerating creep. In reservoirs, chalk deformation may therefore not conform to traditional viscoelastic creep behavior (Fjær et al. 2008), but rather more viscoplastic behavior (Omdal 2016b) dominated by permanent deformation under constant stress. The reduced transient creep could also suggest that stable microfracture growth (Fjær et al. 2008) may not be a dominating deformation process in chalk reservoirs.

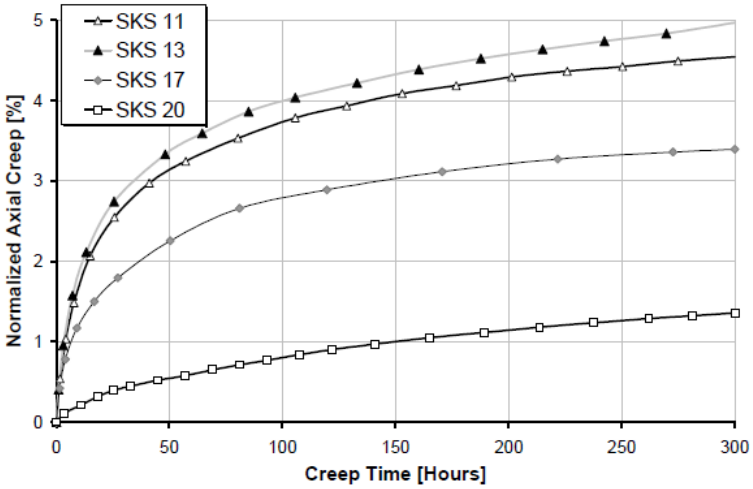

Figure 2.16: Normalized axial creep as a function of creep time for 300 hours determined by Omdal et al. (2010). Core SKS 20 was loaded at a much lower loading rate than SKS 11, SKS 13 and SKS 17. The reduced loading rate leads to a reduction in the transient creep stage, but the slope of the steady state creep is similar. In the low loading rates seen in producing hydrocarbon reservoirs this would indicate that all chalk creep may be steady state plastic deformation. (Illustration from Omdal (2010))

Viscoplastic creep deformation of chalk conforms well to the observations by Risnes (2001), who suggested that chalk failure was due to local frictional sliding at grain contacts, or shear failure between grains. This deformation will be permanent and irreversible. In terms of chalk mechanical properties, creep indicates a time dependency of chalk porosity and thus a time dependency of chalk elastic properties. The permanent nature of the deformation, suggests that the elastic properties are not likely to change significantly during repressurization (Teufel and Rhett 1992).

2.8 Acid Stimulation

Acid stimulation uses injection of hydrochloric acid to improve near wellbore properties. Acid can either be applied as a matrix treatment or as acid fracturing. Injection pressure is the primary difference between the stimulation techniques, where acid fracturing injects fluids above the fracture gradient of the formation. Acid fracturing is the primary stimulation method applied in the Ekofisk and Eldfisk fields (Snow and Brownlee 1989, Omdal et al. 2008).

The objective of acid fracturing is to generate fractures in the formation which are kept open by the uneven geometry of the acid etched fracture surfaces. Omdal et al. (2008) showed through acid injection in chalk cores, that stimulation geometry was highly dependent on chalk properties. In low porosity chalk, acid would tend to generate single narrower wormholes and not etch the entire hydraulic fracture, while higher porosity chalks showed even etching of fractures and wormholes extending from the fracture (Omdal et al. 2008). When injecting in acid fractured stimulated wells, higher porosity zones are therefore likely to be more effectively stimulated. As more fissures and fractures are contacted by the stimulation acid, a propagating injection fracture is likely to have more complex geometry in higher porosity chalk.

Economides and Nolte (2000) indicated that due to high reaction rates, hydrochloric acid (HCl) used in chalk stimulation will tend to etch preferred pathways following local high permeability streaks. HCl stimulation is therefore not expected to enter the chalk matrix, preventing acidizing at grain contacts, which could influence particle cohesion and impact the Biot stress coefficient (Section 2.3).

2.9 Determining Fracture Closure Pressure

2.9.1 SQRT(t) Falloff Analysis

The fracture closure pressure may be determined by interpretation of post-fracture falloff tests. As outlined by McClure et al. (2016) and Barree et al. (2007) the closure pressure is primarily determined from plots of p_w vs $\sqrt{t}$ and p_w vs G-time (Section 2.9.2). For 1D fracture leakoff at constant differential pressure, the leakoff rate will be proportional to the inverse of the square root of time (Howard and Fast 1957, McClure et al. 2016). Coupled with constant fracture system compliance (average fracture width/p_w), this gives a wellbore pressure decay proportional with the square root of time (Nolte and

Smith 1981, McClure et al. 2016). This results in the wellbore pressure plotting linearly vs $\sqrt{t}$ during closure (Barree et al. 2007).

Barree et al. (2007) showed that the correct interpretation of fracture closure pressure from a square root of time plot, is the inflection point of the pressure curve. This is illustrated in Figure 2.17, where the highlighted (black between dots) part of the pressure curve is shown to be linear during fracture closure, and correct closure is estimated at the inflection point (Barree et al. 2007). Barree et al. (2007) also showed that fracture closure determined based on square root of time plots alone, will give incorrect closure estimates. The square root of time technique must therefore be combined with the G-function technique (Section 2.9.2), with the correct closure pressure satisfying both techniques (Barree et al. 2007).

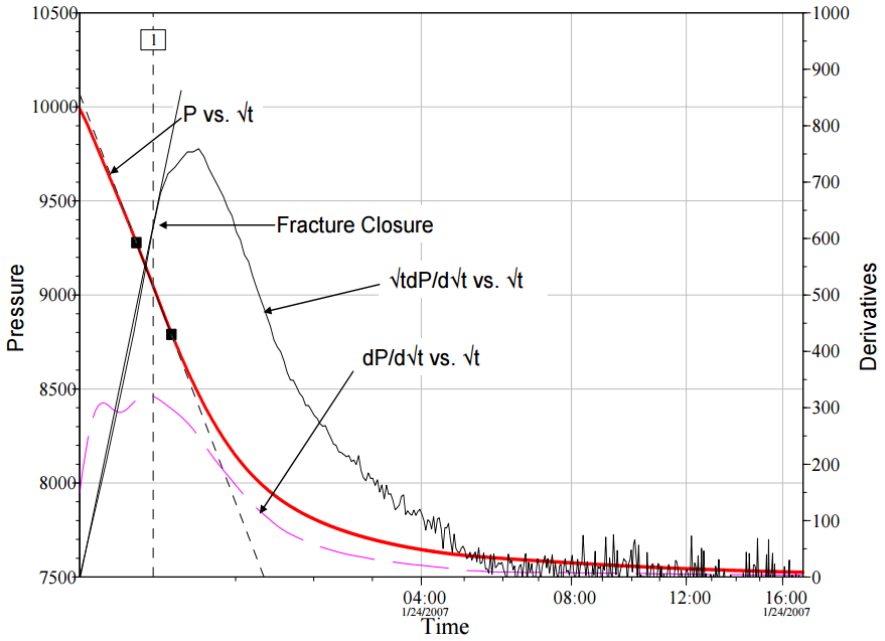

Figure 2.17: Fracture closure pressure estimated from plot of of p_w vs $\sqrt{t}$. The highlighted (black between dots) line shows the linear pressure trend seen during fracture closure. The correct closure estimate is seen to be the inflection point of the curve (Illustration from Barree et al. (2007)).

2.9.2 G-function Falloff Analysis

G-function analysis of small scale injection fractures is used to determine fracture closure pressure (Barree et al. 2007). The G-function is a time scale normalization technique, where the elapsed time is normalized to the duration of the fracture extension period (t_p). Dimensionless pumping time used in the G-function analysis is defined as (Barree et al. 2007):

$$\Delta t_D = \frac{(t - t_p)}{t_p} \tag{2.23}$$

t = Elapsed time since start of fracture propagation

t_p = Elapsed time from start of fracture propagation to shut-in

Δt_D = Normalized time

G-function analysis in low permeability formations assume high fluid efficiency, such that the fracture area is a linear function of time after shut-in of injection (Fekete 2014). More complex versions of G-function analysis exist, that account for non-linear variation of fracture surface area (Barree et al. 2007).

The intermediate function defined in G-function analysis accounts for the fracture leakoff assumption. For the low leakoff (low permeability) assumption used in this thesis, the intermediate function takes the form shown in Equation 2.24 (Barree et al. 2007).

$$g(\Delta t_D) = \frac{4}{3}\left[(1+\Delta t_D)^{1.5} - {\Delta t_D}^{1.5}\right] \qquad \text{(low leakoff)} \qquad (2.24)$$

$g(\Delta t_D)$ = Intermediate function – function of normalized time

The G-function used in fracture closure analysis is then defined by Equation 2.25 (Barree et al. 2007):

$$G(\Delta t_D) = \frac{4}{\pi}[g(\Delta t_D) - g_0] \qquad (2.25)$$

g_0 = Value of intermediate function for $t = t_p$

Barree and Mukherjee (1996) used fracture simulation analysis to show how the semi-log G-function derivative of well falloff pressures (Gdp/dG), can be used to determine fracture closure pressure. The analysis showed that for normal leakoff with no pressure dependency and constant fracture geometry, the semi-log G-function derivative would follow a linear trend from the origin as long as the fracture remained open (Figure 2.18). From this analysis it could then be shown that a deviation of the semi-log derivative from the linear trend indicates fracture closure (Barree and Mukherjee 1996). As illustrated in Figure 2.18, fracture closure may only occur once the fluid pressure in the fracture equals the fracture closure pressure. Figure 2.19 illustrates a practical example applying G-function semi-log derivative analysis to determine fracture closure pressure (Barree et al. 2007).

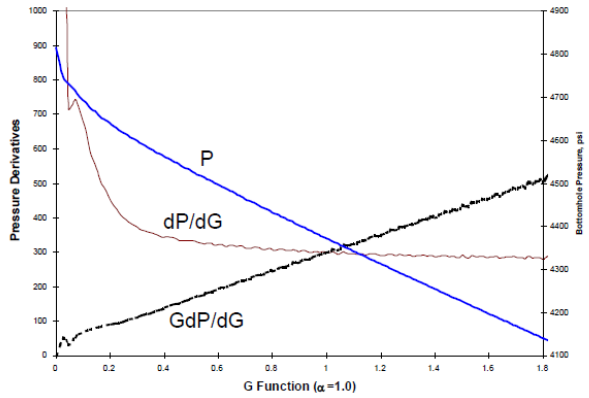

Figure 3: G-function analysis for Case 2 - normal leakoff with no pressure dependence.

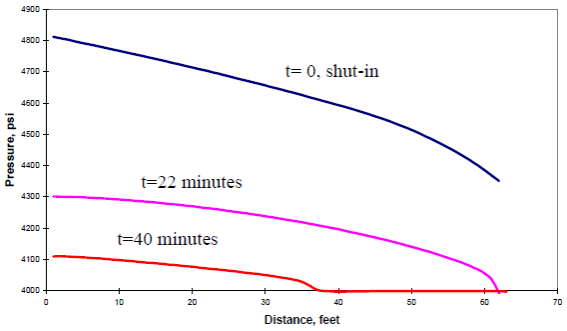

Figure 4: Pressure distribution with fracture length during closure for Case 2.

Figure 2.18: Illustration of behavior of G-function semi-log derivative (Gdp/dG) for normal leakoff behavior. The analysis shows that the semi-log derivative will follow a linear trend as long as the fracture remains open. Fracture closure pressure is 4000 psia in the example from Barree and Mukherjee (1996). (Illustration from Barree and Mukherjee (1996)).

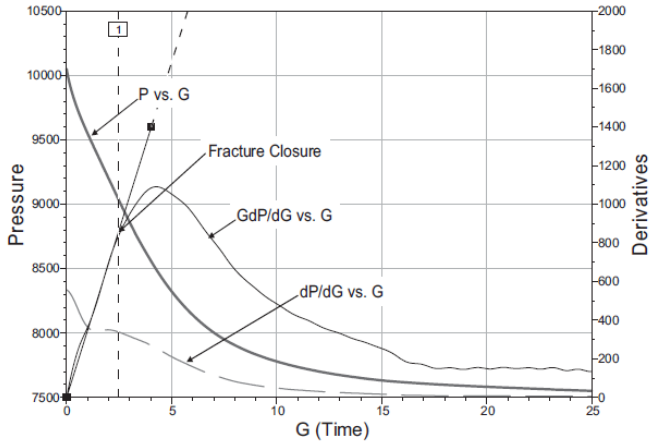

Figure 2.19: Example illustrating deviation of semi-log derivative (Gdp/dG) used to determine fracture closure pressure (Illustration from Barree et al. (2007)).

2.9.3 McClure Closure Analysis Method

An alternative closure analysis method to the G-function analysis from Section 2.9.2 has recently been developed by McClure et al. (2016) (ConocoPhillips and Cramer 2015, McClure et al. 2016), and is hereafter referenced as the "McClure method". The method used the same G-function as referenced in Section 2.9.2, but argues that closure is not indicated by a deviation from a linear semi-log derivative trend (blue arrow, Figure 2.20). Instead closure is indicated by an increase in semi-log derivative trend (orange arrow, Figure 2.20), and therefore the start of the semi-log linear trend. The method is developed and tested for low permeability (shale) minifrac analysis, and argues that the increase in semi-log derivative is the first indication of mechanical closure between the two surfaces of the fracture (Figure 2.10 (Section 2.2.1.3) and Figure 2.20). McClure et al. (2016) also indicated that in intermediate permeability formations, such as chalk, fracture closure can be identified by Gdp/dG deflecting downwards (but still increasing) due to the reduced leakoff rate of the fracture. These

observations indicate that the method outlined by Barree et al. (2007) is applicable in chalk fracture closure analysis (Section 2.9.2). The McClure method cannot be applied if only the linear part of the semi-log derivative is visible, as the point of derivative increase will be unknown.

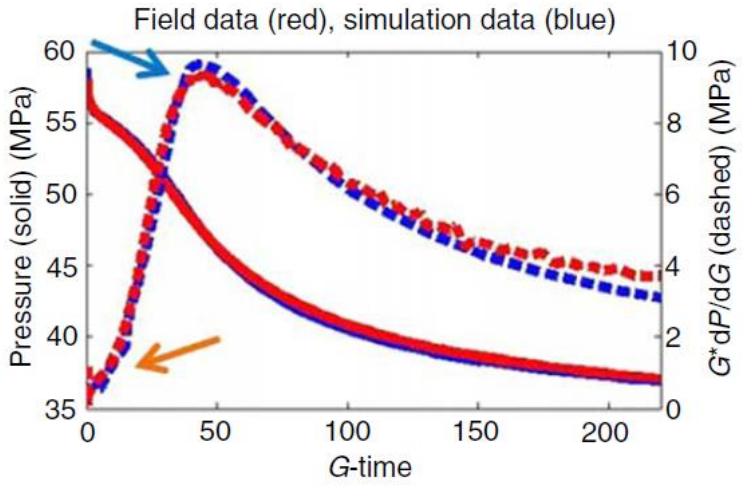

Figure 2.20: Illustration of closure estimate difference using the method developed by Mark McClure et al. (2016) (orange) compared to the traditional method outlined by the G-function analysis (blue) (ConocoPhillips and Cramer 2015, McClure et al. 2016) (Illustration from ConocoPhillips and Cramer (2015)).

2.10 Determining Fracture Initiation Pressure

2.10.1 P-Q Analysis

The fracture initiation pressure describes the pressure required to open (initiate) an injection fracture (Section 2.2.1.1). Under normal injection operations the fracture initiation pressure represents the upper bound for injection pressure, as higher injection pressures may lead to uncontrolled fracture propagation (Singh et al. 1987). The fracture initiation pressure is also referenced as Formation Parting Pressure (FPP) in other literature.

Fracture initiation pressure is traditionally determined through analysis of Step Rate Tests (SRT) (Figure 2.21). Injection rates are increased in steps from a stable reference rate, with ideal test design allowing for equal rate step length. If each rate step allows for steady-state flow conditions, where the flowing well pressure (p_w) is constant as a function of time ($dp_w/dt = 0$), then the well pressure and injection rate (q) will follow Equation 2.26 (Singh et al. 1987).

$$p_w = p_e - \left[141.2\frac{B\mu}{kh}\left(\ln\left(\frac{r_e}{r_w}\right) + S\right)\right]q \tag{2.26}$$

$r_{e,w}$ = Radius to constant pressure boundary / wellbore radius

p_e = Far-field reservoir pressure (constant pressure at $r = r_e$ from the wellbore)

B = Formation volume factor

μ = Viscosity of injected fluid

kh = Permeability thickness of formation

S = Wellbore skin (wellbore damage/enhancement)

Under steady-state conditions p_e and r_e are constant, such that there will be a linear relationship between wellbore pressure at the end of each step (p_w) and injection rate (q). A deviation from the initial linear P-Q trend signifies a change in well flow conditions, and is used as a measurement of the fracture initiation pressure/Formation Parting Pressure (FPP) (Figure 2.21) (Singh et al. 1987).

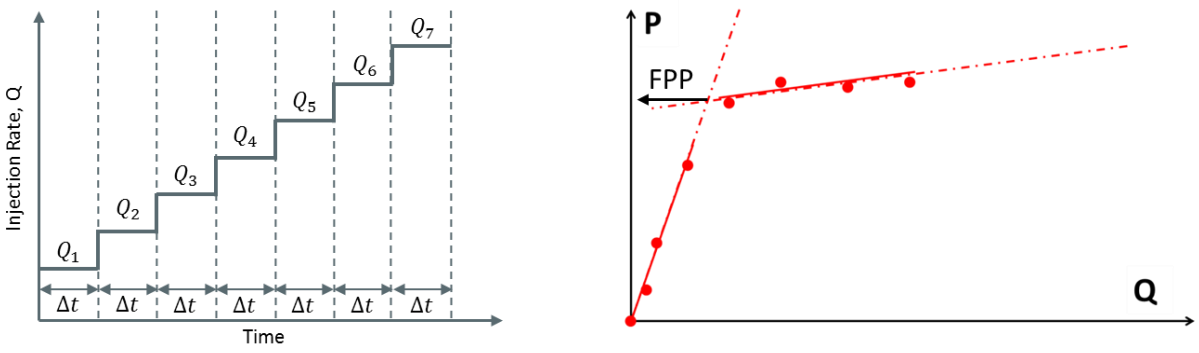

Figure 2.21: Illustration of Step-Rate Test procedure to determine fracture initiation pressure/Formation Parting Pressure (FPP). The illustration shows FPP as the point on the pressure versus rate plot where two linear trends intersect. The wellbore pressure is taken at the end of each rate step (Illustration from ConocoPhillips (2013)).

Under normal Step Rate Test conditions, as those analyzed in this thesis, the injection rate steps will represent transient flow conditions under which the well pressures will not have stabilized (Singh et al. 1987). Aronofsky and Jenkins (1954) showed that even under transient flow conditions, well pressure (p_w) and injection rate (q) will follow Equation 2.26 with r_e replaced by the effective drainage radius, r_d. For Step Rate Tests with comparable step length (Δt) the well pressure (p_w) will then still be a linear function of injection rate (q), as variations in $\ln(r_d/r_e)$ will be negligible (Singh et al. 1987).

3 Method

3.1 Eldfisk Minimum Effective Stress

Fracture closure pressure is a direct measurement of the minimum principal stress in the formation (σ_{min}). In most deep reservoirs such as the Eldfisk and Ekofisk fields the minimum stress in the formation is the minimum horizontal stress ($\sigma_{h,min}$), as the overburden stress is the largest principal stress. SPE 17854 outlines the in-situ stress state of the Ekofisk Field, as seen in Table 3.1 (Jonhson et al. 1989), which shows that the overburden stress is the largest principal stress. Due to similar overburden characteristics of the Eldfisk and Ekofisk fields, it can therefore be assumed that the fracture closure pressure is a direct measurement the minimum horizontal stress ($\sigma_{h,min}$).

Table 3.1: In-situ formation pressure and stress conditions in the Ekofisk Field as outlined in SPE17854. The Eldfisk and Ekofisk fields are situated at the same depth and have similar overburden characteristics, the in-situ overburden stress should therefore be comparable.

EKOFISK INITIAL FORMATION PRESSURE AND STRESS CONDITIONS (SPE 17854)				
Reference Depth	9500	ft-TVDSS		
Overburden	9000	psi	0.947	psi/ft
Formation Pressure	7000	psi	0.737	psi/ft
Minimum Horizontal Stress	8000	psi	0.842	psi/ft

3.2 Traditional Minifrac Analysis

The fracture closure pressure is determined by analyzing miniature fracture (minifrac) test pressure trends. A minifrac describes a small fracture generated to test formation properties (Figure 3.1). The technique is similar to an Extented Leak Off Test (XLOT), and determines fracture initiation pressure from the initial Step Rate Test (SRT), and fracture closure pressure from the following falloff (Figure 3.2). Minifrac analysis may also be applied in low permeability formations to determine reservoir permeability (Guk et al. 2014).

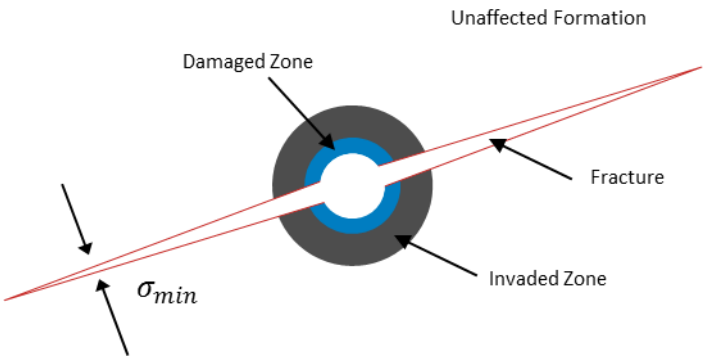

Figure 3.1: Illustration of a minifrac. The small fracture propagates through the near wellbore damaged zone and measures the true in-situ stress conditions.

A theoretical minifrac injection test cycle is illustrated in Figure 3.2. The test starts with a Step Rate Test consisting of fixed length periods of constant injection rate increased at increments from 0. The step length is constant for the reasons discussed in Section 2.10.1. The wellbore pressure increases from a stable pressure representative of the reservoir pressure, to a peak pressure indicating fracture initiation/formation breakdown (Section 2.2.1.1). After the desired max rate is obtained, the injection rate is held constant to propagate the formed tensile fracture. The wellbore pressure will drop from the formation breakdown pressure due to unstable fracture growth, and then increase slowly due to increased fracture leakoff and near wellbore pressure increase. After the extended max rate period the well is shut-in resulting in a pressure falloff test. The pressure will show an initial linear pressure decline due to stop of flow and therefore loss of wellbore friction. The end of the linear pressure decline gives a measurement of the fracture Instantaneous Shut-in Pressure (ISIP), where the difference between the last flowing pressure before shut-in and the fracture ISIP is a direct measurement of the flowing friction below the gauge. The pressure falloff after the fracture ISIP can be analyzed to determine the fracture closure pressure.

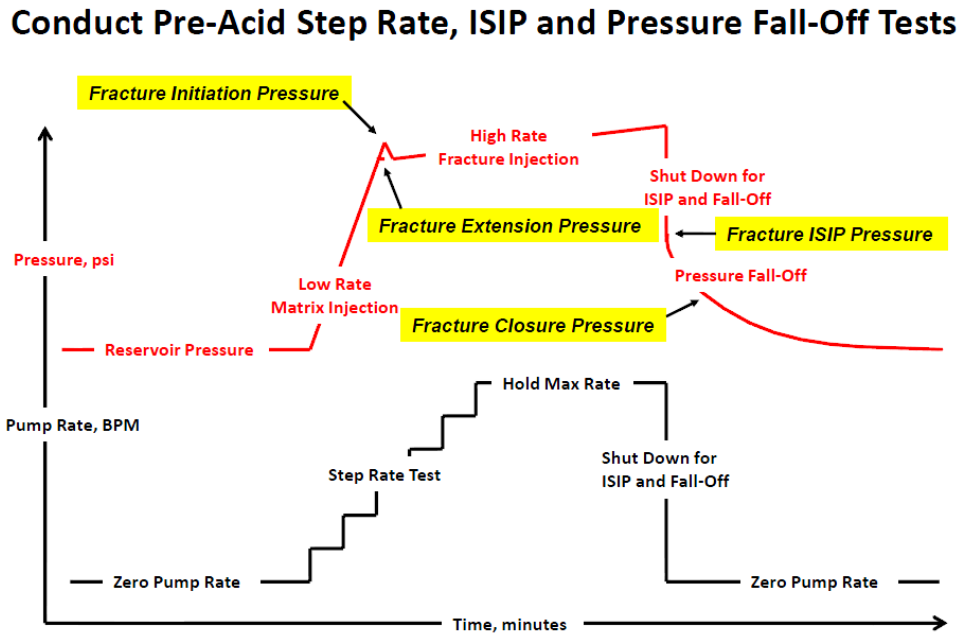

Figure 3.2: Illustration of ideal minifrac test with location of fracture initiation and fracture closure on the pressure profile. The initial Step Rate Test can be analyzed to determine fracture initiation pressure, while the pressure falloff test can be used to determine the fracture closure pressure. The fracture Instantaneous Shut-In Pressure (ISIP) is a direct measurement the wellbore friction below the gauge at the maximum injection rate. (Illustration from ConocoPhillips (2013)).

In this thesis, pre-acid stimulation and post-acid stimulation minifrac tests on the Eldfisk Field are analyzed to determine fracture closure pressure and fracture initiation pressure. A dataset with good data is shown in Figure 3.3. The datasets generally consist of 3 periods of interest for the analysis (Figure 3.3):

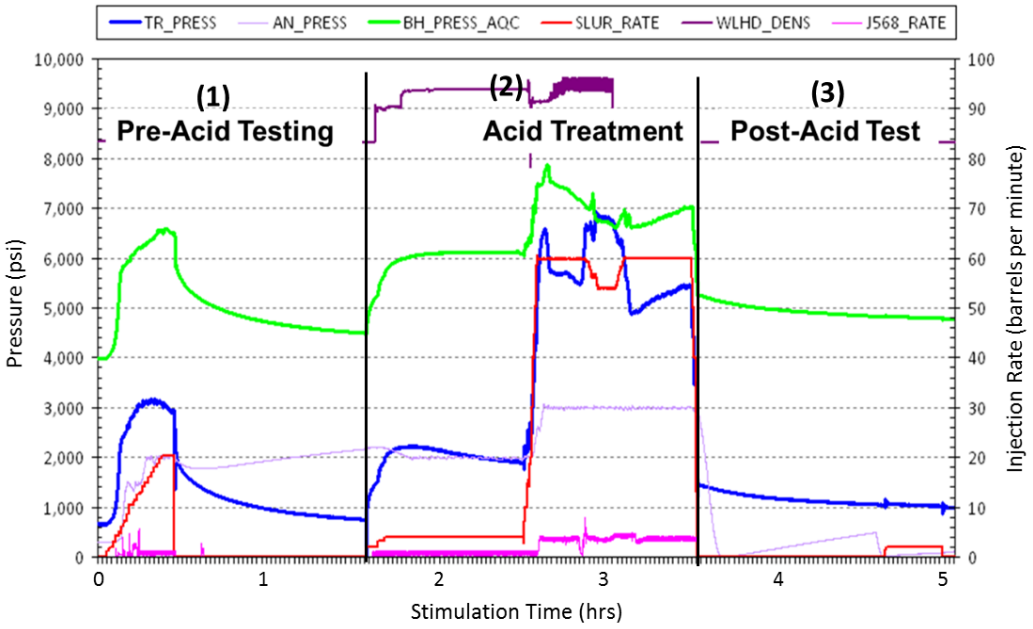

Figure 3.3: Example of a good acid stimulation dataset for closure analysis. Injection rates are shown in red and Bottom Hole Pressures (BHP) in green. The dataset shows the pre-acid and post-acid tests, which can be used to analyze property changes as a result of acid stimulation (Illustration from ConocoPhillips (2013)).

1) The pre-acid Step Rate test can be used to determine fracture initiation pressure following the method described in Section 2.10.1. A pressure vs rate (P-Q) plot is generated by plotting the average injection rate in each step against the last pressure in each step (Figure 3.4). The intersect between the two straight line trends in Figure 3.4 indicates a change in flow characteristics as a result of fracture intiation (Pong et al. 1992) (Section 2.10.1). The slopes of the straight line trends are an indication of injectivity, and as a fracture is formed the injectivity is improved due to the larger well leakoff area provided by the fracture. The linear slope is therefore reduced once a fracture is formed, as seen in Figure 3.4, and the intersect between the two linear slopes is a measurement of the injection pressure required to initate a fracture.

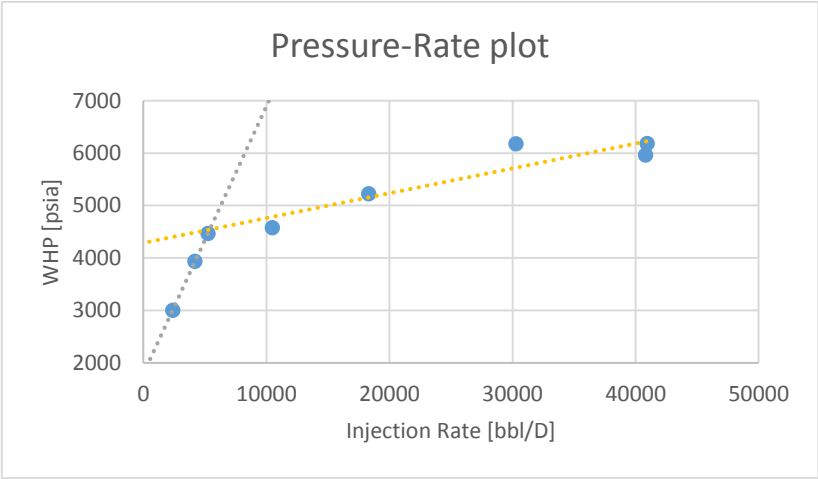

Figure 3.4: An ideal pressure vs rate (P-Q) plot. The intersect between the two straight line trends gives the fracture initiation pressure. Illustration from data analyzed as part of this thesis.

2) The pre-acid falloff test (Figure 3.2 and Figure 3.3) is used to determine the fracture closure pressure in accordance with the G-function method described by Barree et al. (2007), and square root of time method outlined in Section 2.9. The fracture closure pressure is determined as the G-function derivative deviation from linear and the closest inflection point of the square root of time pressure function (Figure 3.5). The McClure method as outlined in Section 2.9.3, is not applied due to a relatively small difference (100 psi in Figure 3.5), relatively high conductivity of the formation, and inapplicability of the method with early closure and water hammer disturbed data (Section 4.1.6.2).

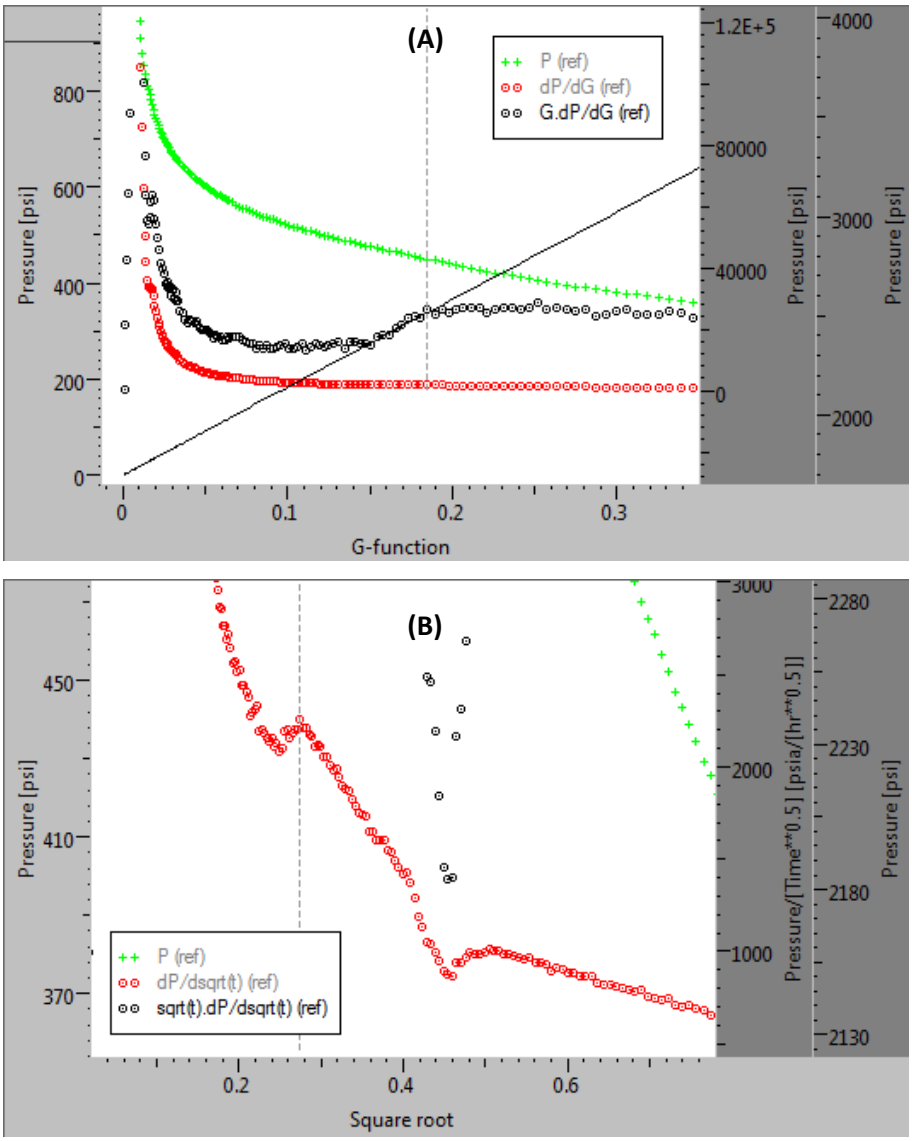

Figure 3.5: Illustration of G-function (A) and square root of time (B) technique applied to a dataset in this thesis for estimation of fracture closure pressure (Section 2.9). Fracture closure is determined at the end of the linear semi-log derivative in the G-function plot, and the inflection point in the square root of time plot. As seen in A and B, both picks match to give one unique closure pressure. Illustration generated with Saphir well test analysis software, Kappa Engineering © 2016.

3) The post-acid falloff test (Figure 3.2 and Figure 3.3) can similarly to the pre-acid falloff test be used to determine the fracture closure pressure.

3.3 Pressure Transient Analysis

Pressure Transient Analysis (PTA) describes the analysis of pressure changes over time (Schlumberger 2016). The analysis of pressure transients can be used to give information on reservoir and wellbore characteristics. In this thesis Pressure Transient Analysis of falloff and injection cycles is used to evaluate changes in reservoir conductivity and fracture development around injection wells over time. The Pressure Transient Analysis follows the approach outlined by Shchipanov et al. (2014) as part of the COREC-projects, with some modifications.

The analysis uses the Saphir well test analysis software (Kappa Engineering © 2016) to determine reservoir parameters from key flow regimes identified from semi-log derivatives. The analyzed wells are horizontal injectors and are therefore characterized by the flow regimes illustrated in Figure 3.6:

1) **Early Radial Flow**: Flow is a function of effective horizontal well length, vertical and horizontal permeability.
2) **Linear Flow**: Flow is a function of effective horizontal well length and horizontal permeability.
3) **Late Radial Flow**: Flow is a function of horizontal permeability and reservoir thickness.

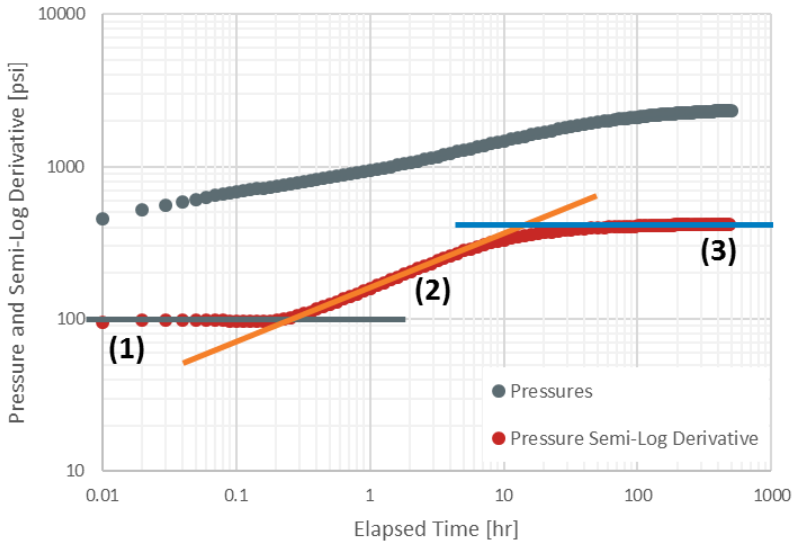

Figure 3.6: Illustration of horizontal well flow regimes. Reservoir and well characteristics can be uniquely defined if all flow regimes can be correctly identified. The flow regimes are identified from the semi-log derivative, as 1) early radial flow, 2) linear flow and 3) late radial flow. (Illustration generated with Saphir well test analysis software, Kappa Engineering © 2016).

If all flow regimes can be identified in the dataset, then the reservoir parameters can be uniquely defined. However, the falloff and continuous flow periods are normally not of the duration required to identify the late radial flow regime, and there may also be producer interference preventing late radial flow. The analysis is therefore conducted with the assumptions outlined in Table 3.2, in order to allow for consistent interpretation and evaluation of results. The assumptions may be limiting, and the analysis will therefore primarily identify changes in key parameters.

Table 3.2: Table outlining the assumptions in the conducted time-lapse Pressure Transient Analysis (PTA). The assumptions allow for consistent interpretation of the available dataset.

Assumption	Explanation
Constant effective wellbore length	The effective wellbore length is assumed equal to the perforated reservoir section. The assumption is verified with Injection Logging Tools (ILT) and 4D seismic.
$k_v/k_h = 1$	Simplifying assumption, as early radial flow can only be identified in a limited number of datasets. The determined permeability is therefore best used to indicate changes.
Constant no. of fractures	The no. of fractures is assumed established by the stimulation. Any fracture change is due to propagation of these fractures.
Constant injection fluid viscosity	The injected water viscosity is expected to increase as the reservoir is cooled, but actual increase is hard to quantify. This assumption is therefore discussed as an uncertainty.

3.3.1 Handling Wellbore Friction

A new analysis technique is applied in this thesis which is modified compared to that outlined by Shchipanov et al. (2014). Pressure Transient Analysis has been conducted without wellbore friction by starting the analysis at the end of the Instantaneous Shut-In Pressure (ISIP) (Figure 3.2). This technique decouples rate dependent wellbore and perforation friction effects from reservoir changes. The method does not impact the identified reservoir permeability as seen from the stable derivatives in Figure 3.7, but is key to identifying the reservoir skin effect induced by fractures (black arrow).

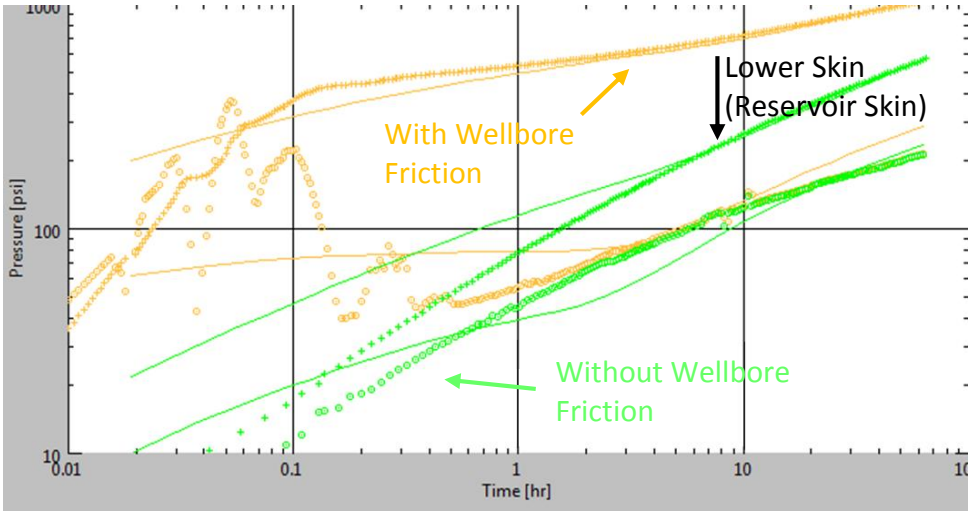

Figure 3.7: The figure is from one of the analyzed datasets in this thesis, and illustrates the difference between PTA with and without wellbore friction. The points show pressures and semi-log derivatives, while the lines are matched reservoir models. The semi-log derivative slopes are the same resulting in the same identified reservoir permeability. The skin is significantly lower when wellbore friction is removed (lower pressure curve, black arrow), which allows for correct identification of fracture skin effect. Illustration is generated using Saphir well test analysis software, Kappa Engineering © 2016.

3.4 Pressure Transient Analysis - Minifrac Step Rate Tests

Alternative to the pressure versus rate (P-Q) analysis outlined in Section 3.2, the minifrac Step Rate Tests are analyzed to examine reservoir behavior under high injection rates and pressures. The method uses Pressure Transient Analysis (Section 3.3) for each injection rate step to determine the reservoir conductivity and skin. The method is applied with a simple assumption of a vertical wellbore. The assumption is a result of the short rate steps seen in minifrac tests, which will give an infinite acting pressure response and therefore be described by a vertical well (Figure 3.8). The model assumptions are outlined in Table 3.3.

Table 3.3: Assumptions applied for Pressure Transient Analysis (PTA) of minifrac Step Rate Tests. The assumptions are applied with a vertical wellbore flow model.

Assumption	Explanation
Reservoir thickness equal to stimulation zone length	The vertical reservoir thickness in the model is assumed equal to the length of the open perforations. Consistent with early radial flow as discussed in Section 3.3.
$\boldsymbol{k_v/k_h = 1}$	No distinction is made between vertical and horizontal permeability. The matched permeability will be close to $\sqrt{k_v \cdot k_h}$
Constant injection fluid viscosity	The reservoir will not be cooled substantially due to the small volumes injected. Fluid properties consistent with original reservoir temperature are therefore assumed.

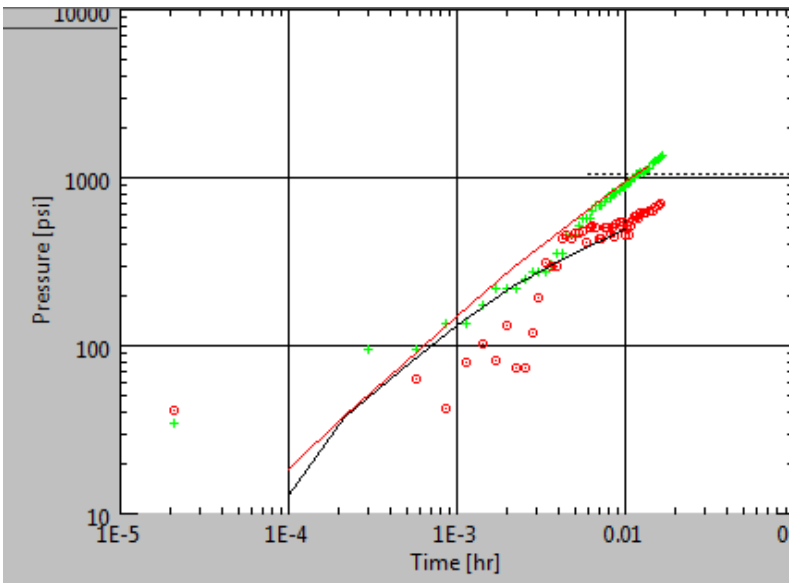

Figure 3.8: Illustration of model match for an analyzed rate step in a minifrac Step Rate Test. The red line shows the pressure match and the black line the semi-log derivative match. The vertical wellbore model gives a good match of the reservoir flow response. The match will be associated with considerable uncertainty as the rate step length is only 1 minute. Illustration generated with Saphir well test analysis software, Kappa Engineering © 2016.

3.5 Reservoir Pressure Determination

3.5.1 Formation Pressure While Drilling

The pore pressure for fracture closure pressure analysis is determined from Formation Pressure While Drilling (FPWD) testers. Pore pressures are measured with a sample probe that extends from the drillstring to the formation. A typical high quality tool test cycle is seen in Figure 3.9. Three pressure drawdowns (1, 2 and 3) are followed by three pressure buildups (A, B and C) as reservoir fluid flows into the tool. The pressure buildups are stable and consistent, and the final pressure in the last buildup (C) is reported as the pore pressure. The final pressure spike during probe release confirms a good seal from the wellbore during the test. Good quality buildups with fluid mobilities consistent with formation properties can be considered as very reliable (Okoroafor et al. 2015).

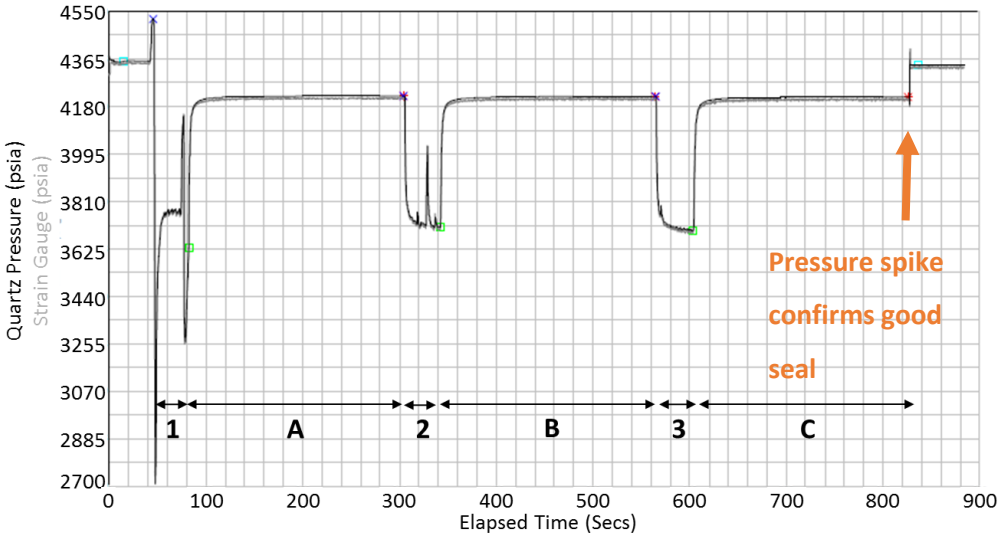

Figure 3.9: Example of high quality Formation Pressure While Drilling test cycle. A good test is characterized by stable and consistent buildups (A, B and C), with confirmed probe seal, as seen from the final pressure spike (orange arrow). The reported pore pressure is the buildup pressure from the last test cycle (C) (Illustration from ConocoPhillips (2015)).

3.5.2 Reservoir Pressure Determination from Falloff Tests

To be able to determine the reservoir pressure development in response to water injection, reservoir pressures are estimate from the injection falloff pressure after 72 hrs and 100 hrs. Due to production influence, the falloff pressures will in theory never stabilize, so a fixed sample point for reservoir pressure is required to be able to compare reservoir pressure development. 72 hours and 100 hrs were picked based on personal communication with Serap Ozoglu-Topdemir (2016) (Reservoir Engineer, ConocoPhillips), as the falloff pressures tend to be relatively stable after this duration of falloff (Figure 3.10). 72/100 hrs was also a practical estimate as several falloffs were within this length and could therefore be compared for reservoir pressure development in time. Injection wells would typically still exhibit linear flow behavior around 72-100 hrs, and shorter falloffs could therefore give reservoir pressure by extrapolating linear flow to 72 hrs or 100 hrs.

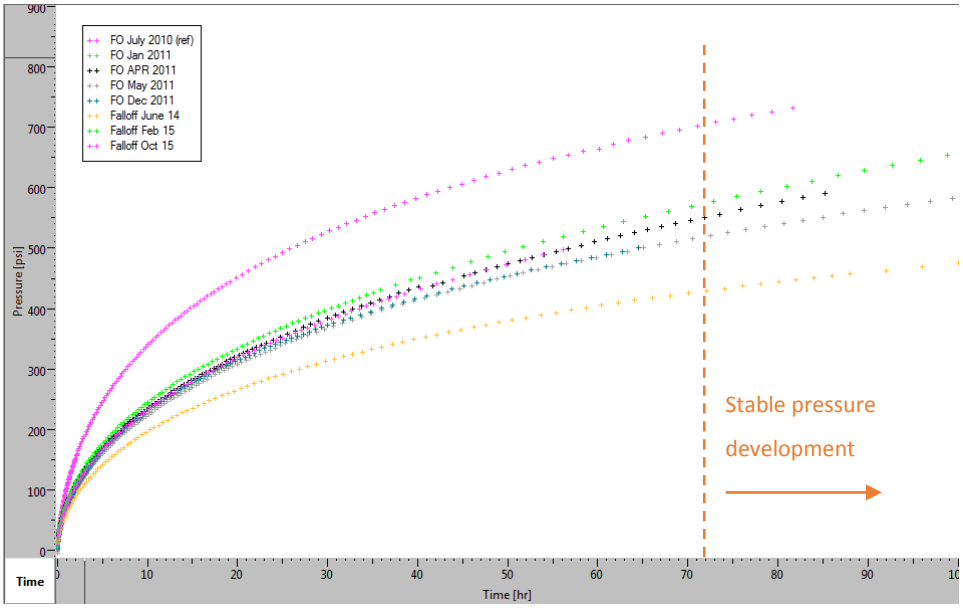

Figure 3.10: The plot shows ΔP vs Δt for falloffs over a period of 5 years. Pressures are relatively stable after 72 hrs with pressures changing at a maximum of 2 psi/hr. The pressure at 72 hrs can therefore be used as a reasonable estimate of the reservoir pressure. Lower permeability wells used reservoir pressure estimate after 100 hrs. Illustration from thesis data.

Figure 3.11 illustrates the use of the technique for determination of reservoir pressure development in an example well. As seen from the figure, the falloff pressure after 72 hrs is comparable to the initial FPWD measurement of reservoir pressure. The pressures are corrected from gauge depth to reservoir depth, and a linear correction is applied calibrating P_{72hrs} with P_{res} using early long falloffs when small reservoir pressure gradients should exist. Due to the low permeability of chalk reservoirs, pressure gradients will persist for a long period of time after injection shut-in, and the objective is to evaluate the reservoir pressure near the injection well as this determines the fracture closure pressure. Correcting the reservoir pressure also accounts for the difference between high pressure in fractures and low matrix pressure.

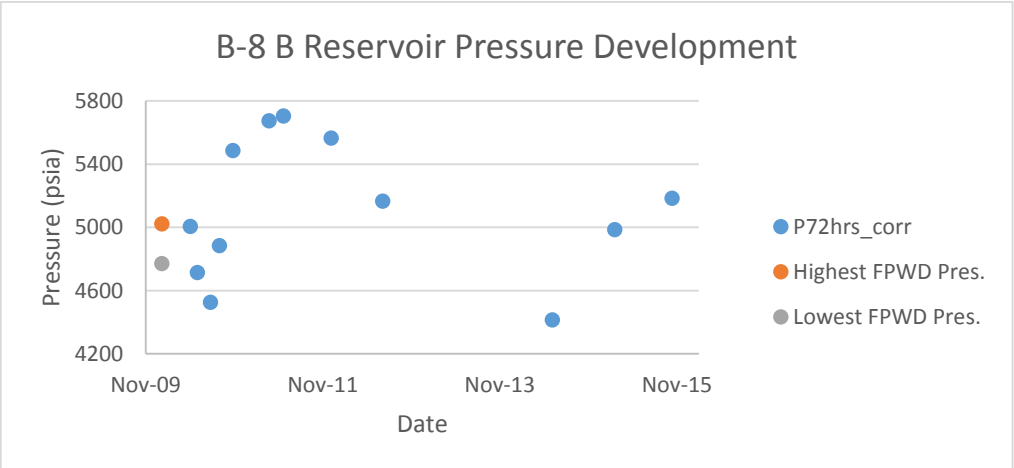

Figure 3.11: Illustration of application of the falloff pressure after 72 hrs as reservoir pressure for well B-8 B. The first reservoir pressure determined from the falloff is comparable with the initial reservoir pressure. The corrected pressure after 72 hrs of falloff can therefore be used as a good indicator of near wellbore reservoir pressure. Illustration from data in thesis.

4 Results

4.1 Eldfisk Fracture Closure Analysis

4.1.1 Eldfisk Closure Pressure Trends

Figure 4.1 shows the fracture closure pressures determined from pre-acid minifrac tests in the Eldfisk S drilling campaign, and one A-well restimulation. A total of 9 Eldfisk S-wells and 1 Eldfisk A-well were analyzed with a total of 32 separate stimulations. The results are compared with the Ekofisk Field closure pressure trend. The linear regression model is obtained assuming negligible error in the determined pore pressure, as pore pressure is determined from direct formation measurements (FPWD, Section 3.3). All points are from zones with mobile oil saturations.

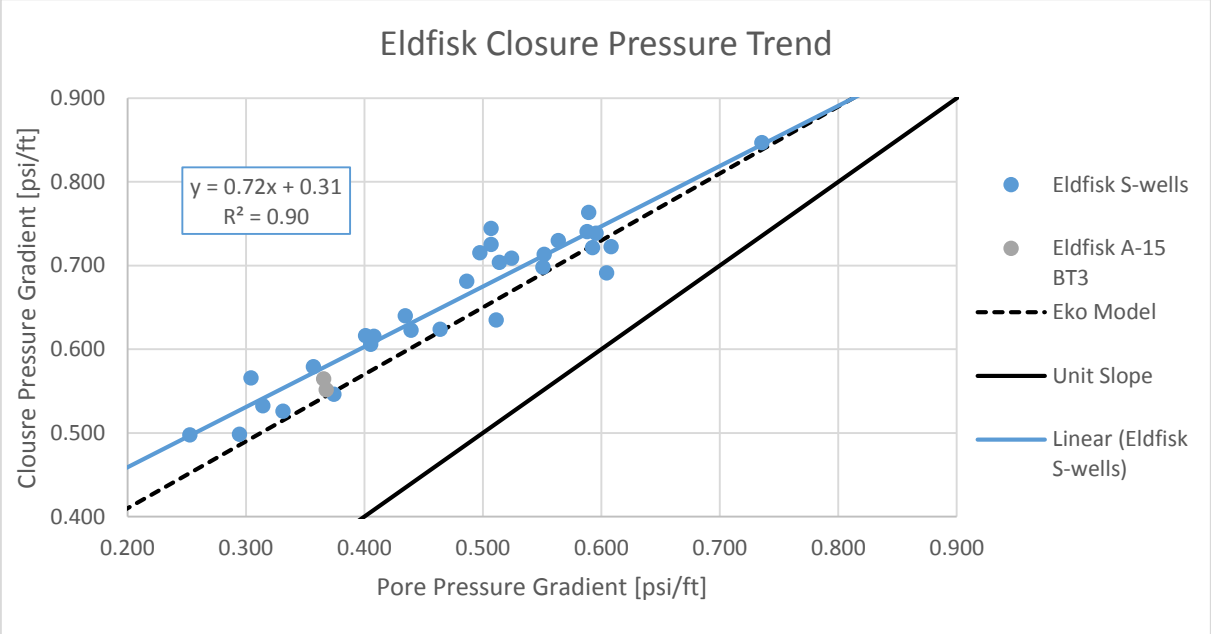

Figure 4.1: Eldfisk closure pressures determined from analysis of pre-acid minifrac injection tests. The results indicate that the Eldfisk closure pressure trend deviates from the Ekofisk trend. Results obtained from restimulation of A-15 BT3 fall within the trend with a maximum error of 5.4 %.

The results show that the Eldfisk closure pressures follow a linear trend as a function of pore pressure. This is in accordance with Equation 2.19 and 2.20 (Section 2.4.1), and suggests reservoir compaction in accordance with the uniaxial compaction model. The linear regression curve (blue curve in Figure 4.1) slope for the S-well data is 0.72 with an intercept of 0.31 psi/ft, and is hereafter referenced as the "new model" or "Eldfisk model" for Eldfisk closure stress. However, it is also important to note that there is significant spread in the observed datapoints, as seen in Figure 4.1 and Figure 4.2, with largest spread in the highest pressure datapoints. This indicates that depletion behavior may conform to the uniaxial compaction model, but repressurization behavior may deviate as discussed in Section 2.5. The A-15 BT3 restimulation datapoints fit within the new Eldfisk closure stress model with a maximum error of 5.4 %, which indicates good predictability of the new model.

Figure 4.2 shows the error chart comparing the prediction of the new Eldfisk linear depletion model, with the model used on the Ekofisk Field. For the Eldfisk dataset shown in Figure 4.1, the new model shows an average error of 0.45 %, while the Ekofisk model shows an average prediction error of -4.2 %. This is expected as the new Eldfisk model is built around the dataset in Figure 4.1. This signifies that there is a significant difference in the depletion stress path (Equation 2.22, Section 2.4.3) followed on the Eldfisk Field compared to the Ekofisk Field.

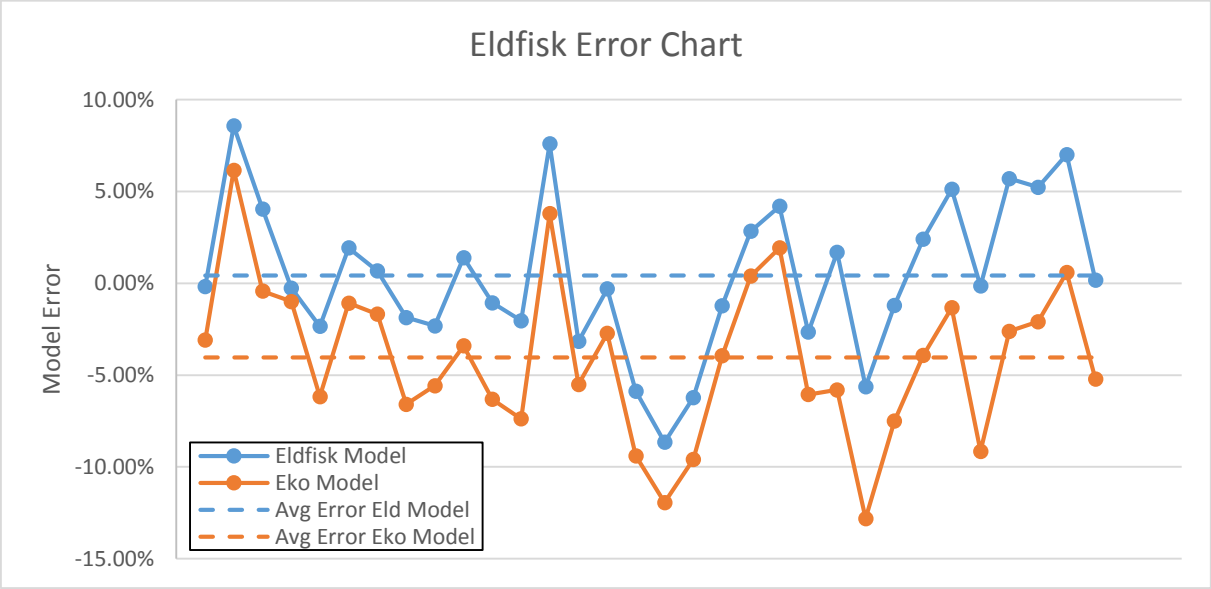

Figure 4.2: Error chart illustrating the improved Eldfisk closure stress model for the dataset in Figure 4.1. The average prediction error with the new model is 0.45 % compared to -4.2 % for the Ekofisk model. This is naturally expected as the new model is built around the new dataset.

4.1.2 Eldfisk Depletion Stress Path – Elastic Properties

Figure 4.1 shows that the Eldfisk minimum effective stress conforms to a depletion trend with a gradient equal to 0.72. Figure 4.3 shows the porosity distribution in the dataset. The majority of the measured closure pressures are from high porosity chalk (85% larger than or equal to 34 % porosity). In accordance with the findings by Teufel and Warpinski (1990) (Section 2.3), chalk of this high porosity would have a Biot stress coefficient close to unity. As a result, the simplified uniaxial compaction model described in Equation 2.19 (Section 2.4.1) should be representative for the

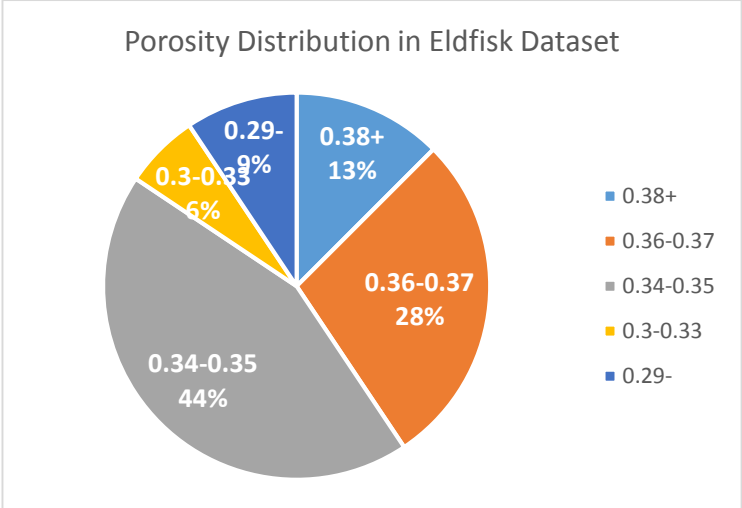

Figure 4.3: Porosity distribution in analyzed dataset shown in Figure 4.1. The majority of the measured closure points are from high porosity oil saturated zones. This puts a bias on the dataset towards high porosity chalk.

dataset, assuming linear elasticity. As discussed in Section 2.1.3.1 and 2.7, pore pressure depletion in high porosity chalk may lead to significant inelastic strains, adding uncertainty to the linear elasticity assumption.

With a Biot stress coefficient (α) close to unity, the results inserted into Equation 2.19 give:

$$A_{pe} = \frac{1-2\nu}{1-\nu}\alpha = \frac{1-2\nu}{1-\nu} = 0.72 \tag{4.1}$$

The results are given in Table 4.1 for the Eldfisk Poisson's ratio and depletion stress path K (0.28) (Equation 2.22), and compared to the Ekofisk depletion stress path (0.2) as given in the Ekofisk model and proposed by Teufel and Rhett (1991).

Table 4.1: Poisson's ratio and stress path K (Section 2.4.3) comparison for the new Eldfisk model and the Ekofisk model

ELDFISK MODEL			EKOFISK MODEL		
A_{pe}	Poisson's Ratio (ν)	Stress Path (K)	A_{pe}	Poisson's Ratio (ν)	Stress Path (K)
0.72	0.22	0.28	0.8	0.17	0.2

The results indicate a larger stress path K (Section 2.4.3) for the Eldfisk depletion trend than Ekofisk, suggesting a larger change in the horizontal effective stress compared to the effective overburden stress. This suggests that the Mohr-circle expansion during depletion of the Eldfisk reservoir will be less than that shown by Teufel and Rhett (1992) for the Ekofisk reservoir (Figure 2.13). Combined with the stress hysteresis concepts outlined in Section 2.5, this may reduce the likelihood of shear failure during repressurization of the Eldfisk reservoir. However, it is important to note that the majority of Ekofisk data is sampled from vertical wells, while the Eldfisk data is from horizontal wells. The deviation may therefore be attributed to uncertainties introduced by the wellbore geometry.

Studies of North Sea reservoir chalks conducted as part of the Joint Chalk Research (JCR) program, showed that the Poisson's ratio is not a function of chalk porosity (Havmøller et al. 1996). Reservoir chalk cores show Poisson's ratios ranging from 0.1 to 0.3, with a mean value of 0.21 and a standard deviation of 0.06. This corresponds well with the determined 0.22 Poisson's ratio for the Eldfisk model (Table 4.1), and indicates that field data is within the range determined from core experiments. However, the calculated Poisson's ratio assumes linear elasticity. As underlined by Teufel (2007) and Teufel and Rhett (1991), field stress paths may not conform to the uniaxial strain assumption due to inelastic deformation effects. Comparing core measured and field calculated Poisson's ratios may therefore not be possible.

4.1.3 Closure Trend Controllers

As outlined in Section 4.1.1, the closure pressures are primarily sampled in high porosity oil filled reservoir zones. This puts a significant bias on the dataset, and may reduce the applicability of the dataset for waterflood evaluation. Despite this, analysis has been conducted to evaluate if porosity, water saturation, type of reservoir formation or structural location control the closure trend.

4.1.3.1 Porosity

Figure 4.4 shows the closure pressure data for the 32 stimulations in Figure 4.1, plotted as a function average zone porosity. The results indicate that the closure pressure trend is not a strong function of porosity. This corresponds well with the findings by Havmøller et al. (1996) (JCR), which indicated that the Poisson's ratio is not a strong function of porosity. However, there is some uncertainty as the porosities are the average for each stimulation zone. The exact porosity at the point of rock failure is unknown and may deviate from the value in the plot.

In Figure 4.4, highest porosities are found in higher pressure zones possibly indicating some pore collapse and therefore inelastic effects in the dataset. This is in accordance with the findings of Teufel and Rhett (1992) for Ekofisk chalk.

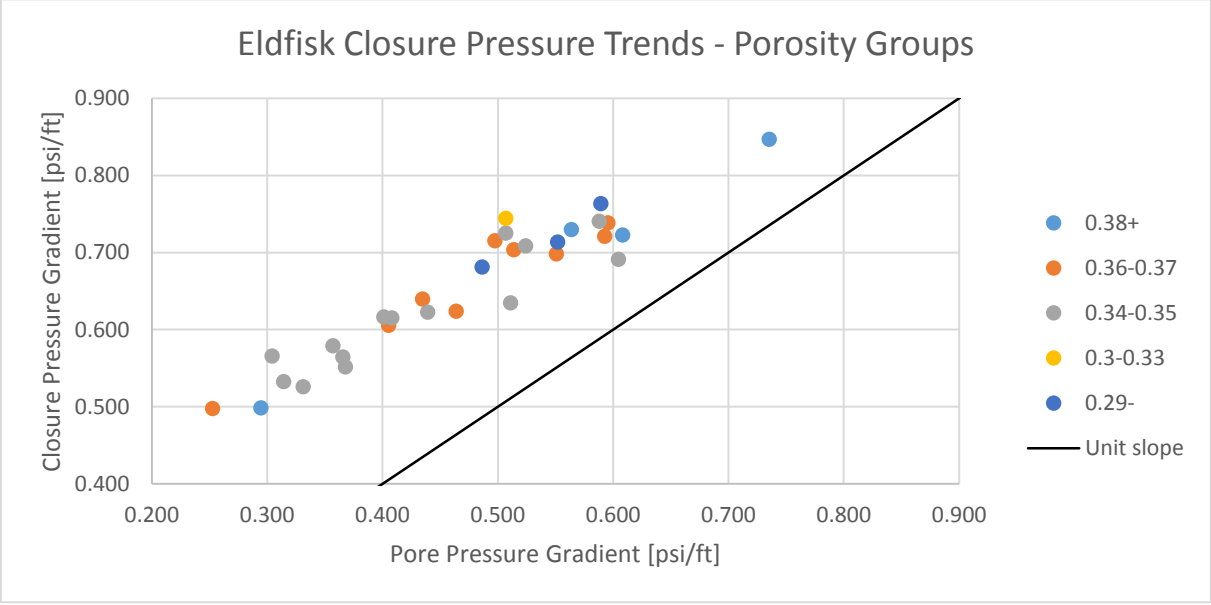

Figure 4.4: Fracture closure pressure vs porosity for the dataset in Figure 4.1. The results do not indicate that porosity is a strong controller of the closure pressure response. This corresponds well with the findings by Havmøller et al. (1996), which showed that the Poisson's ratio is not a function of porosity for North Sea reservoir chalks.

4.1.3.2 Water Saturation

Figure 4.5 shows the plot of closure pressure data as a function of average zone water saturation. In accordance with the stress hysteresis concept in Section 2.5, higher water saturation is expected to result in a decrease in the Poisson's ratio of the chalk (Madland et al. 2002). The results do not indicate

a strong correlation between closure trends and water saturation. As the data is primarily from zones intended for oil production, the water saturations will be too low to expect significant injection water influence. Experiments have shown that very low water saturations (>1-2 %) are required to mobilize the water weakening effect in chalk cores (Madland 1999, Risnes 2001), suggesting that further water weakening requires the influence of seawater. The water saturations in the dataset in Figure 4.5 are too low (minimum water saturation of 3 %) to show influence of seawater, due to the favorable displacement conditions in the reservoir.

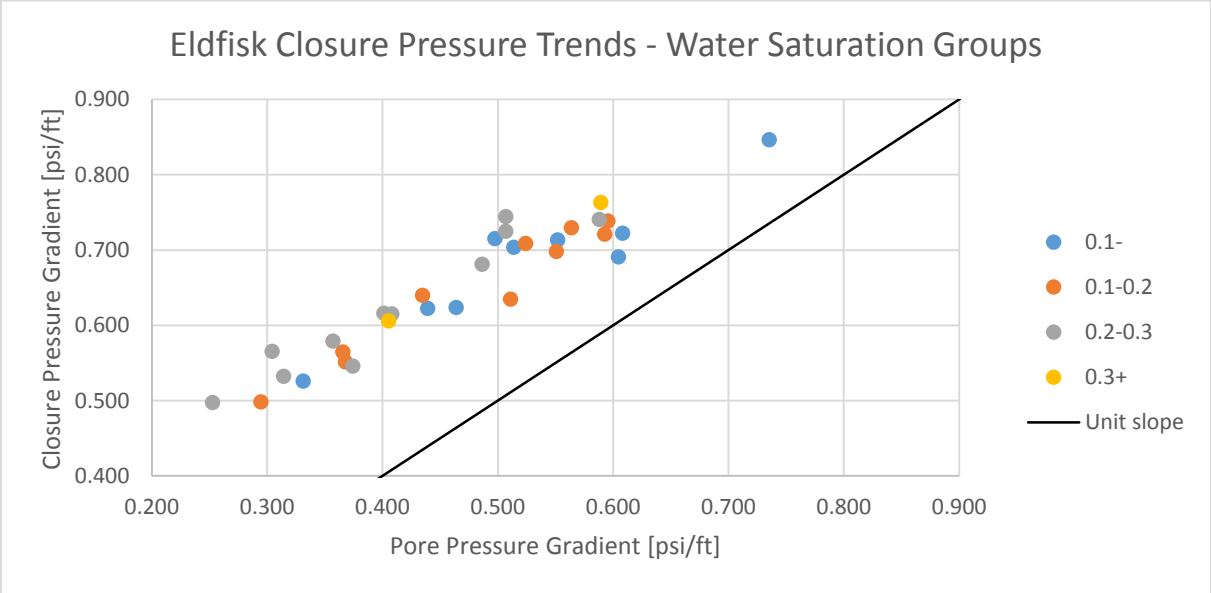

Figure 4.5: Fracture closure pressure as function of water saturation for the dataset in Figure 4.1. The results generally show very low water saturations (minimum water saturation of 3 %), indicative of zones close to initial reservoir conditions with very limited water weakening. The majority of the measurements are from oil producing zones, putting an overall bias on the dataset.

4.1.3.3 Reservoir Formation

Figure 4.6 shows the closure pressure trends plotted as a function of reservoir zones. For most zones, the general data trend indicates good correspondence with the Eldfisk trend (Figure 4.1). The Tor closure pressure trend (light blue Figure 4.6) seems to match the Ekofisk model closely, which may indicate that Eldfisk trend deviation is partly due to high degree of samples from the Ekofisk Formation.

The only zone that indicates substantial deviation is the Upper Ekofisk zone (EU) (grey Figure 4.6). This is a zone with generally lower reservoir quality than the rest of the reservoir, and the pore pressures are depletion pore pressures which have likely not been repressurized. As shown by the linear trend, EU indicates a substantially lower slope (0.57), which, assuming linear elasticity, corresponds to a high Poisson's ratio of 0.30. This Poisson's ratio is in the high end of the 0.1-0.3 range determined by Havmøller et al. (1996) (JCR) for North Sea reservoir chalk. The number of low pressure datapoints in EU is however too small to draw a clear conclusion.

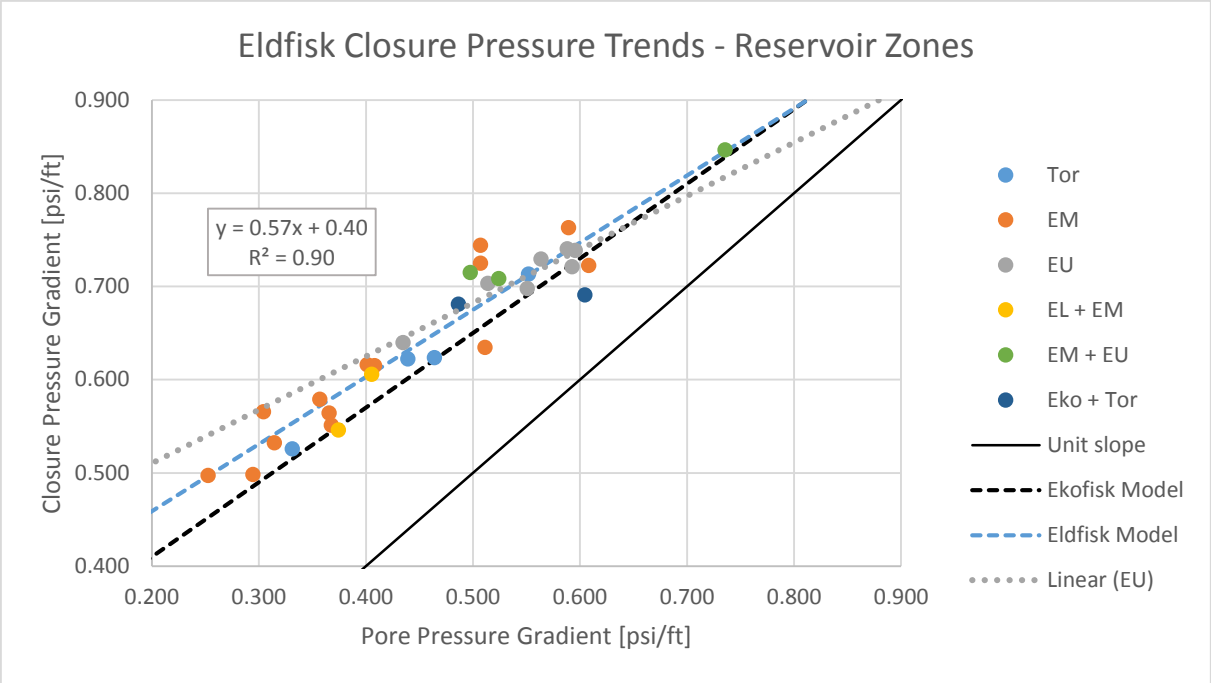

Figure 4.6: Closure pressure trends as a function of reservoir zone for data in Figure 4.1. The reservoir is subdivided into Tor, Lower Ekofisk (EL), Middle Ekofisk (EM) and Upper Ekofisk (EU). Some of the tested zones are commingled with 2 different reservoir zones. Most of the data conforms to a trend similar to the Ekofisk trend, with minor deviations. The data for EU shows a substantial deviation, potentially indicating a substantially higher Poisson's ratio.

4.1.3.4 Structural Location

In reference to the discussion of stress arching in Section 2.4.2 and analysis by Teufel and Rhett (1991), structural location is expected to have an impact on the closure pressure trend. Stress arching with increase of overburden stress on the structural flanks, is expected to lead to a parallel shift of the closure pressure trend. Unfortunately, datasets frequently show an under sampling of the structural flanks due to the poorer reservoir characteristics.

Figure 4.7 shows the closure stress trend as a function of structural location for the analyzed dataset in Figure 4.1. As expected there are significantly more crest than flank datapoints. The data does not indicate a clear deviation with significantly higher closure stress on the flanks than the crest of the structure. This may be due to the relatively low number of sample points, or indicate that stress arching only has a minor impact on the closure stress trends. Alternatively, the shown flank wells, which are producers, are not placed far enough out on the flank to feel the impact of the stress arching, or wells classified as crest wells actually show flank characteristics. Apart from two datapoints, the flank closure stresses (orange) are a few hundred psi above the crestal values (grey) at the same pore pressure, which could be an indication of some arching.

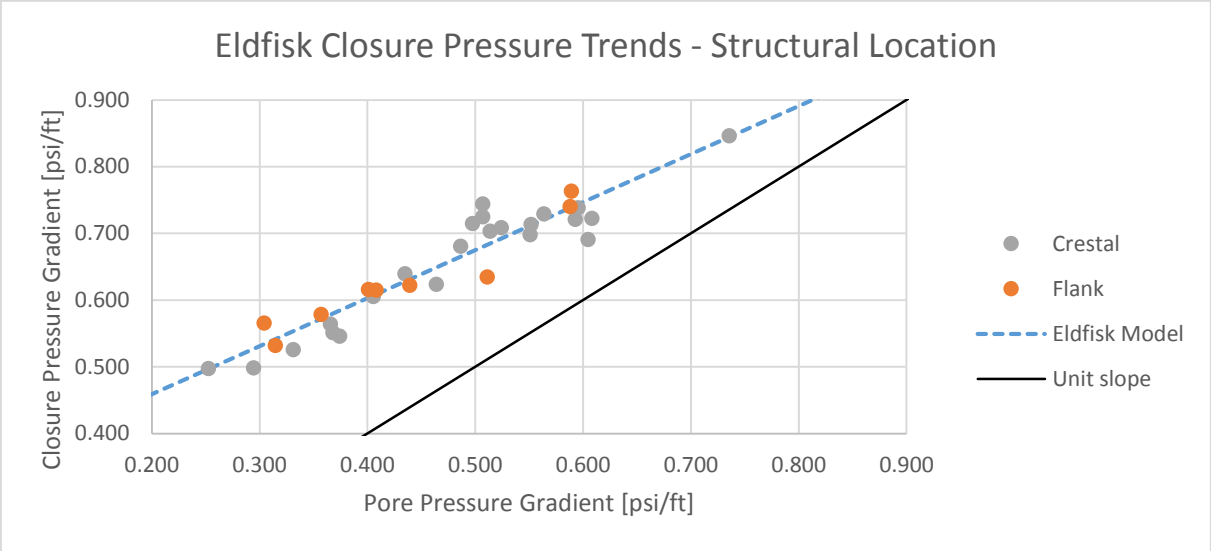

Figure 4.7: Closure stress trends as a function of structural location for the dataset in Figure 4.1. The dataset cannot be said to indicate a clearly higher closure stress trend on the flank than the crest of the structure. Some of the flank datapoints show indications of slightly higher closure stress at constant pore pressure.

4.1.4 Stimulation Impact on Closure Measurements

As discussed in Section 2.8, the objective of acid fracturing stimulation is to etch the surfaces of the fracture such that fracture channels remain open after fracture closure. In accordance with Section 2.2.1.3, the stimulation should only allow for mechanical, but not hydraulic fracture closure. Post-acid (post-stim) falloff results are therefore expected to show fracture closure signature, but may for very effective stimulations not show clear closure as the fractures will largely remain open.

As discussed in Section 2.5 and 2.8, acid fracture stimulation may impact the fracture initiation pressure, but is not expected to significantly impact the fracture closure pressure. A change in fracture closure pressure (minimum effective stress) would require a local shift in the stress equilibrium, which primarily could be induced through changes in the Biot stress coefficient (α). Weak acids could be expected to decrease the degree of cohesion between the chalk grains, due to dissolution of chalk and cement at grain contacts. However, the strong acids (HCl) used in chalk stimulation are only expected to etch surfaces (Section 2.8), resulting in no significant change in the Biot stress coefficient.

Figure 4.8 shows that the pre-acid and post-acid closure pressure measurements on a whole show very little deviation. The only significant change is seen in the lowest reservoir pressure datapoints, where the post-acid points are significantly below the pre-acid points. This may be due to changes in the local stress equilibrium, but may also be attributed to very uncertain closure analysis and no correct observable closure. At low reservoir pressures the post-acid closure pressure analysis was found to be very uncertain, partly due to noise when reservoir pressure is below the hydrostatic column weight. The result may also be attributed to complex stimulation fracture geometry induced by high differential pressures between the fracture and matrix.

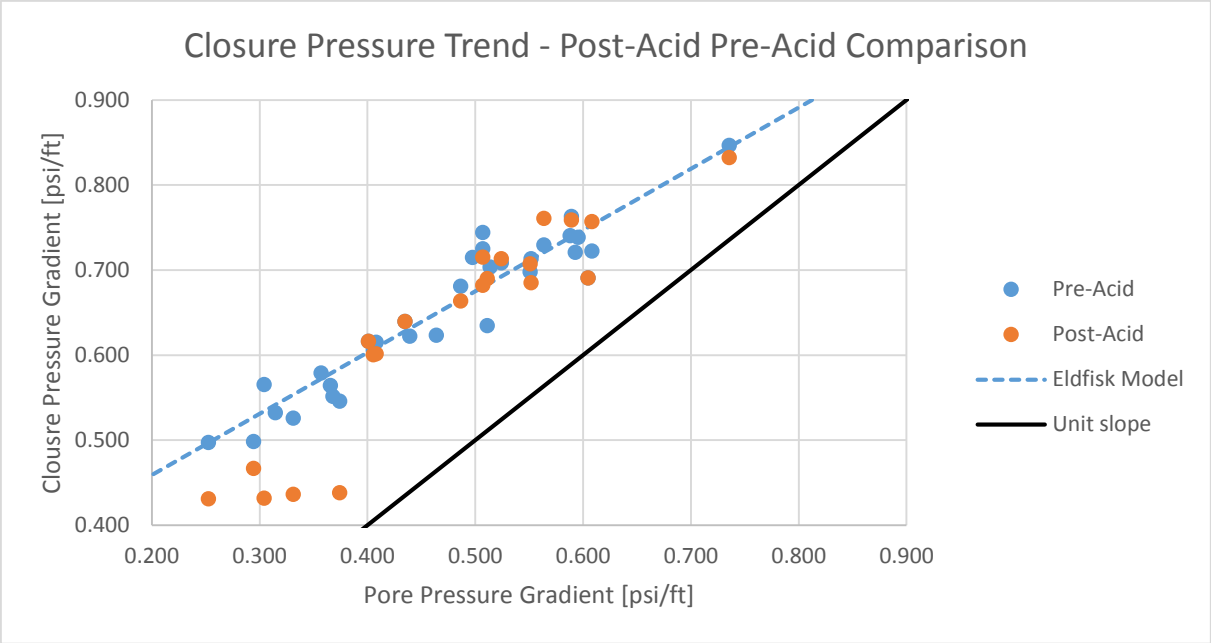

Figure 4.8: Comparison of pre-acid and post-acid closure pressure trends for the dataset in Figure 4.1. The expected behavior is no change as discussed in Section 2.5 and 2.8, and only the very lowest pressure datapoints show a deviation. It is important to note that the lowest pressure closure measurements for the post-acid analysis are uncertain.

4.1.5 Repressurization Stress Path

The dataset in Figure 4.1 indicates that the closure stress data conforms to a linear depletion and repressurization trend. As most of the higher pressure datapoints are repressurized after waterflooding was started in 1999, the data indicates that repressurization follows a similar stress path to depletion.

Figure 4.9 shows the closure stress data from Figure 4.1 highlighting the data from the 6 stimulation zones in the well S-4 (orange). Unlike the general closure trend, S-4 shows almost constant closure stress measurements for all zones, despite 1000 psi pore pressure variations. As the data in general shows a linear closure trend with a slope of 0.72 (Figure 4.1), this may indicate local variations with areas where the repressurized closure stresses show slopes closer to 0. This would conform to Teufel and Rhett (1992), who suggested that areas close to the pressure front would show isotropic repressurization with stress paths closer to unity (Section 2.5). Teufel and Rhett (1992) also suggested that the change in repressurization stress path would be local and therefore not impact the global closure pressure trend seen in Figure 4.1. S-4 is the well in the dataset that is drilled closest to an active injector (650 ft distance), and could therefore reflect local changes in stress paths near injectors.

There is, however, some uncertainty in the trends. Especially the pore pressure at the point of failure in the lower pressure datapoints is uncertain due to 300 psi pore pressure gradients across the zone. There could also be annulus communication preventing zonal isolation in the well. The closure pressure would then be similar for all zones, and representative for the weakest point in the well.

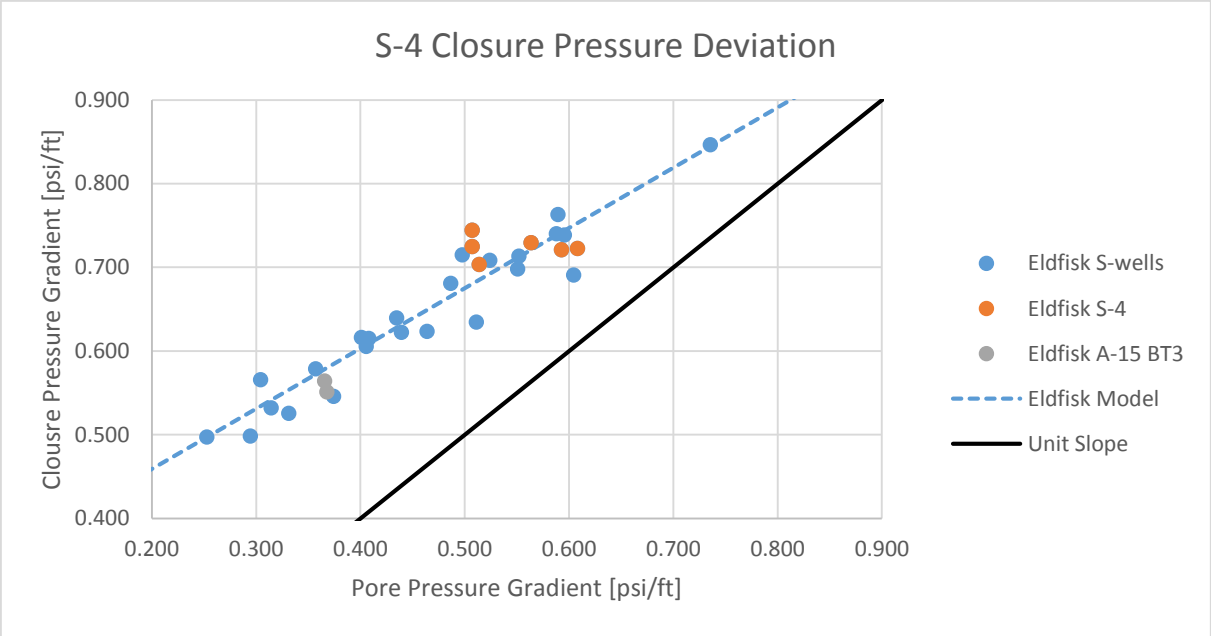

Figure 4.9: Plot of the closure pressure data from Figure 4.1. The well S-4 is highlighted as it shows a clearly deviating closure stress trend. Despite more than 1000 psi pore pressure deviation, all zones show comparable closure stresses. This may be an indication that field wide repressurization conforms to the linear closure stress trend in Figure 4.1, but sees local variation with close to isotropic repressurization. This may, however, also indicate annular communication.

4.1.6 Uncertainty Assessment

The analysis results shown in Sections 4.1.1 through 4.1.5 are associated with uncertainty. The most important uncertainties are highlighted and discussed in the following sections. Section 4.1.6.1 looks at the impact of wellbore geometry on the closure stress trend, while Section 4.1.6.2 evaluates the impact of water hammer features on the determined closure stress. Section 4.1.6.3 looks at the impact of multiple fracture signatures, while Section 4.1.6.4 discusses the uncertainty in the determined pore pressure. Section 4.1.6.5 discusses the impact of the chosen completion, and Section 4.1.6.6 briefly discusses the assumption of linear elasticity in Section 4.1.2.

4.1.6.1 Wellbore Geometry

A limitation of the dataset is that all datapoints are sampled from deviated or horizontal sections. As discussed in Section 2.2.1, the wellbore geometry would primarily influence the measured fracture initiation pressure, but should not influence the measured fracture closure pressure as long as the injection fracture is propagated to an adequate length (Fjær et al. 2008). To validate that the injection fractures are propagated to an adequate length, the closure pressure trends are cross-plotted against wellbore azimuth and inclination (Figure 4.10). Inclination impact on the closure trend cannot be fully validated due to the lack of vertical wellbores in the dataset.

The results show that wellbore azimuth is not a strong controller of the closure pressure trend. However, this conclusion can only be drawn based on data dominated by azimuths between 300 and

340 degrees (red and dark blue Figure 4.10A). Due to the Eldfisk development strategy most wells will be drilled in the same direction, and there are too few deviations to be able to say anything definitive on the impact of wellbore azimuth on the closure pressure trend.

The inclination results show that the wellbores are highly deviated or fully horizontal (70° – 90°), and definitive conclusions on the impact of wellbore inclination cannot be drawn. The results appear to be relatively consistent, with a possible slight indication of trend shift between 85-90 and 90+ degree trends (Figure 4.10). The trend shift is small, with an uncertainty of approximately ±150 psi seen from the figure. Small changes in wellbore azimuth are not expected to significantly impact fracture closure, as the fracture development and geometry will be similar. The deviation may therefore be a result of the natural spread of the dataset, or an indication of deviations possibly caused by the completion design. For wellbores with inclination between 80-85 degrees there may appear to be a deviating trend, but the datapoints are from one well and can be attributed to interpretation uncertainty.

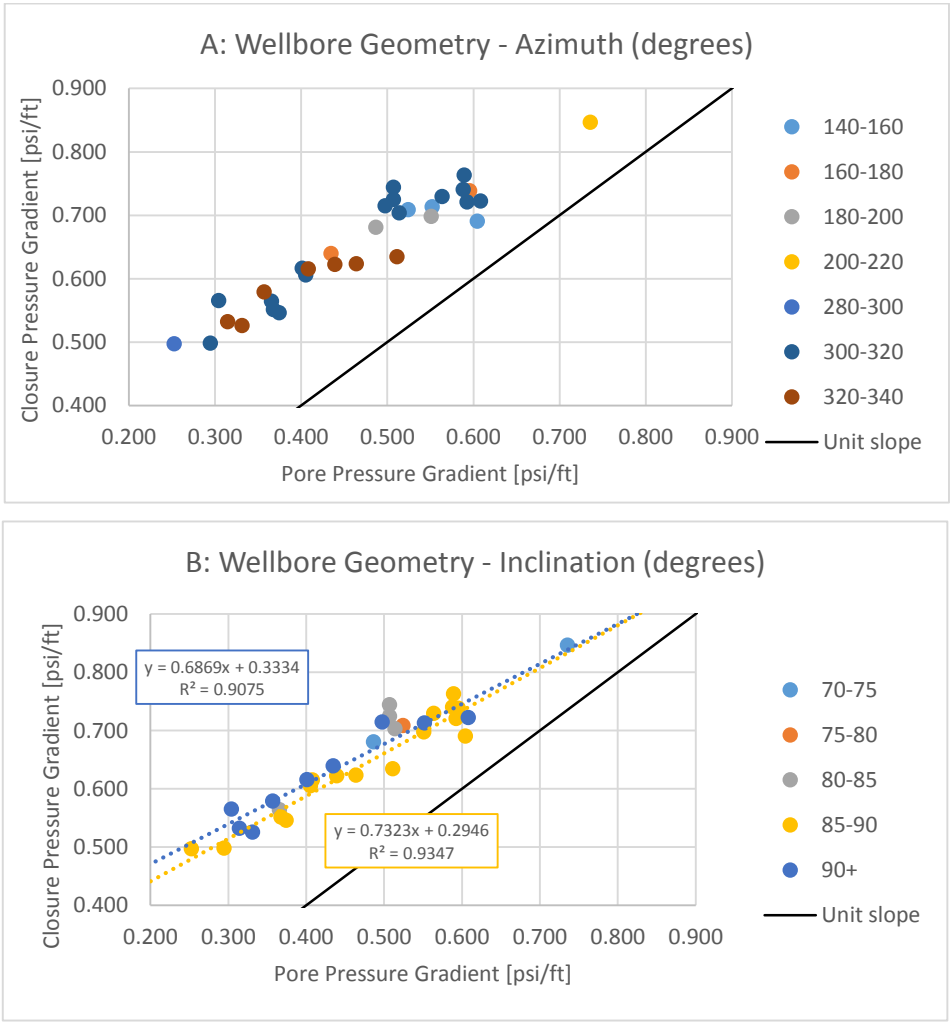

Figure 4.10: Plot of closure pressure trends vs wellbore azimuth (A) and inclination (B) for the dataset in Figure 4.1. Azimuth and inclination are given in degrees. The results do not indicate that wellbore geometry is a strong controller of the closure gradient, however, the inclination data shows primarily horizontal wells indicating that impact of wellbore inclination cannot be properly assessed. The impact of azimuth can neither be properly assessed as most azimuths are between 300-340°.

4.1.6.2 Water Hammer

A water hammer is a pressure transient generated during a hard shut-in, normally caused by a fast closure of a valve. The water hammer travels down the wellbore to the sandface and is reflected back up, causing an attenuating fluctuation in pressure (Mondal 2010). Carey et al. (2015) proposed a method using water hammer signature to describe fracture parameters, due to the water hammers sensitivity to wellbore volume. This method is not applied in this thesis, but underlines the importance of water hammer effects in fracture diagnostics.

Due to the pressure fluctuations caused by the water hammer effect, fracture closure pressure determined with the methods outlined in Section 2.9 will often be subject to significant uncertainty. Several of the interpreted datasets indicate that the water hammer may partially conceal closure (example of water hammer shown by orange arrow Figure 4.11). As a result, some of the interpreted closure pressures may be lower than the actual minimum horizontal stress (Figure 4.11). The uncertainty caused by the water hammer effect is hard to quantify as correct closure is not known, but the example shown in Figure 4.11 shows a water hammer extending over a 300 psi pressure drop. The uncertainty therefore appears to be limited but significant.

The analysis technique outlined by McClure et al. (2016) and described in Section 2.9.3 cannot be applied to determine closure pressure in datasets with significant water hammer disturbance (Figure 4.11). The start of the semi-log linear trend is not visible in datasets with water hammer disturbance, as illustrated in Figure 4.11, which is why the method outlined by Barree et al. (2007) (Sections 2.9.2 and 3.2) is applied in this thesis.

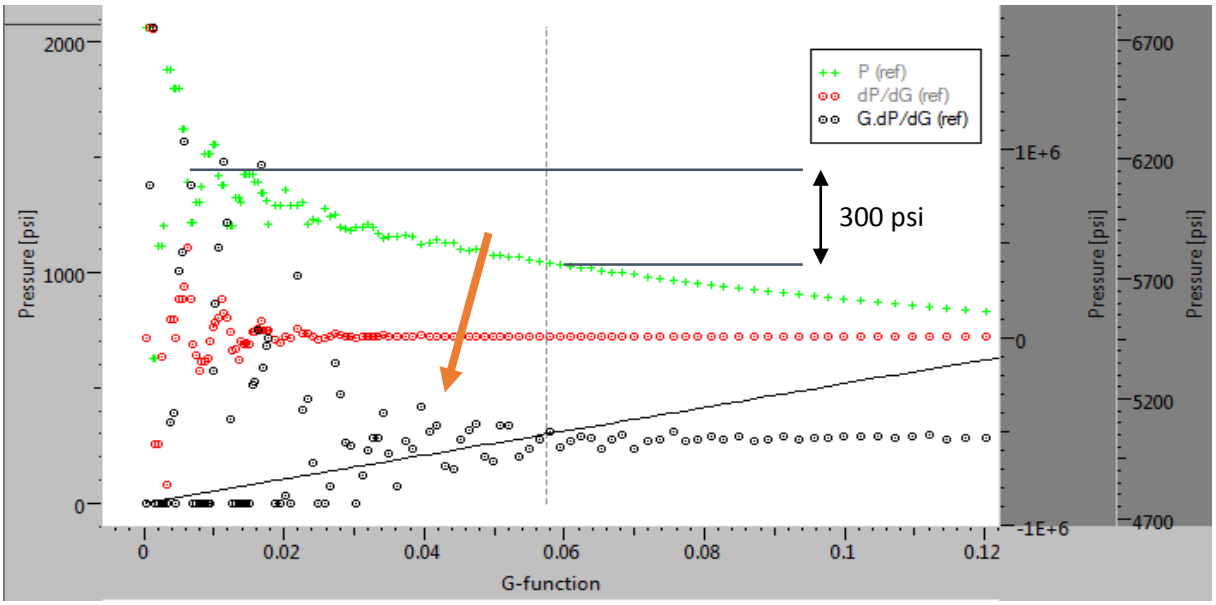

Figure 4.11: Example of extensive water hammer (orange arrow) making closure pressure interpretation uncertain. Example from analysis conducted in this thesis work. The hammer stretches over a 300 psi pressure drop affecting the accuracy of the determined closure. Plot generated with Saphir, Kappa Engineering © 2016.

4.1.6.3 Multiple Fracture Signature

Uncertainty is also added to the evaluation when multiple fractures form such that the falloff analysis shows multiple interpretable closure pressures (black, blue and yellow line in Figure 4.12). The analysis has been conducted assuming that the lowest closure pressure (yellow line in Figure 4.12) represents the first initiated fracture, and that this is the fracture closure pressure representative for the formation. The range in measured closure pressures in Figure 4.12 is 300 psi.

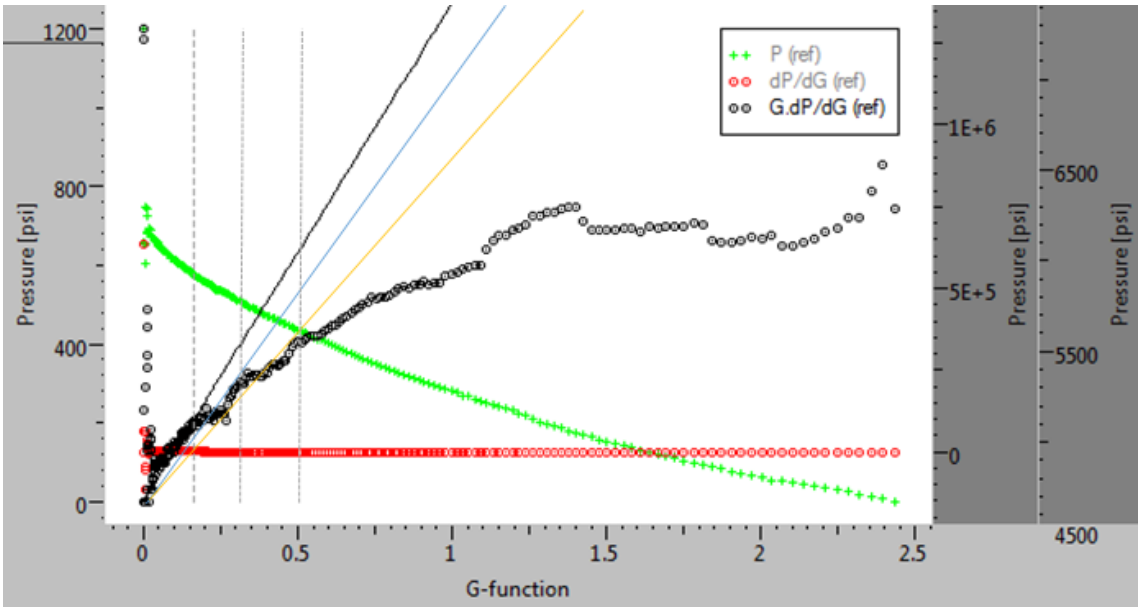

Figure 4.12: Multiple closure signature from dataset analyzed in this thesis work. The lowest pressure (last interpretation, yellow line) is taken to be the correct closure pressure. Range in measured closure pressures is 300 psi. Plot generated with Saphir, Kappa Engineering © 2016.

4.1.6.4 Pore Pressure

Pore pressure will be an uncertainty. As stated in Section 4.1.1, the closure pressure regression analysis assumes significantly less uncertainty in the determined pore pressure than in the closure pressure. All pore pressures are taken from good buildup stability Formation Pressure While Drilling (FPWD) datapoints. Figure 4.13 shows an illustration of a good datapoint, with good and consistent buildup stability (orange arrows). Reservoir connectivity can be confirmed and mobilities are consistent with reservoir properties. The pore pressure can therefore be given with a high degree of certainty, and the closure pressure can be stated to be more uncertain.

However, there will still be an uncertainty in the pore pressure at the point of failure. Normally only a single pore pressure is taken in a zone, which is then assumed applicable for the entire zone. In wells with high pressure differentials along the horizontal, this may not be the case, and as a result the pore pressure at the point of failure may deviate from the measured FPWD pore pressure. Maximum observed pore pressure gradient across a stimulation zone in the dataset is 400 psi, and the gradient in most datasets is much smaller, indicating that the uncertainty is limited.

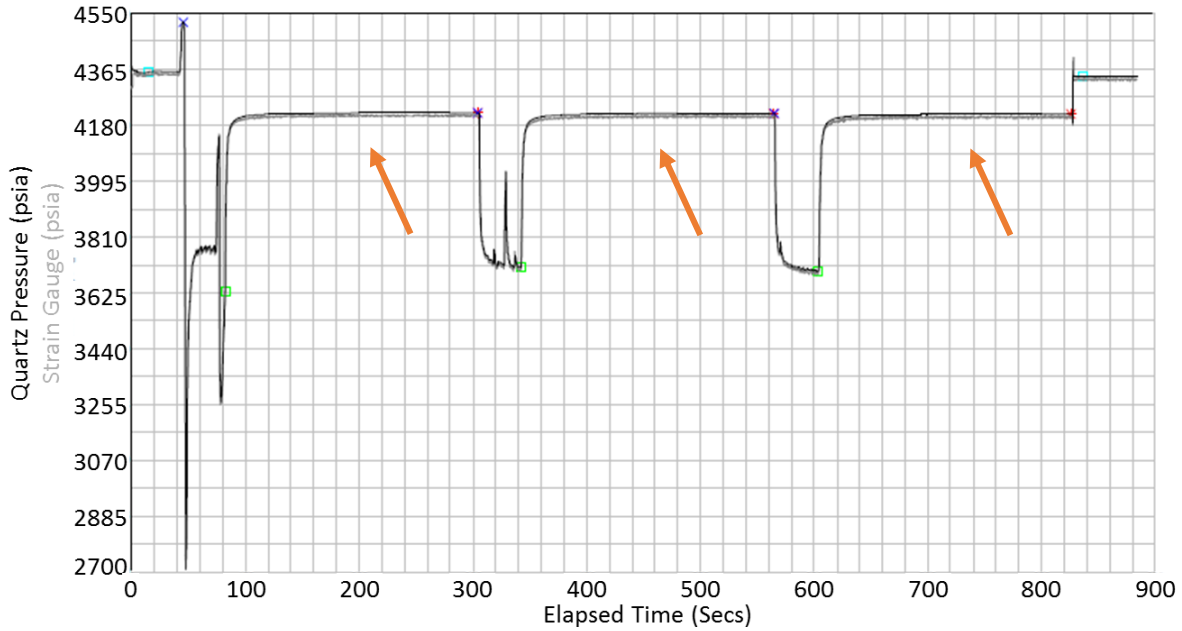

Figure 4.13: Example of pore pressure from a Formation Pressure While Drilling (FPWD) test. Good buildup stability gives reliable low uncertainty pore pressure estimates. (Illustration from ConocoPhillips (2015)).

4.1.6.5 Completion

The completion option also adds uncertainty to the determined closure pressure. This is primarily in terms of which zones that are open, and therefore which pore pressure that should be matched with which closure pressure. One well has a complex sleeve in sleeve completion which means that more "perforations" are opened during the pumping operation. Experience shows that multiple pre-acid pumping cycles are required to open the sleeves, and each cycle gives a different closure pressure estimate. In accordance with Section 4.1.6.3, the lowest reliable closure pressure estimate was used as an estimate for the fracture closure pressure in the stimulation zone.

4.1.6.6 Linear Elasticity

The assumption of linear elasticity applied in Section 4.1.2 will be discussed further in Section 5.3. The linear closure stress trend seen in Figure 4.1 in Section 4.1.1 can be interpreted as an indication of linear elastic behavior. However, the porosities in Section 4.1.3.1 indicate that pore collapse has occurred in the reservoir during depletion. These plastic deformation effects are likely to impact the closure trend in Figure 4.1, and the determined 0.22 Poisson's ratio in Section 4.1.2 may therefore not be representative for the elastic deformation regime. Teufel and Warpinski (1990) concluded that nonlinearities invalidate most theoretical and mechanistic models, indicating that plastic deformation invalidates the application of uniaxial compaction models. Furthermore, Omdal et al. (2009) referenced to Risnes and Nygaard (1999), who indicated that linear elastic models only have limited applicability in chalk.

4.2 Fracture Initiation Pressure

4.2.1 Determining Fracture Initiation

Fracture initiation pressure was estimated based on the pressure vs rate (P-Q) analysis approach outlined in Section 2.10.1. Out of total of 32 analyzed Step Rate Tests (SRTs), only 10 allowed for a confident estimate of fracture initiation pressure. The 10 analyzed datasets covered the entire pore pressure range, enabling good estimates of fracture initiation pressure dependency on pore pressure.

Fracture initiation pressure was determined by correcting Bottom Hole Pressures (BHP) to sandface pressures by removing flow friction components and adding hydrostatic components. Figure 4.14 illustrates the determination of fracture initiation pressure for one Step Rate Test. The correction to sandface pressure is most important at high rates where the friction component becomes large.

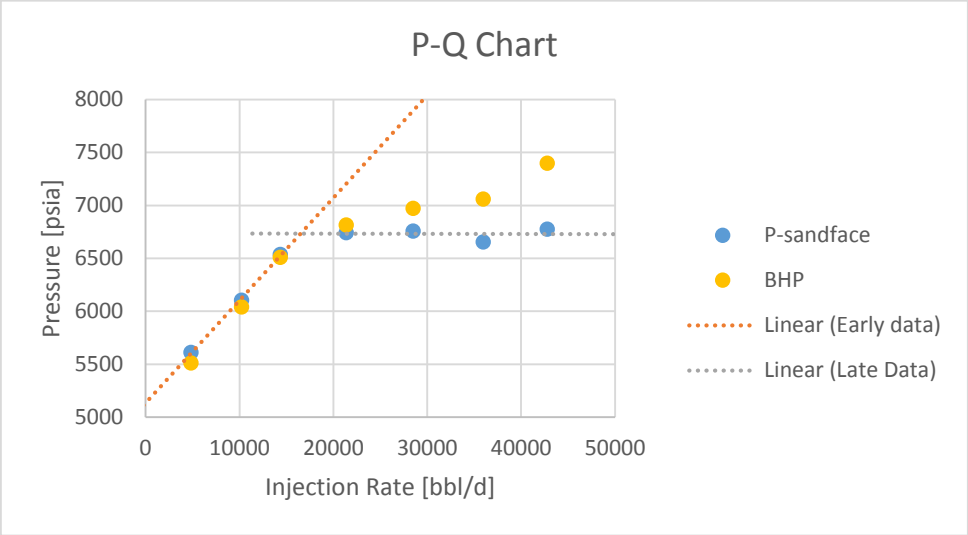

Figure 4.14: Example of pressure vs rate (P-Q) analysis conducted in this thesis to determine fracture initiation pressure. The fracture initiation pressure is determined at the intercept between the two straight line trends. The chart also illustrates the correction from BHP to pressure at the sandface (P-sandface). Correction to pressure at the sandface is most important for high flow rates where the friction component becomes large.

4.2.2 Fracture Initiation Results

The fracturing differential pressure is defined as the fracture initiation pressure minus the fracture closure pressure. This is a measurement of the excess pressure above the closure pressure that is required to initiate a fracture (Section 2.2.1.1).

Figure 4.16 shows the fracturing differential pressure for the 10 analyzed datasets. The results show no correlation with pore pressure and have an average of 615 psi. Apart from two deviations, one high differential of 1000 psi and one low of 130 psi, the deviations are mostly within ±150 psi of the mean. The high outlier has a closure pressure deviating on the low side of the trend determined in Section 4.1.1, and may simply be a result of uncertainty in the closure estimate. The low outlier has a jump in the Step Rate Test data, and the fracture initiation pressure therefore has an uncertainty of ±200 psi.

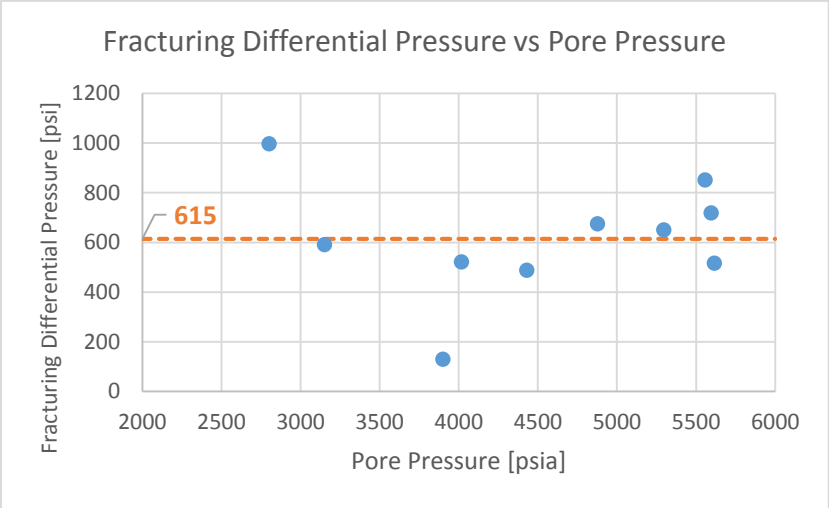

Figure 4.15: Plot of fracturing differential pressure vs pore pressure for the 10 analyzed datasets. The plot shows that the difference between the fracture initiation pressure and the fracture closure pressure shows no correlation with the pore pressure. The difference is relatively consistent with an average of 615 psi.

The standard deviation excluding the two outliers is ±120 psi. The results of the analysis can therefore be given as a fracturing differential pressure of 600 psi within an uncertainty of ±150 psi for the dataset. As the wells are perforated, Lost Circulation Material used during drilling will have a limited effect and these determined values should therefore be representative of the fracture reopening pressure assuming 0 tensile strength (Section 2.2.1.4).

4.2.3 Analysis Uncertainty

It is important to note that the fracture initiation pressure is associated with uncertainty. The main uncertainties are shown below. These uncertainties will also impact the PTA outlined in Section 4.3.

Table 4.2: Outline of uncertainties in pressure vs rate (P-Q) analysis of fracture initiation pressure in this thesis.

P-Q Analysis Uncertainty	Explanation
Rate step length	Rate steps may vary in length by 5-6 times, leading to different degree of stabilization (Section 2.10.1).
Friction reducer assumptions	Friction calculations assume same friction reducer efficiency at all rates.
Perforation friction assumptions	Perforation friction calculations assume same number of perforations open at all rates.
Closure pressure uncertainty	Section 4.1.5
Fracture initiation pick	Consistent method is applied, but there may be some uncertainty as illustrated by the low point in Figure 4.15.

4.3 Pressure Transient Analysis – Minifrac Step Rate Tests

4.3.1 Results Outline

As part of this thesis project, an objective was to study the potential application of Pressure Transient Analysis (PTA) techniques for minifrac Step Rate Test evaluation (Section 3.4). The results show applicability, but only in a limited number of datasets. Out of 32 pre-acid Step Rate Tests, only five tests were deemed to have the data quality required for PTA, and the analysis results have considerable uncertainty as illustrated in Section 4.3.3.

Figure 4.16 shows a minifrac dataset with data quality adequate for PTA, the Bottom Hole Pressure (BHP) is shown in green, with the model match in red and injection rates in orange. As shown by the good model match of the pressure history, pressure transient evaluation of minifrac Step Rate Tests is possible, and can give reliable estimates of reservoir properties.

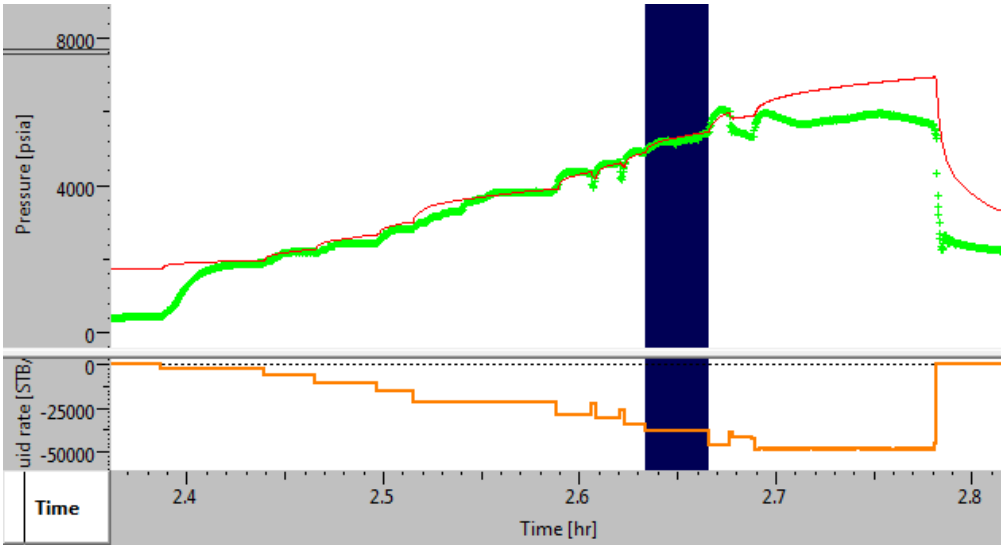

Figure 4.16: Example of Pressure Transient Analysis applied to a good quality Step Rate Test in this thesis work. The model match (red) shows that reliable estimates of reservoir properties can be obtained through PTA. Bottom Hole Pressure (BHP) shown in green, injection rates in orange. Plot generated with Saphir, Kappa Engineering © 2016.

4.3.2 Dynamic Reservoir Permeability Response

4.3.2.1 Example of Dynamic Reservoir Response

Figure 4.17 illustrates the permeability response determined for one of the five analyzed tests. The results clearly show a significant increase in permeability with increasing BHP (blue curve). This suggests multiple tensile fracture growth or fracture network expansion in the reservoir. The uncertainty in the degree of conductivity change is significant, as seen from the minimum (orange) and maximum permeabilities (grey), reflecting the limitation imposed by the short duration of minifrac Step Rate Tests (Section 3.4). However, all curves support the conclusion of increased permeability with increasing BHP (Figure 4.17).

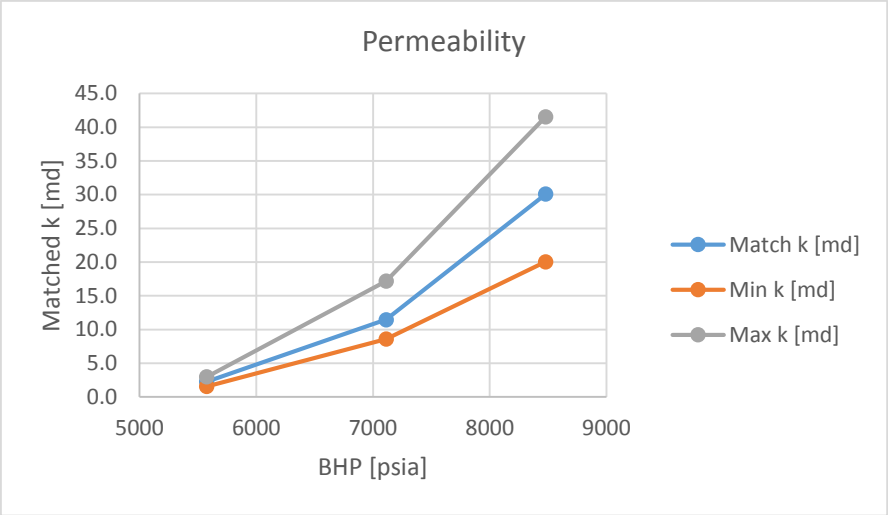

Figure 4.17: Illustration showing results of a minifrac Pressure Transient Analysis conducted in this thesis work (INJ3 ZE Section 4.3.2.2). The analyzed zone shows a significant increase in reservoir permeability with increase in injection pressure.

The results in Figure 4.17 illustrate that the permeability response of chalk can be dynamic when injecting at high pressure and rates. The permeability increases from a matrix dominated response (1.6 – 3 mD) to a fracture flow dominated response (20 – 40 mD). This feature enhances the injectivity of the injector, improving overall injector performance.

Figure 4.18 shows the analyzed skin development with uncertainty for the same stimulation. If no tensile fractures are formed, skin will increase due to the effect of perforation friction on the wellbore pressure. This increase is observed in all curves from 5000 to 7100 psia, but reversed when the Bottom Hole Pressure (BHP) exceeds 7100 psia and tensile fractures are formed. The results therefore show propagation of tensile injection fractures combined with a dynamic increase in permeability. This indicates injection at pressures above the fracture initiation pressure and possibly connection to and expansion of natural fracture networks, or growth of multiple tensile fractures.

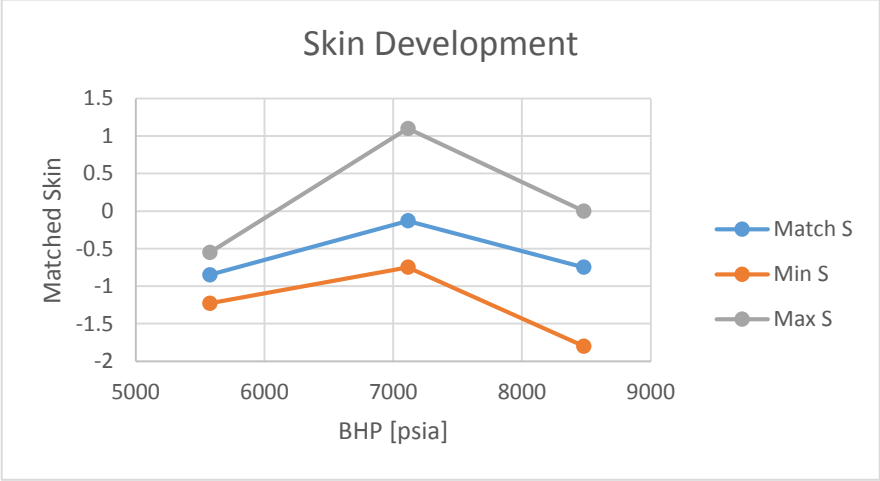

Figure 4.18: Illustration of skin development for the analyzed well shown in Figure 4.17. The decrease in skin for BHP exceeding 7100 psia illustrates the forming of tensile injection fractures.

4.3.2.2 Fracture Propagation and Permeability Response

To understand the trends seen in Section 4.3.2.1 it is important to consider the concept of sandface pressure (Section 4.2.1). The sandface injection pressure is the actual pressure felt by the chalk during the injection. This pressure is equivalent to the pressure that would have been measured on the outside of the perforations in an injection well. The correction from BHP to sandface pressure is described in Section 4.2.1.

Figure 4.19 shows a plot of the data from Figure 4.17 against the difference between the sandface pressure and the determined fracture closure pressure. Referencing to Section 2.1.3.3, once the sandface pressure exceeds the closure stress the effective stress will be tensile. The data clearly shows that once the sandface pressure exceeds the closure pressure by ~750 psi, fractures are initiated and propagate, leading to an increase in conductivity as well as a reduction in skin (Figure 4.17 and Figure 4.18). As the increase in permeability is associated with pressure significantly exceeding the closure stress, the permeability increase appears to be connected to the fracture growth process and not natural fracture network expansion. This suggests either multiple fracture growth, or possible growth of transverse injection fractures enhancing the reservoir conductivity (Teufel et al. 1993). The data does not show a significant difference between the fracture initiation pressure and the fracture propagation pressure (Section 2.2.1.2) at the sandface, as the sandface pressure remains relatively constant once a fracture is initiated. Once the fracture propagates the conductivity and fracture area will increase, which results in a constant sandface injection pressure despite significantly increased injection rate (24 000 bbl/D – 75 000 bbl/D).

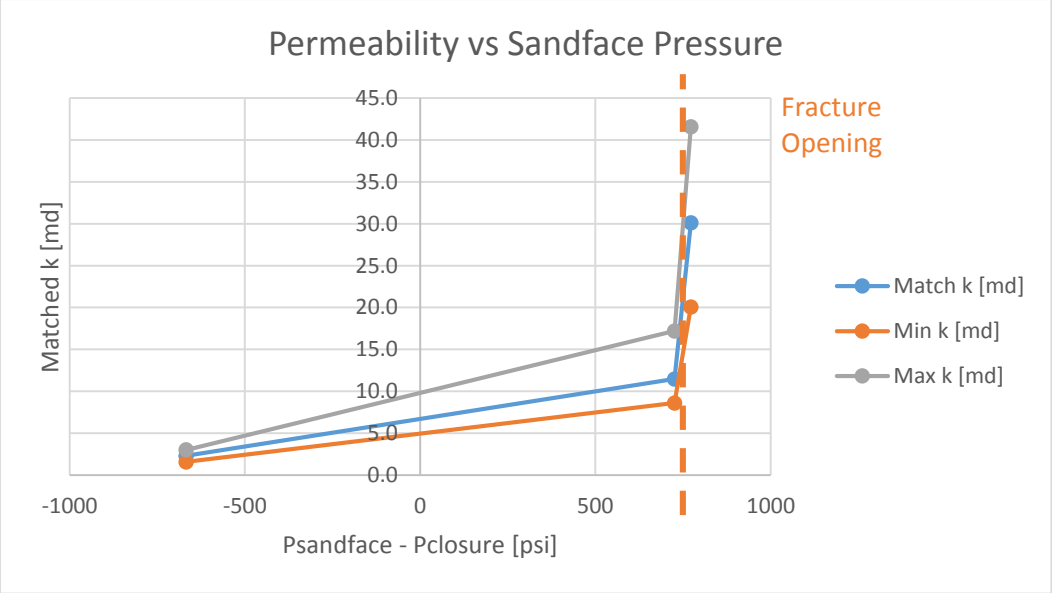

Figure 4.19: Illustration shows the excess pressure required to open and propagate a fracture. The sandface pressure needs to exceed the closure pressure by ~750 psi to initiate and propagate a fracture. Once the fracture starts propagating the injection rate will increase without an increase in sandface pressure due to the increased leakoff rate of the fracture.

4.3.2.3 Dynamic and Static Reservoir Conductivity

Figure 4.20 shows a plot of conductivity multipliers for all the analyzed stimulations. The results clearly show that not all zones exhibit dynamic reservoir conductivity response. Section 4.3.2.3.1 examines INJ1 (light blue), INJ2 ZC (orange) and INJ3 ZE (dark blue) which all show permeability that increases by 11-13 times the original value. Section 4.3.2.3.2 looks at INJ3 ZA (grey) and INJ3 ZC (yellow) which on the other hand only show small increase in permeability (2-3 times). Fractures are formed in all of the tests, as fracture closure is observed in the following falloff. The difference in degree of conductivity increase may therefore indicate differences in fracture mechanics.

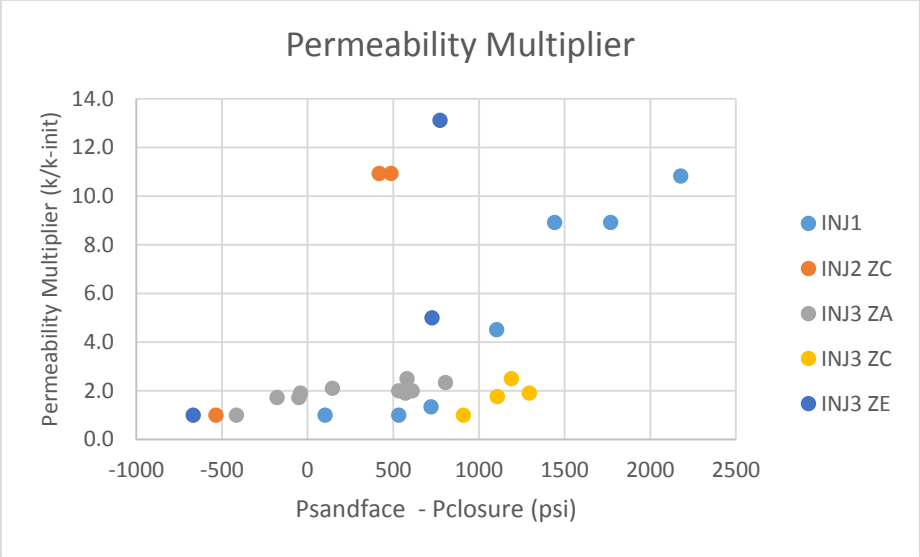

Figure 4.20: Plot of permeability multiplier vs difference between sandface pressure and closure pressure for all analyzed wells. The permeability multiplier is defined relative to the initial matched permeability for each well. The results show that while three of the analyzed tests (INJ1, INJ2 ZC and INJ3 ZE) show increased reservoir permeability, two zones (INJ3 ZA and INJ3 ZC) show limited change. Abbreviations: ZA – Zone A, ZC – Zone C, ZE – Zone E.

4.3.2.3.1 Dynamic Conductivity Response

INJ1, INJ2 ZC and INJ3 ZE (Figure 4.20) all show dynamic reservoir conductivity response. INJ2 ZC shows fracture opening at pressures as low as ~450 psi above fracture closure pressure, giving a significant conductivity increase (~11 times). However, once the fracture starts propagating there is no increase in permeability. This may indicate local shear failure around the wellbore prior to tensile fracture propagation, with no significant failure after the fracture starts propagating. Based on discussions in Section 2.5, shear failure may be likely in this well as the pore pressure is 600-1000 psi lower than INJ1 and INJ3 ZE, respectively.

INJ1 shows a progressive increase in conductivity once the sandface pressure exceeds the fracture closure pressure by ~1000 psi. The gradual increase in sandface pressure indicates no major fracture growth, suggesting that the permeability is enhanced by shear failure. As the shear failure zone propagates away from the well it gives a progressive increase in reservoir permeability. Alternatively,

multiple small fractures form, or the natural fracture systems expand. The conductivity of each fracture may then be limited and require higher pressure to increase the fracture aperture and give higher conductivity (Teufel et al. 1993).

INJ3 ZE is discussed in Sections 4.3.2.1 and 4.3.2.2, and shows a response intermediate between INJ1 and INJ2 ZC, with a gradual increase in permeability at relatively constant 750 psi difference between the sandface pressure and the closure pressure (Figure 4.20). This may, as discussed in Section 4.3.2.2, indicate multiple fracture growth with small differences between the initiation pressure of each fracture, or be due to gradual shear failure occurring at pressures close to the fracture initiation pressure.

Pore pressure appears to be a potential important controller of the conductivity increase. Figure 4.21 indicates that for the wells that show dynamic reservoir conductivity, the response starts once the difference between the sandface and pore pressure exceed ~2400 psi. This suggests that expansion of the natural fracture network could be a function of the pressure difference between the induced fracture and the matrix. This could also indicate a constant difference between the fracture initiation pressure and the pore pressure at the pressure front. As Section 4.2 showed a constant difference between the fracture initiation and the fracture closure pressure, this would give a constant difference between the fracture closure pressure and pore pressure at the pressure front. Potentially indicating a stress path K (Section 2.4.3) equal to 0 at the injection front, as the change in horizontal stress would be equal to the change in pore pressure. This would be opposite of the isotropic repressurization at the front postulated by Teufel and Rhett (1992).

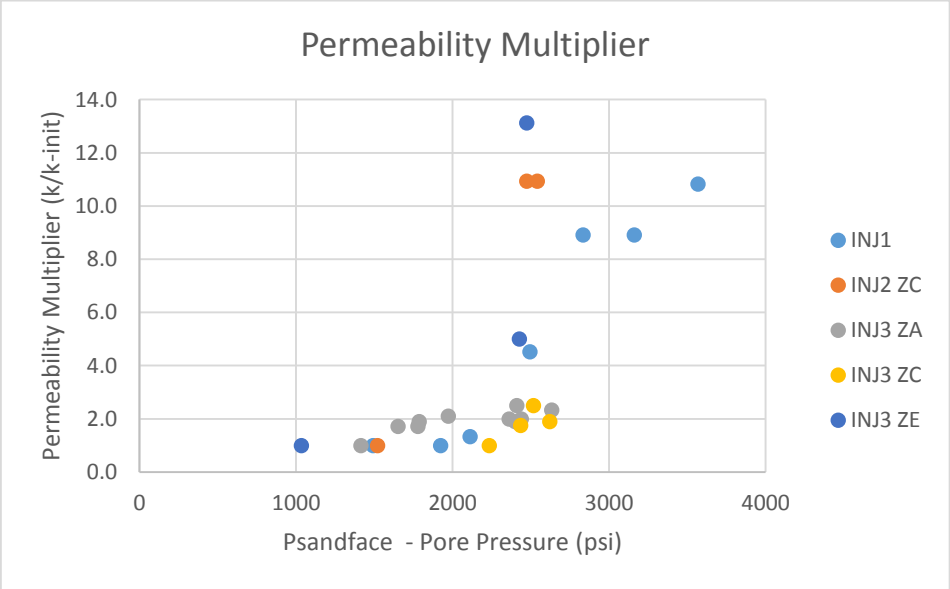

Figure 4.21: Permeability vs sandface pressure – pore pressure difference for the analyzed wells. The results indicate that pore pressure is a potential controller of the permeability increase, as increase does not occur until the difference between sandface pressure and pore pressure exceed ~2400 psi.

4.3.2.3.2 Static Response

INJ3 ZA and ZC (grey and yellow in Figure 4.20, respectively) show no significant dynamic conductivity response. This may simply be an indication of higher tensile formation strength in these zones, or single zones of weakness resulting in only a single formed fracture. Especially in INJ3 ZA, the maximum analyzed sandface pressure minus closure pressure (grey Figure 4.20) is below the pressure difference required for conductivity increase in INJ1 (light blue in Figure 4.20), and stresses may not be large enough to create multiple fracture networks.

However, Table 4.3 illustrates one of the limitations in field data analysis. The perforation lengths of the analyzed zones vary significantly, and the zones that show static conductivity response are 3-10 times shorter (yellow shading Table 4.3) than the other stimulation zones. Longer stimulation zones will give a response which may contain multiple failures and different failure modes, while the thinner stimulation zones can be expected to give more unique reservoir data. This is especially important for pore pressure which is normally taken with just one sample in each stimulation zone. The pore pressure in the failed section of the longer stimulation zones (INJ1, INJ2 ZC and INJ3 ZE) may therefore be lower, such that the difference between the sandface and pore pressure is higher than the maximum difference of ~2600 psi seen in INJ3 ZA and ZC. In which case permeability increase would not be expected at the sandface pressures seen in INJ3 ZA and ZC. These considerations may indicate that there is a critical pressure difference required between the formed tensile fracture and the matrix pore pressure to form transverse tensile fractures increasing the reservoir conductivity.

Table 4.3: Perforation length comparison for Pressure Transient Analyzed minifrac zones. The highlighted zones (yellow shading) show no significant change in permeability as tensile fractures are formed (static permeability).

	INJ1	INJ2 ZC	INJ3 ZA	INJ3 ZC	INJ3 ZE
Perf. length [ft]	660	640	113.6	61.7	349

Alternatively, the static permeability zones represent zones with only tensile failure and no expansion of the natural fracture network or shear failure. As a result, the propagating fractures only impact the reservoir skin while the permeability is primarily matrix dominated. This conclusion would indicate that thinner more isolated sections of the reservoir are more competent in terms of shear failure, or that these zones show less natural fractures. Alternatively, thinner zones show the true impact of propagating injection fractures, which is to reduce the skin by improving connectivity, while the thicker zones show that multiple fracture growth gives an apparent enhancement of the reservoir conductivity.

4.3.3 Analysis Uncertainty

As shown in Figure 4.17, the conducted minifrac Pressure Transient Analysis is associated with significant uncertainty. This interpretation uncertainty comes in addition to the uncertainties outlined in Table 4.2 (Section 4.2.3) and uncertainties due to the assumptions in Table 3.3 (Section 3.4). Figure 4.22 shows the uncertainty span for the analyzed stimulations. The uncertainties are especially large for the wells that show conductivity increase, as the rate steps are short and the changes in pressure very small at higher reservoir conductivities. Despite the uncertainties, the results still indicate that three zones (INJ1, INJ2 ZC and INJ3 ZE Figure 4.22) show significant increase in permeability, while two zones show relative stable permeability (INJ3 ZA and INJ3 ZC Figure 4.22).

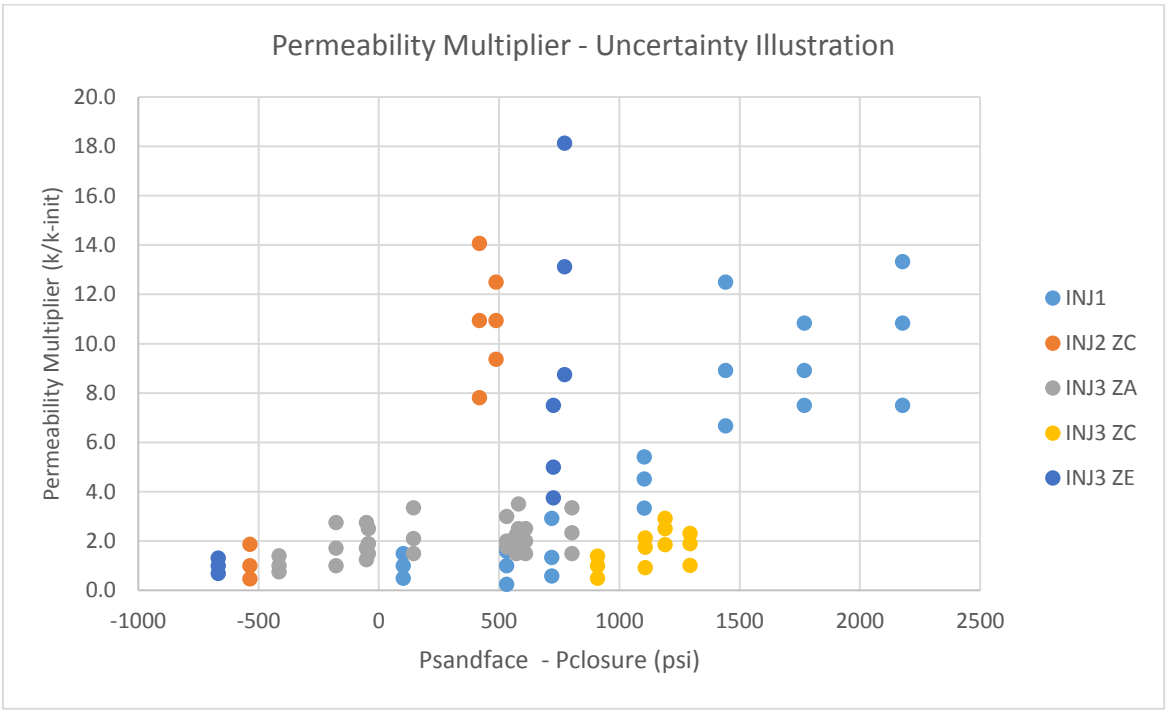

Figure 4.22: Illustration of overall scatter and uncertainty in the estimated permeabilities for the analyzed minifrac Step Rate Tests. The uncertainty is significant due to the short duration of the rate steps (Section 3.4), but the results still support the conclusions drawn based on Figure 4.20.

4.4 Time-Lapse Pressure Transient Analysis

Time-lapse Pressure Transient Analysis has been conducted on two Eldfisk B injectors (B-8 B & B-22) (Figure 8.1, Appendix A) to evaluate the impact of seawater injection on the Eldfisk reservoir. The analysis follows the procedure outlined in Section 3.3, with emphasis on determining conductivity and fracture development over time. Section 4.4.1 covers B-8 B, 4.4.2 B-22 and 4.4.3 the uncertainties.

4.4.1 B-8 B

The first injector to be analyzed is B-8 B. The injector was drilled as a replacement injector in January 2010, and injects into a previously flooded part of the Tor formation centrally on the B-structure (Figure 8.1, Appendix A). The structurally central location means that the B-8 B area was subject to substantial depletion during the primary production stage, with minimum pressure of 2300 psia predicted by the simulation model. The well encountered repressurized Tor formation with reservoir pressures between 4600 - 5000 psia, with porosities in the range 31%-35% (Appendix B: B-8 B CPI).

4.4.1.1 Injection History

B-8 B started injection into the Tor formation in March 2010. The well injected for 2.5 months before acid stimulation. The acid stimulation lead to a 3-fold increase in injection rates with maximum injection rates of 35 000 bbl/D. Figure 4.23 shows a summary of the B-8 B injection rate (orange) and pressure (yellow) history. Injection at 35 000 bbl/D was ended in January 2012 after a producer 400 ft from B-8 B collapsed in November 2011 (PROD1 Figure 8.1, Appendix A). After 6 months of reduced rates, the well was shut-in for 1.5 years to protect remaining producers. The well was put back on injection in June 2014, with significantly reduced rates to prevent tensile injection fracturing.

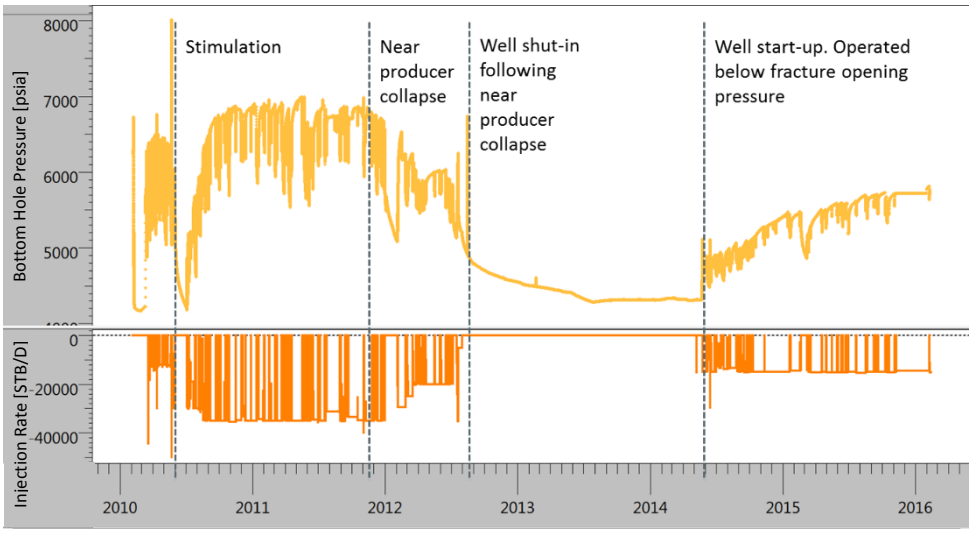

Figure 4.23: Illustration of B-8 B injection and Bottom Hole Pressure history. Injection rates are shown in orange and pressures in yellow. The well history is signified by an early period without acid stimulation, prior to a period of high injection rates ended by the collapse of a nearby producing well. The well was restarted in June 2014 following a 1.5-year shut-in after the collapse of the nearby producer, and injection rates are kept considerably lower to prevent undesired communication with nearby producers. Plot generated with Saphir, Kappa Engineering © 2016.

4.4.1.2 Time-Lapse Falloff Analysis

4.4.1.2.1 Impact of Acid Stimulation

Figure 4.24 shows a comparison of the pre- and post-acid stimulation injection falloff responses. The acid fracturing gives the expected decrease in reservoir skin due to near wellbore tensile fractures, which is seen from the decrease in pressure drop (ΔP, blue arrow). However, the stimulation also results in improved reservoir conductivity as seen from dropping semi-log derivatives (orange arrow). Warpinski and Teufel (1987) discussed the impact of natural fractures on induced fracture geometry, and showed that the resulting fracture patterns will be complex and also include expansion of natural fracture networks. The improved reservoir conductivity may therefore be linked to acidization of natural fracture networks. Omdal et al. (2008) showed that acid fracturing in high porosity chalk can create wormholes extending from the fracture (Section 2.8), and the conductivity increase could therefore also indicate development of fissures extending from the induced tensile fracture.

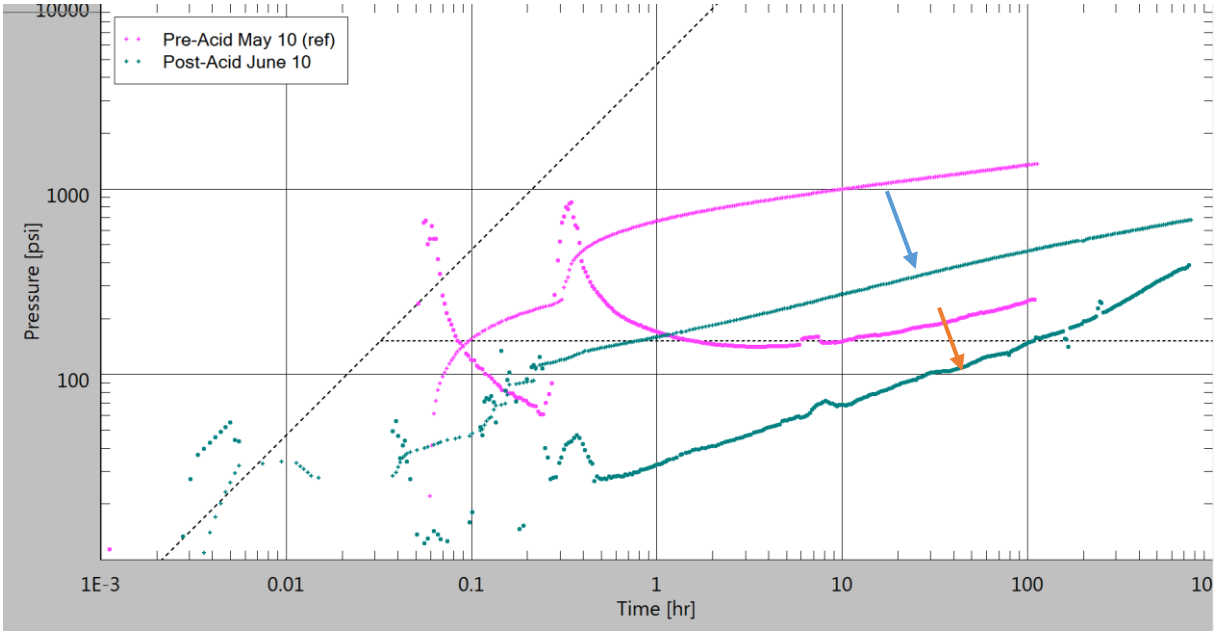

Figure 4.24: B-8 B injection falloff response pre-acid (purple) and post-acid (blue) stimulation. The acid stimulation gives the expected decrease in skin (blue arrow) due to induced tensile fractures. The post-acid response also indicates an improvement in the reservoir conductivity (orange arrow), which may be an indication of fissure development and enhancement of natural fracture networks. Plot generated with Saphir, Kappa Engineering © 2016.

4.4.1.2.2 Post-Stimulation Falloff Development

Figure 4.25 shows the falloff development over time after the acid stimulation. The derivatives indicate a significant increase in reservoir conductivity following the acid stimulation (orange arrow), and that the conductivity change is limited after 2011 where derivatives can be seen to stabilize. The reservoir skin is also seen to change (blue arrow), with distinctly lower skin after the restart of injection in 2014. Following Section 3.3.1, this can in part be linked to differences in injection rates, as higher rates will give more flow friction and therefore higher skin.

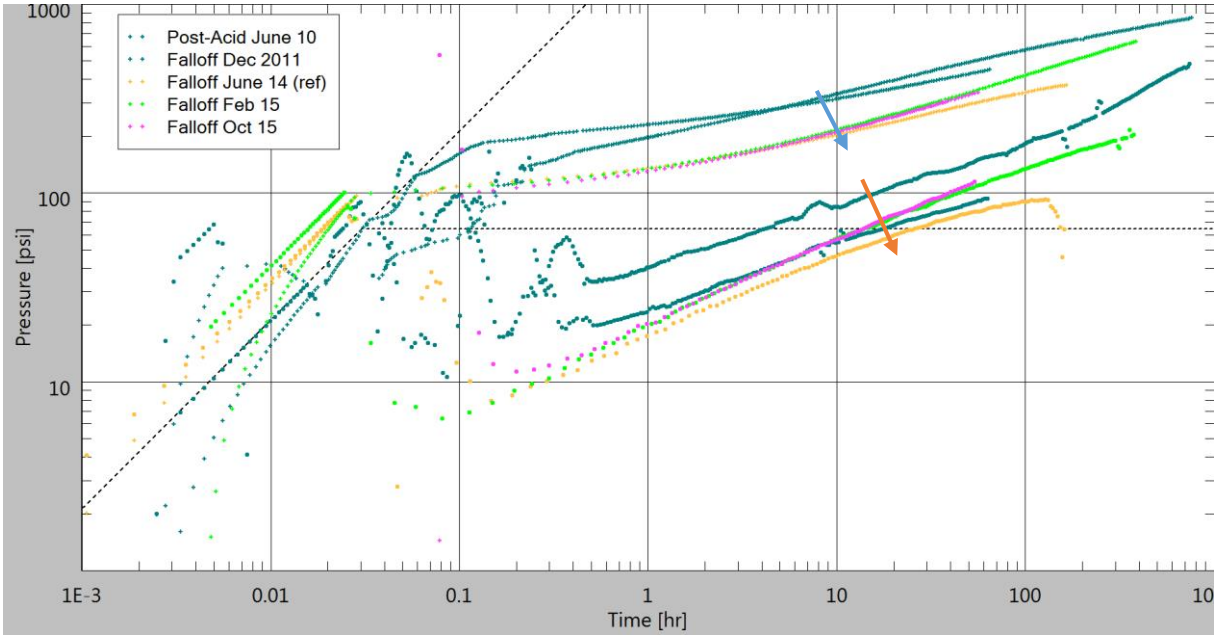

Figure 4.25: B-8 B injection falloff response over time. The response shows a significant change in conductivity after stimulation (orange arrow), with relatively constant conductivity after 2011. The falloffs also show a reduction in skin (blue arrow) after restart of injection in June 2014. The skin reduction is primarily linked to differences in wellbore friction due to reduced injection rates. Plot generated with Saphir, Kappa Engineering © 2016.

4.4.1.2.3 Falloff Analysis Results Including Wellbore Friction

The analysis including wellbore friction is a continuation of a study conducted by Anton Shchipanov (IRIS) in 2014. The study is included to allow for comparison with the results from the analysis without wellbore friction (Section 4.4.1.2.4). The results are from analytical wellbore and reservoir models and may be regarded as approximate values for reservoir properties.

Table 4.4 shows the results from the analysis with wellbore friction. Permeability increases from ~1 mD after the stimulation in June 2010, to ~4 mD by July 2012. The wellbore skin is also increased, from ~-4.7 post-acid stimulation to ~-1.2 in July 2012. The skin increase suggests near wellbore damage or perforation scaling, as the fracture models indicate no change in the effective fracture area. Some of the skin increase can also be coupled to a rate increase, and therefore an increase in wellbore friction below the gauge. The permeability is relatively constant after July 2012 only dropping from ~4 mD to ~3.5 mD by October 2015, suggesting that the observed permeability increase is caused by permanent changes in the reservoir. The skin is also constant from June 2014 to October 2015, only varying between ~-2.7 and ~-2.85, which indicates that there is no tensile fracture growth in the period after restart of injection in June 2014.

Table 4.4: Results from B-8 B time-lapse falloff analysis including wellbore friction. The analysis until 2012 was conducted by Anton Shchipanov (2014), while the "New Data" represents the continued analysis as part of this thesis work. Uncertain results are highlighted in green, and represent results where the match quality is poor. The analysis from June 2010 is highlighted as uncertain, but the permeability is definitely lower than the 3.0 mD in December 2011.

Parameter	Unit	May-10	Jun-10	Dec-11	Jul-12	Jun-14	Feb-15	Oct-15
All Models		Shchipanov				New Data		
Permeability	mD	0.6	1.0	3.0	4.0	4.0	3.5	3.5
Model with skin								
Well Skin	dim.less	-2.1	-4.7	-2.4	-1.2	-2.7	-2.85	-2.85
Models with Fractures								
Number of fractures		0	18	18	18	18	18	18
Fracture half-length (Xf)	ft	0	40	40	40	40	40	40
Fracture height (Hf)	ft	0	80	80	80	80	80	80
Fracture Area	ft^2	0	115200	115200	115200	115200	115200	115200
Injected Volume	MMBBL	1.3	1.7	17.5	20.9	21.3	24.5	27.6

4.4.1.2.4 Falloff Analysis Results Excluding Wellbore Friction

In the analysis without wellbore friction, all old data was reanalyzed to conform with the method outlined in Section 3.3.1. Fractures were assumed to extend beyond near wellbore damage, and well skin was therefore set to 0 in the fracture analysis.

The analysis results are shown in Table 4.5. A significant and gradual increase in permeability is observed from ~1.2 mD in June 2010 to ~4 mD by May 2011. From May 2011 the permeability remains relatively constant, only dropping to ~3.5 mD by October 2015. The results deviate slightly from those determined by Shchipanov (2014) in Table 4.4, indicating that permeability increase is seen until May 2011 and not July 2012 as indicated by Shchipanov. When the wellbore friction effects are removed, the reservoir skin shows relatively constant behavior after the acid stimulation, varying between ~-4.35 and ~-5.03 (Table 4.5). This suggests no significant growth of tensile injection fractures, and maintained opening of acid induced fractures. This is supported by the confident results in Table 4.5 which show relatively constant fracture area, only varying between ~172 800 ft^2 and ~230 400 ft^2.

Uncertain analysis results in Table 4.4 and Table 4.5 are highlighted in green. An analysis is classified as uncertain if the falloff behavior cannot be matched with the chosen wellbore model. The values for these falloffs in Table 4.4 and Table 4.5, represent the reservoir and well properties from a best possible match. As an illustration of the uncertainty range, different matched models for the falloff in September 2010 shown in Table 4.5, give permeabilities ranging between ~0.75 mD to ~1.25 mD. This still supports the conclusion drawn based on the ~1 mD value in Table 4.5, that the falloff indicates a lower permeability than the ~2 mD in August 2010 and ~2.5 mD in October 2010. The uncertain results may therefore indicate trends, but cannot be relied upon for absolute values.

Table 4.5: Results from B-8 B time-lapse falloff analysis without wellbore friction (ISIP). The results deviate slightly from those seen in Table 4.4, as the data analyzed by Anton Shchipanov (2014) were reanalyzed. Uncertain results are highlighted in green, and represent results where the match quality is poor. The results from September 2010 are especially uncertain due to poor match quality, and the permeability is estimated to vary between ~0.75 mD and ~1.25 mD.

Parameter	Unit	May-10	Jun-10	Aug-10	Sep-10	Oct-10	Jan-11	Mar-11	May-11	Dec-11	Jul-12	Jun-14	Feb-15	Oct-15
All Models		Pre-Stim	New Analysis											
Permeability	mD	0.6	1.2	2.0	1.0	2.5	2.5	3.5	4.0	4.0	4.0	4.0	3.5	3.5
Model with skin (no ISIP)														
Well Skin	dim.less	-3.07	-4.8	-4.35	-4.8	-4.35	-5.03	-4.5	-4.35	-4.5	-4.27	-4.8	-4.35	-4.35
Models with Fractures (0 well skin)														
Number of fractures		18	18	18	18	18	18	18	18	18	18	18	18	18
Fracture half-length (Xf)	ft	20	85	55	100	60	105	70	70	65	60	80	70	60
Fracture height (Hf)	ft	80	80	80	80	80	80	80	80	80	80	80	80	80
Fracture Area	$X10^3$ ft²	57.6	245.0	158.4	288.0	172.8	302.4	201.6	201.6	187.2	172.8	230.4	201.6	172.8
Injected Volume	MMBBL	1.3	1.7	2.1	3.1	5.0	7.5	9.8	11.5	17.5	20.9	21.3	24.5	27.6

Figure 4.26 shows a plot of the reservoir permeability versus the injected water volume. Permeability remains constant after approximately 12 MMBBL of injected water. The early permeability increase after the stimulation follows a close to linear trend. As injected water volume is coupled to an increase in reservoir pressure, this may suggest a connection between near wellbore reservoir pressure and reservoir conductivity. Alternatively, the linear relation indicates that the permeability increase is a function of the position of the waterfront.

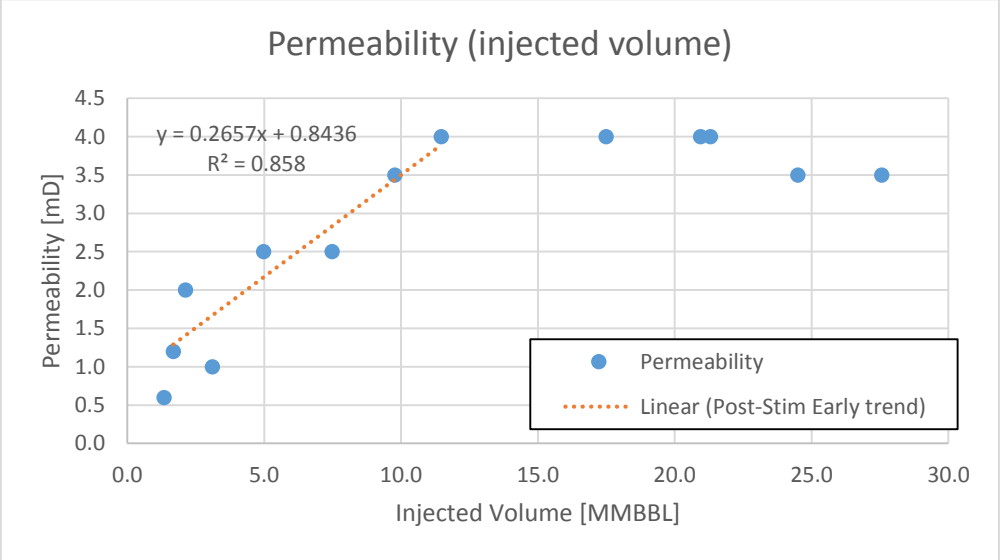

Figure 4.26: Plot of permeability as a function of injected volume. The early permeability increase shows a close to linear development, followed by a constant conductivity response after ~12 MMBBL injected. The plot suggests that pressure may be a key controller of reservoir permeability, as reservoir pressure will have increased substantially in the near wellbore area during the first injection period. Alternatively, the plot indicates that the observed permeability increase is a function of the position of the waterfront.

4.4.1.3 Dynamic Reservoir Response

Shchipanov et al. (2014) pointed out that to properly understand reservoir behavior it is important to analyze flowing periods in addition to falloffs. Behavioral differences would indicate dynamic reservoir behavior, with reservoir properties dependent on flow rates and injection pressures. Figure 4.27 shows consecutive injection and falloff periods in B-8 B. Both periods are matched by the same reservoir model, which indicates that results from falloff analysis are representative for injection performance. The only observable difference is injector-producer interference seen in the injection response, shown by the dropping derivative indicated by the blue arrow in Figure 4.27.

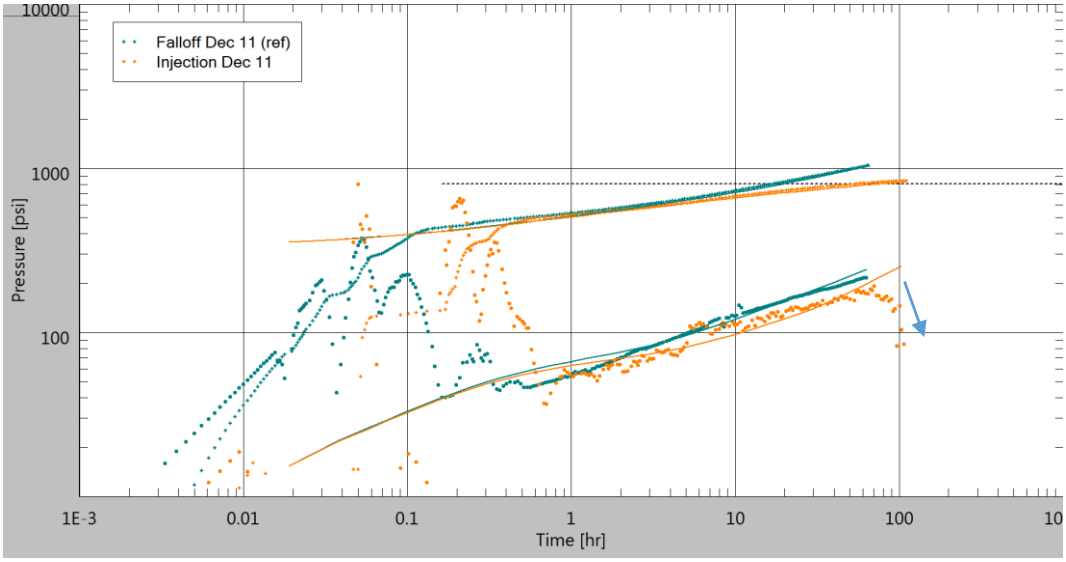

Figure 4.27: Illustration of consecutive falloff and injection flow response comparison for B-8 B. Both periods are matched by the exact same model, indicating no dynamic reservoir behavior in B-8 B. Analysis from falloff periods should therefore be representative for flowing periods. The dropping derivative in the injection response (blue arrow) indicates communication with a producer. Early derivative fluctuations between 0.02 and 0.8 hrs are due to rate variations during shut-in and startup, and are not reservoir effects. Plot generated with Saphir, Kappa Engineering © 2016.

The results are different from the dynamic behavior seen in PTA of minifrac Step Rate Tests (Section 4.3.2), and may indicate lack of tensile injection fracturing. The results could therefore suggest that the observed permeability increase seen in Section 4.4.1.2, is related to another mechanism than induced tensile injection fractures. However, it must also be stated that minifrac effects can only indicate changes near the wellbore and the fracture, due to relatively small pumped volumes.

4.4.1.4 Fracture and Closure Pressure Development

Following the method outlined in Section 3.5.2, the reservoir pressure development was determined for B-8 B as seen in Figure 4.28. The reservoir pressure is an estimate of the near wellbore reservoir pressure, which will control the formation fracture pressure. The reservoir pressure indicates a significant increase in pressure after the acid stimulation, from approximately 4500 psia in June 2010 to approximately 5700 psia by May 2011. Following the derived closure pressure relation in Section 4.1.1, this will result in an increase in the formation closure pressure and fracture initiation pressure.

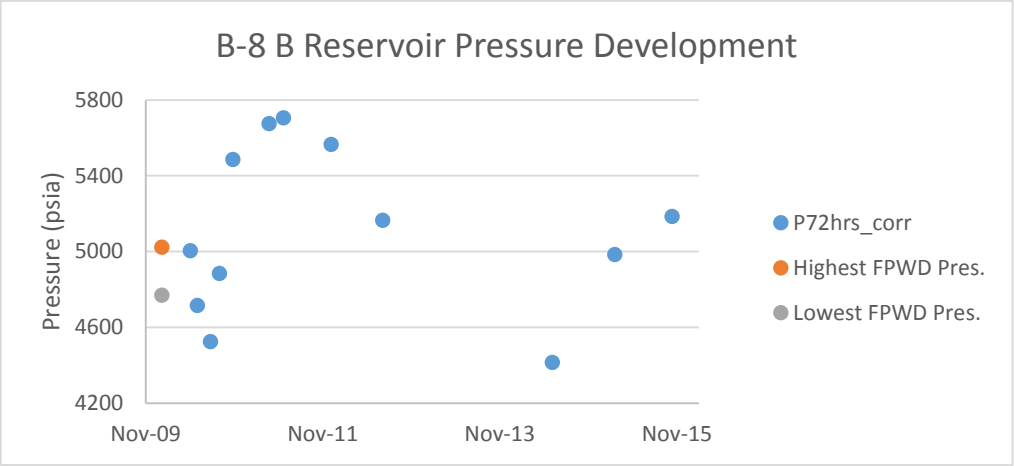

Figure 4.28: Analyzed reservoir pressure development for B-8 B. The reservoir pressure development is an estimate of the near wellbore reservoir pressure, and not the average reservoir pressure in the drainage area.

Figure 4.29 shows a plot of the Eldfisk model predicted fracture closure and fracture initiation pressure based on the reservoir pressure in Figure 4.28. The additional 600 psi fracture initiation pressure is assumed to be representative for the fracture reopening pressure (Sections 2.2.1.4 and 4.4.3.3). The pressures are compared against sandface corrected Bottom Hole Pressure (BHP), which is the gauge BHP with friction removed and an added hydrostatic correction (Section 4.2.1).

The results clearly show that the fracture initiation pressure has not been exceeded, and tensile injection fractures are not the likely cause of the reservoir permeability increase. Closure pressure was exceeded during the early pre-acid stimulation injection period, which could have resulted in some conductivity increase from natural fracture expansion, explaining the good match with a fractured model in May 2010 in Table 4.5. The results make shear failure at pressure below fracture closure the likely explanation for B-8 B permeability increase.

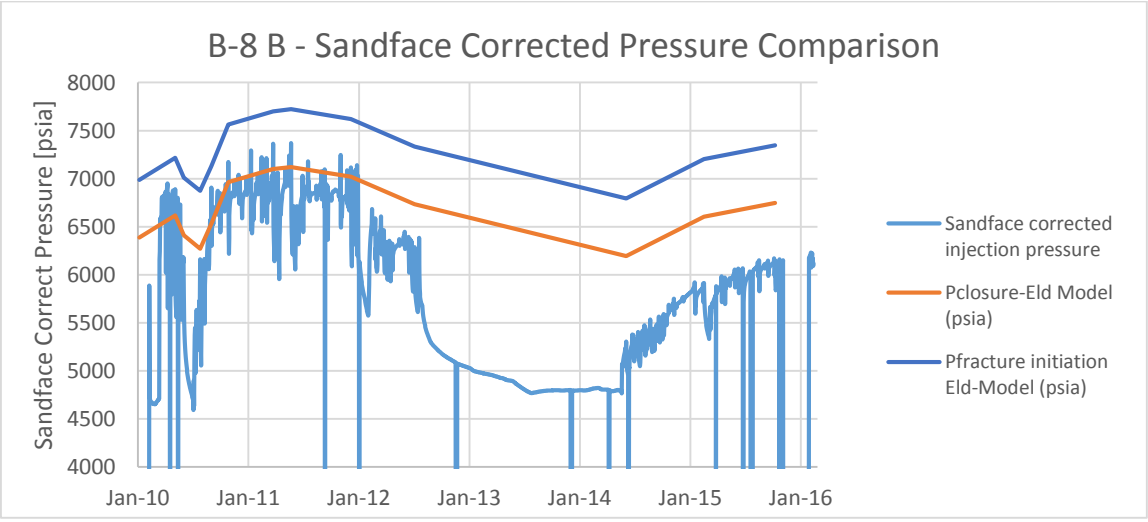

Figure 4.29: Plot of sandface corrected bottom hole pressure vs closure and fracture pressure development for B-8 B. The pressures indicate that tensile fractures have not been initiated in B-8 B, but the fracture closure pressure was clearly exceeded during the early unstimulated injection period (until June 2010).

A pressure controlled permeability model suggests, as seen in Figure 4.29, that the permeability increase may be pressure controlled, but the maintenance appears to be nearly independent of pressure. The chemical interaction between seawater and opened fracture surfaces may lead to alterations which prevent fracture closure (Section 2.6). In shear failure controlled fracture systems, permeability maintenance is also likely due to the complex displacement of the fracture planes.

4.4.1.5 Producer Interaction – Evidence of Fault System

As described in Section 4.4.1.1, B-8 B was identified as the cause of wellbore collapse in a nearby producer designated as PROD1 in Figure 8.1 (Appendix A). The producer collapsed after a massive water breakthrough, which was suggested to be caused by tensile injection fracturing in B-8 B. The well collapsed on Nov 10th 2011, and as seen from the results in May, December 2011 and July 2012 in Table 4.5, there is no observable change in B-8 B behavior in this period.

Figure 4.30 shows B-8 B falloff behavior from July 5th 2011 to March 16th 2012, just before and after the well collapse on Nov 10th 2011. The derivatives and pressures in the nine shown falloffs are consistent and show no significant change. The falloff responses do therefore not indicate any change in well or reservoir behavior.

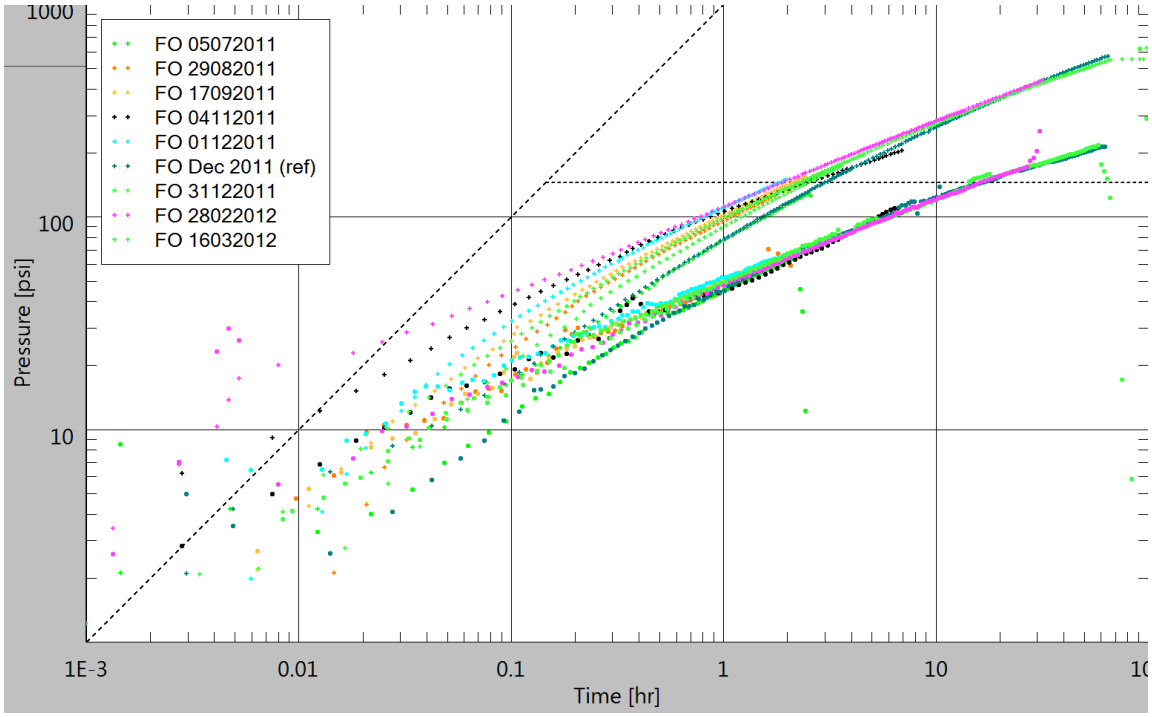

Figure 4.30: Detailed B-8 B injection falloffs just before and after the PROD1 collapse on Nov 10th 2011. The start date of the falloff is shown in the figure legend in the top left. No change in B-8 B reservoir behavior can be observed from the falloffs, as both pressures and derivatives are consistent. Plot generated with Saphir, Kappa Engineering © 2016.

Figure 4.31 shows the injection periods from April 14th to December 29th 2011, just before and after the well collapse on Nov 10th. The period start date is shown in the legend in Figure 4.31, with the time since start of injection on the time axis. The results show dynamic behavior which deviates from the long term observations in Section 4.4.1.3. In 5-6 months, from April to November, leading up to the well collapse, the injection responses show a progressive drop in derivatives (orange arrow) and pressures (blue arrow). This indicates an increase in reservoir conductivity (kh) and a reduction in the reservoir skin. The derivatives and the pressures are at their lowest in the injection period starting Nov 5th, indicating that maximum increase in permeability and reduction in skin is seen just prior to the well collapse on Nov 10th. This increase disappears as soon as the nearby producer is lost due to the wellbore collapse, as seen from the reestablished derivative and pressures in the injection period starting December 29th. B-8 B and PROD1 are connected by a fault (black arrow Figure 8.1, Appendix A), which is not perforated to avoid early breakthrough. The observed changes may therefore be a result of the B-8 B waterfront reaching the fault and then channeling towards PROD1. As long as PROD1 provides a drawdown on the fault, the fault will dominate the flow response of B-8 B. Once the producer is lost, the fault will no longer strongly impact the B-8 B response.

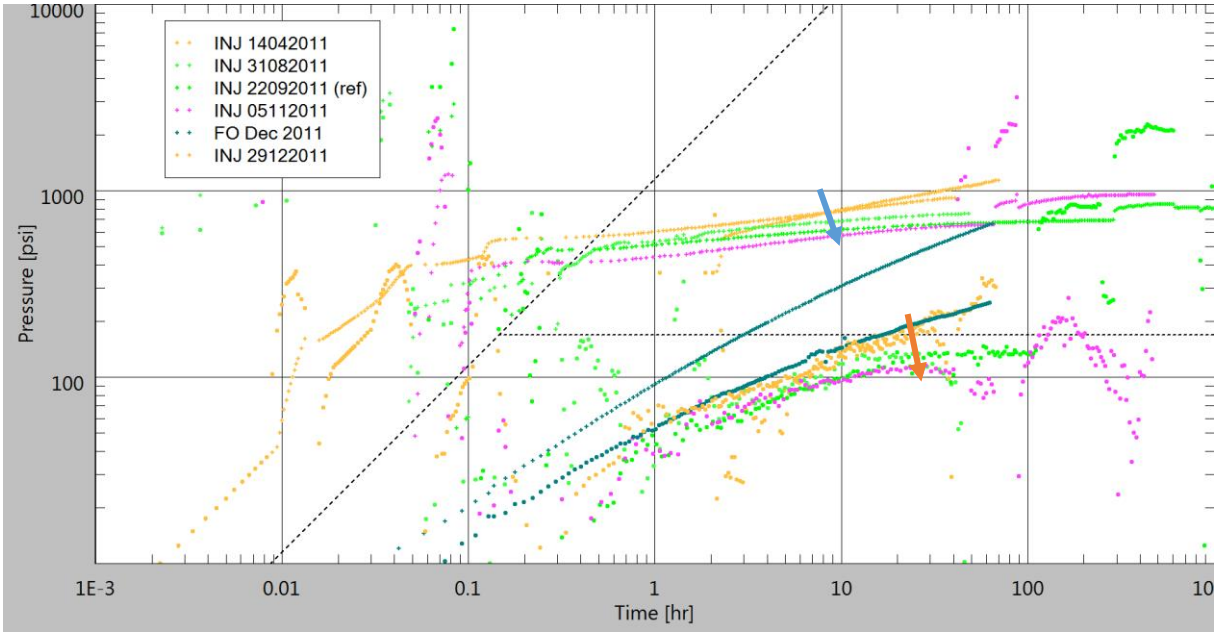

Figure 4.31: Plot of B-8 B Injection responses just before and after the PROD1 collapse. The start of the injection period is shown in the legend in the top left, the time axis plots the duration since the start of the period. The injection shows a significant increase in reservoir conductivity (orange arrow) and a decrease in skin (blue arrow) just prior to the producer collapse. The change is not observed after the well collapse. The effects are interpreted as B-8 B connecting to a nearby fault system which channels water towards PROD1 due to the drawdown at the producing well. Once the producer is lost the fault no longer strongly impacts the B-8 B response. Plot generated with Saphir, Kappa Engineering © 2016.

The conductivity increase makes a single tensile fracture from B-8 B which closes PROD1 is lost, an unlikely explanation (Section 4.3.2.3.2). This would also contradict the findings in Section 4.4.1.4 which showed that the fracture initiation pressure was not exceeded.

4.4.2 B-22

The second water injection well to be analyzed is B-22. B-22 was drilled as a Tor replacement injector on the eastern flank of the Eldfisk B structure (Figure 8.1, Appendix A). The well encountered injection water flooded reservoir, repressurized to 4150 – 4450 psia from a minimum of 3600 psia predicted by the reservoir model. The reservoir properties are good for a flank well, with porosities between 31%-34% (Appendix C: B-22 CPI).

4.4.2.1 Injection History

B-22 injected very limited volumes prior to the acid stimulation in May 2010 (Figure 4.32). The well has been on continuous injection since June 2010, with shut downs in 2013 and 2015. Injection rates have declined from initial 35 000 bbl/D to 17 000 bbl/D, which is primarily believed to be due to reservoir pressure increase in response to the water injection.

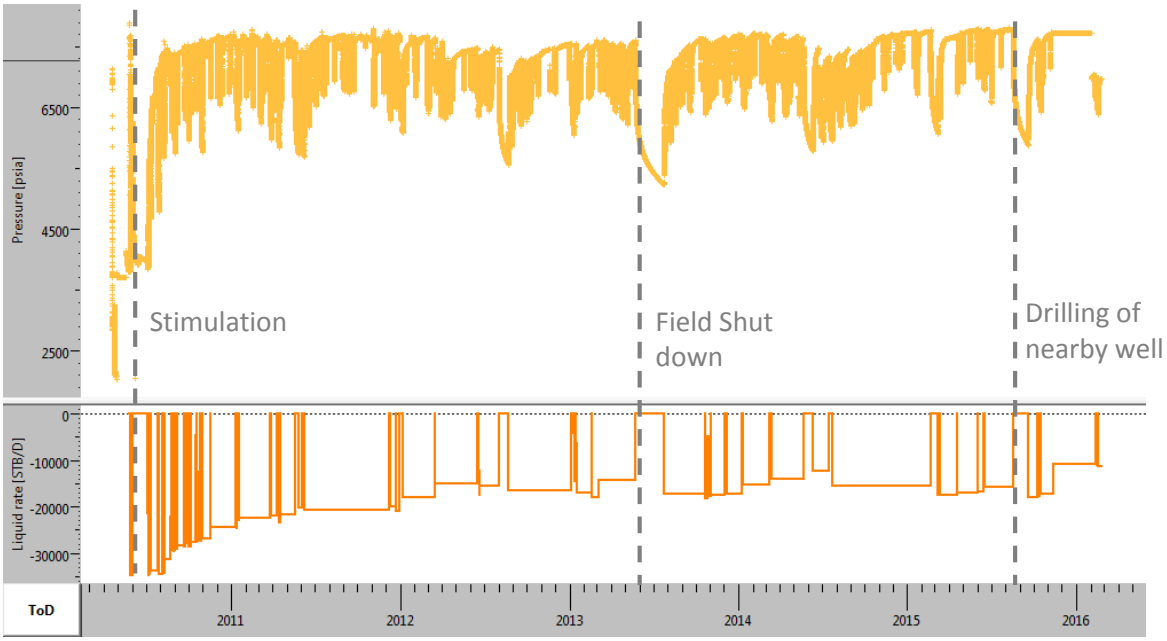

Figure 4.32: B-22 Injection history. Plot of BHP (yellow) and injection rate (orange) vs time. Limited volumes were injected prior to stimulation in May 2010. The well has been on continuous injection since June 2010, apart from the field shut down in 2013 and shut-in due to drilling of nearby well in 2015. Plot generated with Saphir, Kappa Engineering © 2016.

4.4.2.2 Time-Lapse Falloff Analysis

4.4.2.2.1 Post-Stimulation Falloff Development

Figure 4.33 shows a time-lapse of the B-22 falloff responses. The data suggest very limited change in reservoir properties. There is an observable decrease in conductivity (permeability) seen from increasing derivatives from June 2010 to June 2012 (orange arrow Figure 4.33), after which the reservoir response remains constant. There is no observable significant change in skin, as seen from the stable pressures in Figure 4.33, suggesting no tensile fracture growth.

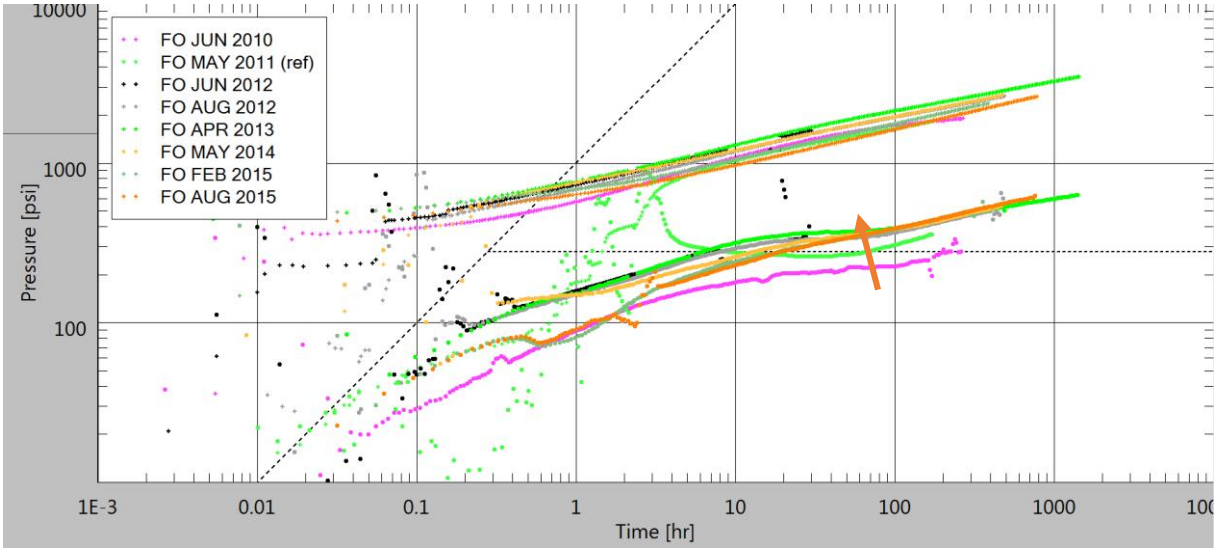

Figure 4.33: B-22 Falloff development. Falloff start dates are shown in the legend. The falloff response may indicate a decrease in reservoir conductivity (orange arrow) and very limited change in reservoir skin. Plot generated with Saphir, Kappa Engineering © 2016.

4.4.2.2.2 Falloff Analysis Including Wellbore Friction

In accordance with the analysis conducted for B-8 B (Section 4.4.1), falloff analysis for B-22 was also conducted including wellbore friction. The results of the analysis are shown in Table 4.6. Both B-8 B and B-22 show porosities between 31%-35%, but the observed permeability in B-22 (~0.6 mD) is significantly lower than B-8 B (max ~4 mD, Table 4.5), indicating less natural fractures due to the flank location of the well. The initial ~1 mD permeability in B-8 B after stimulation (Table 4.4), is however comparable to the initial ~0.6 mD in B-22, possibly indicating that the difference between the wells is caused by the water injection. The permeability in B-22 (Table 4.6) is on a decreasing trend with time, decreasing from ~0.6 mD in June 2010 to ~0.35 mD by August 2015. The skin and fracture area remain relatively constant in the same period, varying between ~-2.55 to ~-3.5 and ~52 800 ft^2 and ~86 400 ft^2, respectively. The slight reduction in skin may be due to reduced wellbore friction as injection rates decrease (Section 3.3.1). The fracture model results are very uncertain due to a poor model match. The assumption of full height fractures leads to unrealistic fracture half-lengths, but analysis was conducted which demonstrated that the calculated fracture area is consistent for varying fracture geometry. The relatively constant fracture area therefore indicates no significant tensile fracture growth.

Table 4.6: Analysis results for B-22 falloff analysis including wellbore friction. The results show very low reservoir permeability, and a decreasing reservoir permeability trend. Uncertain results are highlighted in green, and represent results where the match quality is poor.

Parameter	Unit	Jun-10	Jun-11	Aug-12	Apr-13	May-14	Aug-15
All Models							
Permeability	mD	0.6	0.55	0.425	0.4	0.35	0.35
Model with skin							
Well Skin	dim.less	-3.5	-2.55	-2.8	-2.7	-3.25	-3.5
Models with Fractures							
Skin (Fracture)	dim.less	20	25	25	25	25	15
Number of fractures		12	12	12	12	12	12
Fracture half-length (Xf)	ft	15	11	11	11	18	18
Fracture height (Hf)	ft	200	200	200	200	200	200
Fracture Area	ft^2	72000	52800	52800	52800	86400	86400
Injected Volume	MMBBL	1.2	8.9	16.5	20.7	25.3	31.7

4.4.2.2.3 Falloff Analysis Excluding Wellbore Friction

The results of the falloff analysis excluding wellbore friction have high certainty due to good model match. The results are seen in Table 4.7, and confirm a decreasing reservoir permeability trend from June 2010 (~0.5 mD) to August 2012 (~0.3 mD), as indicated in Figure 4.33. From August 2012 to August 2015 the permeability is relatively constant, varying between ~0.3 - ~0.35 mD. The skin shows small variations (~-3.7 - ~-4.3), and the matched fracture area (~62 400 ft^2 – ~139 200 ft^2) shows some variation, but does not indicate substantial fracture growth post-acid stimulation.

The overall conclusion may be drawn that B-22 reservoir response is relatively stable throughout the injection period. Section 4.4.3 will discuss how reservoir cooling together with the model assumption of constant viscosity, may be the cause of the decreasing permeability trend.

Table 4.7: Analysis results for B-22 falloff analysis excluding wellbore friction. Uncertain results are highlighted in green, and represent results where the match quality is poor. The results have low uncertainty due to good model match. As wellbore skin is excluded, the fracture model assumes 0 fracture skin.

Parameter	Unit	Jun-10	Jun-11	Aug-12	Apr-13	May-14	Aug-15
All Models							
Permeability	mD	0.5	0.45	0.3	0.35	0.3	0.3
Model with skin (no ISIP)							
Well Skin	dim.less	-4.2	-3.75	-4.1	-3.7	-4.2	-4.3
Models with Fractures (0 well skin)							
Skin (Fracture)	dim.less	0	0	0	0	0	0
Number of fractures		12	12	12	12	12	12
Fracture half-length (Xf)	ft	27	15	23	13	25	29
Fracture height (Hf)	ft	200	200	200	200	200	200
Fracture Area	ft^2	129600	72000	110400	62400	120000	139200
Injected Volume	MMBBL	1.2	8.9	16.5	20.7	25.3	31.7

4.4.2.3 Dynamic Reservoir Response

In general, the flowing period (injection) dataset in B-22 is poor. The derivatives and pressure drops match those observed in the falloffs, but the injection periods are disturbed by rate fluctuations and noise (yellow arrow Figure 4.34). Figure 4.34 shows consecutive falloff and injection periods that are matched by the same radial composite model. The radial composite model is required to match the mobility contrast seen across the waterfront in the injection period (blue arrow). Falloff responses do not show the waterfront (Figure 4.33), and Figure 4.34 shows that the derivatives and therefore the determined properties are representative for the waterflooded part of the reservoir. The mobility contrast across the waterfront is primarily due to differences in relative permeability, and indicates that the determined permeability in Table 4.6 and Table 4.7 is the effective permeability to water. The sharp waterfront in Figure 4.34 (blue arrow) indicates no significant water channeling along fault or fracture planes, which supports the conclusion of no tensile fracture growth.

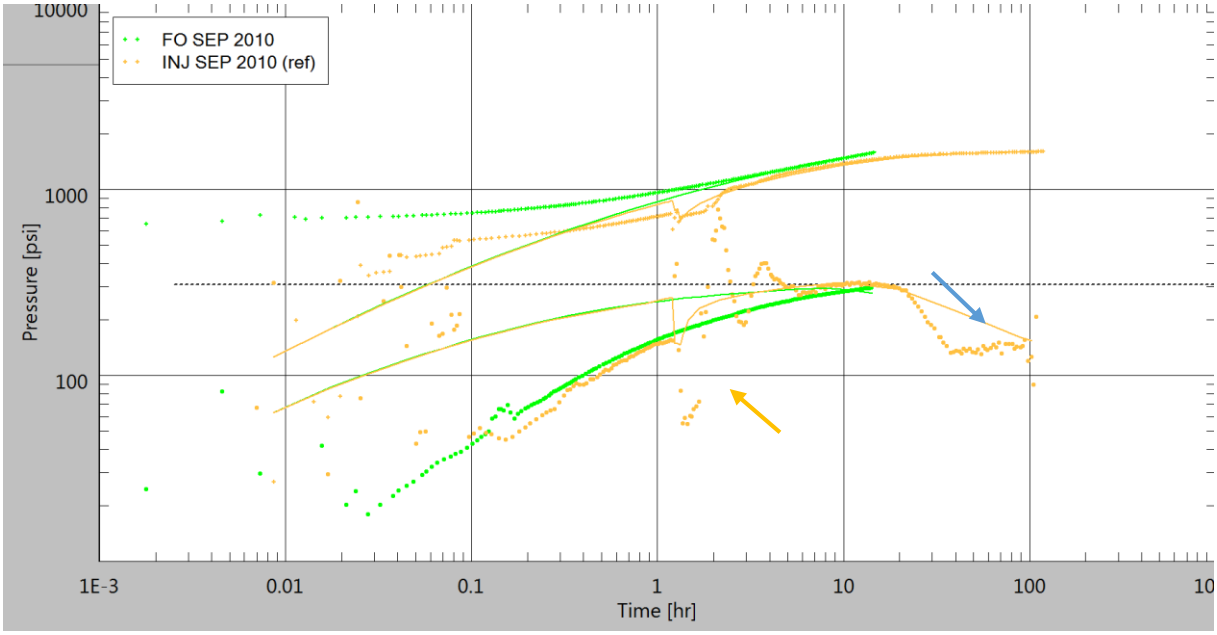

Figure 4.34: Log-log plot of consecutive B-22 injection and falloff responses. The injection response shows noise due to rate variations (fluctuating derivatives, yellow arrow), but the derivatives can clearly be seen to match the falloff. The transition into a second radial flow regime (blue arrow) shows the waterfront with a transition into higher relative permeability oil across the front. Plot generated with Saphir, Kappa Engineering © 2016.

4.4.2.4 Fracture and Closure Pressure Development

Following the same procedure as for B-8 B (Section 3.5.2), the reservoir pressure in the near well area around B-22 was determined. Figure 4.35 shows the reservoir pressure development. As expected, the reservoir pressure increases substantially in response to the injection, from ~4200 psia in February 2010 to ~6800 psia by August 2015. This is a result of the low permeability in the area which gives large pressure gradients in the reservoir.

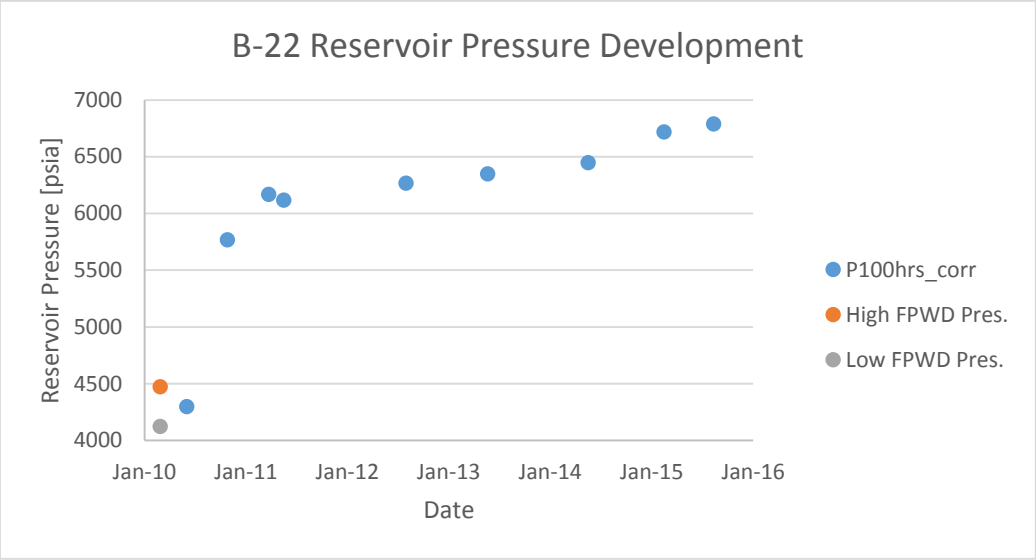

Figure 4.35: Reservoir pressure development in near well area around B-22. The pressure increases substantially in response to the injection due to the low reservoir permeability in the area.

Figure 4.36 compares the predicted closure and fracture initiation pressure from the Eldfisk model, to the sandface corrected injection pressure. The data supports the claim of no tensile fracturing as all injection pressures are below the fracture initiation pressure. According to the Eldfisk model, the closure stress should have been exceeded, but no permeability increase is observed. This suggests a different closure stress on the flanks of the Eldfisk structure, or very limited natural fracture networks to contact. In Section 5.1, stress arching will be discussed as a possible explanation for the observed B-22 trends, as arching would lead to increased closure stress on the flanks of the structure.

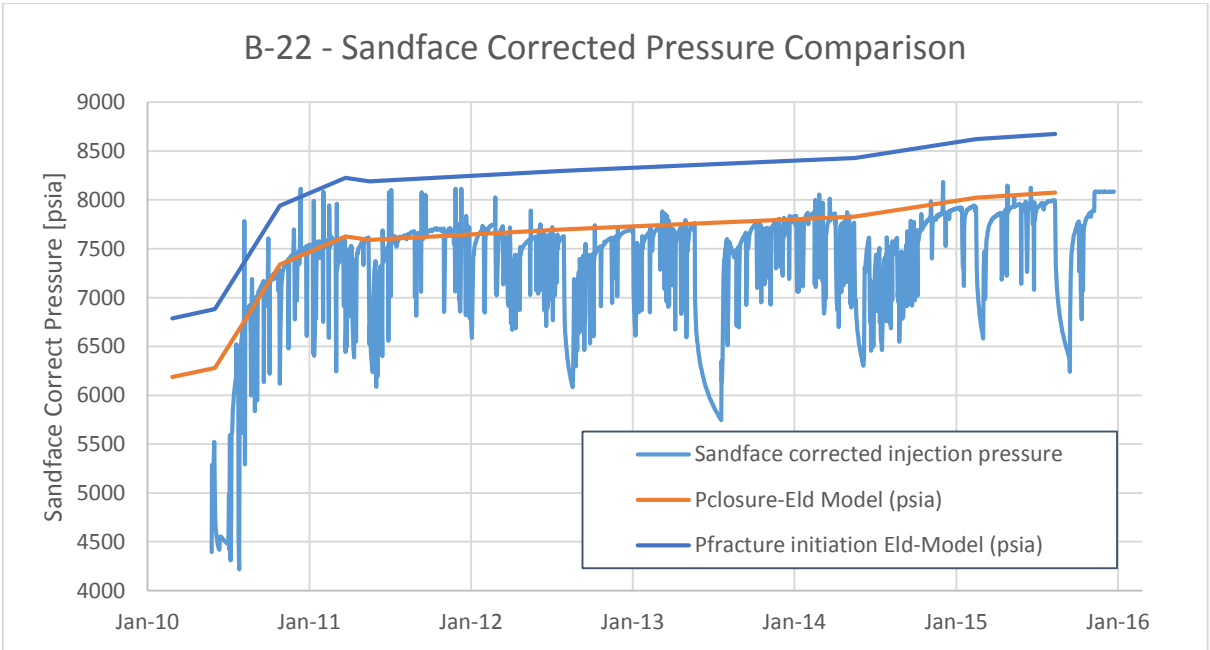

Figure 4.36: Predicted closure and fracture initiation pressure from the Eldfisk model, compared to the sandface corrected B-22 injection pressure. According to the Eldfisk closure model the injection pressure has exceeded the closure stress of the formation.

4.4.3 Uncertainty Evaluation

The results from the analysis in Sections 4.4.1 and 4.4.2 are based on PTA modelling, and will as a result be subject to significant uncertainty. In addition, rate variations and wellbore uncertainties attribute to the overall analysis uncertainty. Table 4.8 outlines the minor uncertainties and the mitigative measures, while the reservoir pressure, viscosity and fracture reopening uncertainties are discussed separately.

Table 4.8: Table highlighting the minor uncertainties in the time-lapse PTA in Section 4.4.

Uncertainty	Implication / Mitigative Measure
Effective wellbore length	The primary uncertainty in conductivity evaluation with horizontal wellbore model. Uncertainty proven to be small with Injection Logging Tools (ILT) in B-8 B and 4D seismic in B-22.
Reservoir thickness	The reservoir thickness is chosen based on vertical wells drilled close to the horizontal injectors. With no observed late radial flow, the reservoir thickness will have a negligible impact on the determined reservoir permeability and skin.
Relative permeability	Relative permeability effects are neglected as both wells were initially waterflooded. B-22 showed that the analysis was representative for the effective permeability to water (Section 4.4.2.3).
Horizontal wellbore model	Horizontal fractured wellbore models are hard to match accurately. To ensure that model results correctly represents reservoir changes, B-8 B analysis focused on matching linear flow behavior, while B-22 analysis focused on matching early radial flow. Relative changes in reservoir permeability and skin can therefore be regarded as reliable.
Early radial flow match	Due to low permeability in B-22, the early radial flow regime was consistently best established. Matching this regime with k_v/k_h = 1 implies that the actual matched permeability is $\sqrt{k_v \cdot k_h}$. The relative changes in permeability are still representative assuming both vertical and horizontal permeability change.
Determining Instantaneous Shut-In Pressure (ISIP)	ISIP pick for analysis without wellbore friction is subjective and will influence the calculated fracture area and skin. Results without wellbore friction are consistent, indicating consistency in the pick and therefore reliable results.

4.4.3.1 Reservoir Pressure Uncertainty

A clear uncertainty is the determined reservoir pressures. Under ideal conditions with infinite falloff length and no producers, the reservoir pressure could be determined unequivocally. However, the objective of the analysis is not to determine the average reservoir pressure in the system, but the average reservoir pressure around the well. This is based on the assumption that near wellbore reservoir pressure dictates the fracture strength of the formation.

The reservoir pressure has been determined with a constant pressure adjustment to match the FPWD reservoir pressures (Figure 4.28 and Figure 4.35). A constant pressure correction will be a simplification, as the pressure drop will be a function of the injection rate prior to the falloff, with larger pressure drop for higher rates. For B-8 B the correction is made based on an injection rate of 10 000 bbl/D, which should result in an overprediction of the reservoir pressure when the well injects at 35 000 bbl/D. However, conductivity is also increased in B-8 B which will lead to an underprediction of the reservoir pressure. The relative change in rate and conductivity during the critical initial period where the conductivity changes, is comparable (both ~3-4 times) and the estimated reservoir pressure should be representable.

B-22 is corrected with a constant pressure adjustment to match the initial reservoir pressure. The falloff follows a high rate Step Rate Test. No rate correction is incorporated, which may give an underestimation of the reservoir pressure as the injection rate decreases. The observed decrease in conductivity may lead to an overestimation of the reservoir pressure, and the applied pressure correction should therefore have a limited error.

It must, however, be stated that reservoir pressure from falloff analysis will still be uncertain, as the actual reservoir pressure representable for the formation fracture strength is not known.

4.4.3.2 Reservoir Fluid Viscosity Uncertainty

The PTA is conducted with assumed constant water viscosity of 0.3 cP, which corresponds to the viscosity of water at ~100 °C (Beal 1946). Section 2.2.1.6 discussed the impact of thermal effects on the fracture initiation pressures, and indicated that the thermal front moved at a speed 30-50% of the waterfront. Due to the low temperature of the injection water, same length falloffs will over time represent progressively cooler formations. Beal (1946) showed that a decrease in reservoir temperature by 40 °C from 100 °C to 60 °C, will increase the viscosity of water by an approximate factor of 2. The actual parameter that is matched in the PTA is a function of both the conductivity and the viscosity:

$$Matched\ Parameter = \frac{k \cdot h}{\mu} \quad (4.2)$$

As the analysis assumes a constant low viscosity, it is apparent that with the same matched parameter, an increase in viscosity would mean a higher reservoir conductivity. This explains the decreasing conductivity trend seen in B-22 (Section 4.4.2.2.3) as an actual indication of reservoir cooling and water viscosity increase. For B-8 B the same effect will enhance the observed increase in reservoir conductivity.

4.4.3.3 Fracture Reopening Pressure Uncertainty

As stated in Sections 4.2.2 and 4.4.1.4, the fracture initiation pressure shown in Figure 4.29 (Section 4.4.1.4) and Figure 4.36 (Section 4.4.2.4) should be a fracture reopening pressure. As discussed in Section 2.2.1.4, in a fractured wellbore the propagation of tensile fractures will be controlled by the pressure required to reopen the existing fractures. The fracture initiation pressure data in Section 4.2 will deviate from the fracture reopening pressure if the reservoir has considerable tensile strength (Section 2.2.1.4). As the fracture initiation pressures are determined from perforated zones, the Lost Circulation Material used during drilling can be assumed to not impact the dataset. Rod and Jørgensen (2005) suggested that naturally fractured chalk would exhibit a tensile strength close to 0, as tensile fractures would be initiated along natural fracture planes. Under these assumptions the fracture initiation pressure in Figure 4.29 and Figure 4.35, will be representative for the fracture reopening pressure.

Havmøller et al. (1996) showed through a review of rock mechanical data, that reservoir cores between 30-35 % porosity gave tensile strength measurements in the range of 75 – 400 psi. If the core measured values are representative for reservoir behavior, the fracture reopening pressure in B-8 B and B-22 would still exceed the closure stress by at least 200 psi, as the fracturing differential pressure was 600 psi (Section 4.2.2). Under these assumptions, as seen from Figure 4.29 (Section 4.4.1.4), B-8 B could potentially have induced tensile fractures during the early unstimulated injection period. All other conclusions in Sections 4.4.1.4 and 4.4.2.4 on B-8 B and B-22 stress would remain the same. How applicable core measured values are for reservoir behavior, is also uncertain.

5 Discussion

5.1 Stress Arching – Closure Stress Model

Stress arching is known to increase the overburden stress on the flanks of subsiding reservoirs, while reducing the overburden stress towards the crest. In the Eldfisk and Ekofisk reservoirs, subsidence is ongoing despite water injection and repressurization of the reservoirs. The result is continued stress arching despite pressure maintenance in the reservoir.

Personal communication with Edvard Omdal (2016a) (Reservoir Engineer, ConocoPhillips) indicated that overburden modelling over the Ekofisk Field has shown stress arching magnitudes of ~1000 psi. Estimates of the impact of stress arching may therefore be made assuming 500 psi overburden stress increase on the flanks and -500 psi overburden relief on the crest of the Eldfisk structure. These corrections should in future studies be confirmed with an Eldfisk overburden model. According to Section 2.4.2, assuming linear elasticity, stress arching will impact the closure stress as described in Equation 2.21. The closure stress determined from the Eldfisk model can therefore be corrected for stress arching with a factor corresponding to:

$$\Delta\sigma_{h,Arching} = \frac{\nu}{1-\nu}\Delta\sigma_v = \left(1 - A_{pe}\right) \cdot \Delta\sigma_v \tag{5.1}$$

With the Eldfisk model closure slope (A_{pe}) of 0.72 determined in Section 4.1.1, this gives a closure stress correction of ± 140 psi. Teufel and Rhett (1991) showed from closure stress analysis on the Ekofisk Field, that closure stress on the flanks of the Ekofisk structure was ~900 psi higher than the crest. The 280 psi magnitude stress difference estimated is therefore conservative, and appears to be more in line with the local variation seen in the closure trend in Sections 4.1.1 and 4.1.3.4.

Figure 5.1 compares the stress arching corrected closure and fracture intiation pressure for B-8 B to the pressures predicted by the Eldfisk model. With the stress arching correction the model clearly shows that sandface injection pressures were close to or exceeded the closure stress around B-8 B until May 2011. The observed permeability increase may therefore be related to expansion of natural fracture networks as the tensile strength of natural fractures can be assumed to be 0. This matches the findings of Walsh (1981), which showed that conductivity of natural fracture networks is highly stress dependent (Teufel and Rhett 1991). The permeability is no longer enhanced after the sandface injection pressure goes below the closure stress of the formation. The maintained permeability at injection pressures below the closure stress may, as discussed in Sections 4.4.1.2.4 and 5.4, be related to chemical interaction between the injected seawater and chalk in the expanded fractures.

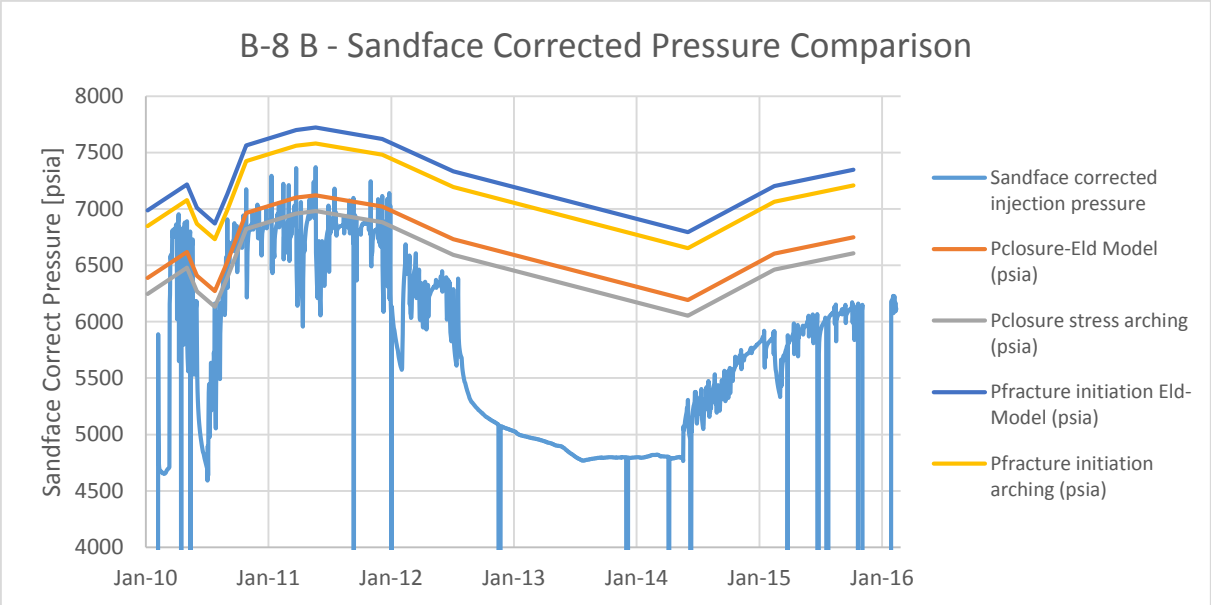

Figure 5.1: Comparison of arching corrected and original Eldfisk model closure and fracture initiation pressure for B-8 B. Stress release due to arching on the Crest leads to a reduction in the closure stress around B-8 B.

Figure 5.2 compares the stress arching corrected closure and fracture initiation pressure for B-22, to the Eldfisk model predicted pressures. With arching correction, both the closure and fracture initiation pressure exceed the sandface pressure at all times. This supports the results from Section 4.4.2.2, which indicate no change in B-22 reservoir properties when accounting for thermal effects. Assuming stress arching influence, the conclusion may therefore be drawn from B-22 and B-8 B, that the sandface injection pressure needs to exceed to fracture closure pressure in order to see an increase in reservoir conductivity.

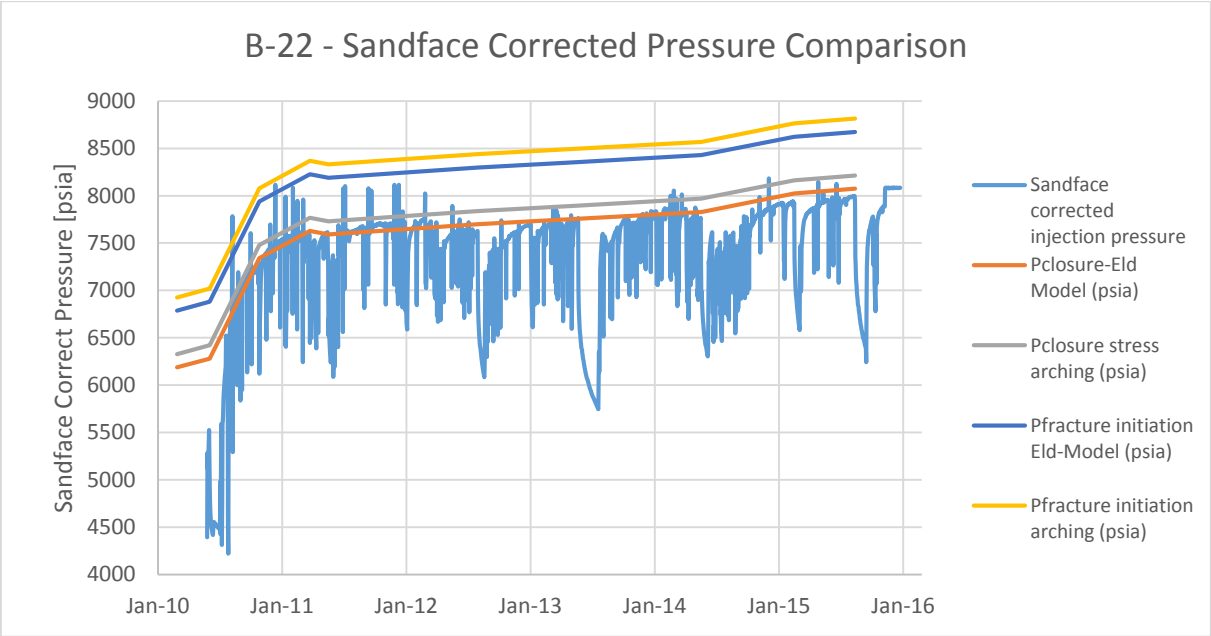

Figure 5.2: Comparison of arching corrected and original Eldfisk model closure and fracture initiation pressure for B-22. Stress increase on the flanks due to stress arching increases the closure stress in B-22.

5.1.1 Closure Pressure Based Conductivity Model

The results in the previous section have shown that when correcting closure pressure for stress arching, the closure stress could be a controller of reservoir conductivity. The proposed model for conductivity enhancement around injection wells is therefore based on the closure stress. For an injection well to enhance the near well natural fracture network, the injection pressure must exceed the near wellbore closure stress. The degree of enhancement will be a linear function of injected volume of water under these conditions (as shown in Figure 4.26), as the volume dictates the distance to which the enhanced conductivity zone is displaced. This also indicates that exposure to seawater and chemical alterations may be important for maintained permeability increase during reservoir depletion (Section 2.6).

The model combined with stress arching, suggests that conductivity increase may be hard to achieve in low permeability flank wells, unless high injection pressures are applied early. Once the reservoir pressure is increased, permeability enhancement cannot be achieved within allowable injection pressure limits (overburden limit).

For crestal wells permeability increase could be enhanced by overburden stress release due to stress arching. Uncontrolled conductivity growth could, however, be a contributing factor to the degree of B-8 B and PROD1 interaction (Section 4.4.1.5 and Figure 8.1, Appendix A), indicating that injection above fracture closure pressure requires continuous monitoring of injection periods.

The fracture initiation pressure will give a recommended upper limit for injection pressures, as fracture development in naturally fractured and faulted reservoirs is unpredictable (Fjær et al. 2008).

5.2 Shear Failure Model

If stress arching effects are negligible on the Eldfisk Field as indicated by Section 4.1.3.4, then the closure stress trends as described in Sections 4.4.1.4 and 4.4.2.4, are representative for B-8 B and B-22. In order to explain the difference in B-8 B and B-22 permeability development we then need to consider the stress history.

Sections 4.4.1 and 4.4.2 highlighted that the reservoir has been subject to significantly different pore pressure histories due to the structural placement of the two wells. Reservoir simulation indicates that the area around B-8 B was depleted to a minimum pressure of 2300 psia, while the B-22 area was only depleted to 3600 psia. Teufel and Rhett (1992) proposed that water injection would lead to local stress changes at the injection waterfront, which would be too small to impact the average response of the field. As a result, Teufel and Rhett (1992) assumed repressurization at the injection water front to be isotropic, which could be an explanation for the S-4 results in Section 4.1.5. As discussed in Section 2.5,

the minimum pressure experienced during depletion will dictate the shear stress during isotropic repressurization. B-22 and B-8 B have porosities in the range 31%-35% and should therefore have comparable failure envelopes (Teufel and Rhett 1991), which gives the conclusion that shear failure and therefore permeability enhancement during repressurization is more likely in B-8 B. Teufel and Rhett (1991) also showed that both cohesion and friction angle increase with decreasing porosity, which means that local shear failure of progressively lower porosity chalk should occur as the reservoir pressure increases. Figure 4.28 indicates that B-8 B reservoir pressure peaked in May 2011, which explains why no permeability increase is seen after this time. As shear failure occurs due to frictional sliding, fractures are expected to remain open during reservoir depletion, explaining the maintained permeability increase in B-8 B.

The shortfall in the shear failure model is the behavior seen in B-22. If stress arching is combined with the shear failure model, Figure 5.2 clearly shows that the effective stress near B-22 is always compressional. With negligible stress arching, effective stresses are extensional and B-22 should experience permeability enhancement through natural fracture expansion (Section 5.1). However, B-22 PTA revealed that the impact of natural fracture networks may be small in B-22 (Section 4.4.2.2.2). With tensile failure mode as the failure mode during repressurization due to the high minimum pressure in the area, it may be required for B-22 to induce tensile injection fractures to see significant conductivity increase. The sandface injection pressures never exceed the fracture initiation pressure, and the lack of permeability increase may therefore be interpreted as an indication of low natural fracture density. It must however be stated, that to the Author it is hard to justify low fracture density in a well with an initial injection rate of 35 000 bbl/D. The deviation could therefore also be linked to uncertainty in the determined pore pressure (Section 4.4.3.1).

The shear failure model could also be combined with the stress arching closure stress model from Section 5.1. Due to the low minimum reservoir pressure in the B-8 B area, shear failure may occur before tensile failure and therefore be the primary failure mode. Shear failure will, as discussed above, explain the observed permanent permeability increase in the area. For B-22, stress arching results in elevated closure stress, preventing natural fracture expansion in the area. The low shear stress due to the high minimum pressure will prevent shear failure under compressional minimum stress conditions. It is however important to note, that stress arching will impact the shear stress in accordance with Equations 2.11 and 2.16. Stress arching will therefore lead to increased shear stress on the flanks of the structure and decreased shear stress towards the crest of the structure. This would increase the likelihood of shear failure on the flanks and reduce the risk of shear failure towards the crest, counteracting some of the effects described above.

5.3 Inelastic Deformation

The studies of several authors have shown that inelastic deformation behavior, such as creep, is prominent in chalk cores (Omdal et al. 2009, Omdal et al. 2010, Madland et al. 2011, Megawati et al. 2011, Nermoen et al. 2015). In addition, pore collapse has proven to be prominent in high porosity chalk (Risnes 2001). All these deformation effects are inelastic, and their impact on the stress equilibrium and fracture propagation is unclear. As previously discussed, pore collapse is a failure mode in which the rock strength increases. Time dependent pore and microfracture compaction (creep) will therefore result in a time-dependent change in the failure envelope of the reservoir rock. The closure stress analysis in Section 4.1 shows that field stress data conforms to a linear closure stress trend, which suggests that inelastic effects do not have a prominent impact on the stress equilibrium on Eldfisk. Goulty (2003) similarly showed that the Ekofisk depletion stress path conformed to poroelastic behavior, despite significant reservoir compaction (Doornhof et al. 2006). However, Section 4.1.6.6 referenced to Teufel and Warpinski (1990) who concluded that nonlinearity invalidates most theoretical and mechanistic models, and results by Omdal et al. (2010) indicated predominantly viscoplastic (Omdal 2016b) creep behavior in chalk under reservoir conditions (Section 2.7.1). One can therefore not conclude that inelastic effects do not impact the closure stress trend on Eldfisk, but the results clearly indicate that the effects do not lead to a non-linear shift of the closure trend.

The observed linear closure stress trend in Section 4.1 may also indicate that plastic deformation through pore collapse creates a new rock with different elastic properties. The reduction in porosity is irreversible and inelastic, but the new rock material may still behave partially elastic and therefore conform to a linear closure trend. Under this concept of elasticity, the plastic deformation will impact the closure trend, but is expected to primarily lead to a shift over time towards a trend dictated by lower porosity chalk. These indications are supported by Teufel and Rhett (1992) who suggested elastic behavior after pore collapse on the Ekofisk Field.

The porosity data shown in Section 4.1.3.1 also shows that high porosity (38%+) chalk zones can be found in extensively depleted parts of the reservoir (3000 psi pore pressure). This directly contradicts the failure envelopes and depletion stress paths determined by Teufel and Rhett (1991) for Ekofisk chalk cores. The results can be interpreted as an indication of varying rock strength for similar porosities across the field. The expected shear strength variation due to porosity variations may therefore be less than predicted by Teufel and Rhett (1991). Alternatively, the results may indicate that pore pressure depletion has led to shear failure, rather than pore collapse in some parts of the field. Risnes (2001) attributed both failure mechanisms to shear failure at grain contacts, where large differential stresses organized shear failure between grains into well-developed shear planes. This could potentially be a result of local arching effects increasing shear stress as discussed in Section 5.2.

5.4 Water Weakening

The concept of water weakening may be important for both the proposed failure models in Sections 5.1 and 5.2. As discussed in Section 2.6, water weakening may also impact the reservoir conductivity development. This section will highlight how water weakening could impact some of the results and conclusions drawn so far in this thesis.

5.4.1 Reservoir Stress Equilibrium

As shown in Section 4.1.1, the Eldfisk minimum horizontal stress conforms to a linear trend as a function of pore pressure. As discussed in Section 5.3, this may be due to a combination of both elastic and plastic deformation effects. Under uniaxial-strain conditions the elastic component of the deformation will be a function of the Poisson's ratio as seen in Equation 2.19 (Section 2.4.1). Studies by Madland et al. (2002) on Liège outcrop chalk showed ~33% reduction in Poisson's ratio (from 0.24 to 0.16, Figure 2.14, Section 2.5) when glycol was replaced by water as the saturating fluid at 130 ^{o}C (Ekofisk reservoir temperature (Madland et al. 2002)). According to Equation 2.19 a reduction in Poisson's ratio during waterflooding would increase the slope of the elastic component of the closure stress trend in Figure 4.1 (Section 4.1.1). The relative contribution of elastic and plastic components would then dictate the impact of reduced Poisson's ratio on the overall closure trend. Teufel (2007) indicated that the closure stress trend in the Eldfisk Field deviated significantly from a uniaxial strain assumption (~3 times lower measured than theoretical stress path K (Section 2.4.3)), which suggests that plastic deformation effects may dictate the closure stress trend in Figure 4.1. Waterflooded sections of the reservoir should then show stress equilibrium following the trend shown in Figure 4.1. Oppositely, Goulty (2003) indicated close to poroelastic behavior for the depletion stress data from the Ekofisk Field. It is therefore apparent that closure stress data from waterflooded sections of the reservoir are required to properly evaluate closure stress development near injection wells.

Madland (1999) showed that water saturations in excess of 1-2 % were required to mobilize the water weakening effect at ambient temperature conditions (Risnes 2001). This is supported by the results in Section 4.1.3.2, which show no correlation between closure stress and formation water saturation in zones where the minimum water saturation is 3 %. Assuming that the critical saturation (1-2 %) is the same at ambient and reservoir temperature, the Poisson's ratio effect shown by Madland et al. (2002) should already impact the closure stress trend in Figure 4.1. Several authors have shown that water composition impacts the hydrostatic yield strength of chalk cores (Madland et al. 2002, Heggheim et al. 2005, Risnes et al. 2005, Korsnes et al. 2008, Liteanu and Spiers 2009, Omdal 2010, Liteanu et al. 2013, Megawati et al. 2013), and chalk elastic properties are therefore expected to change when formation water is replaced by seawater. However, no studies have been found that examine the relationship between fluid composition and Poisson's ratio at varying temperatures.

5.4.2 Chalk Strength

Risnes (2001) concluded that for high porosity outcrop chalk, all failure mechanisms (tensile, shear and pore collapse) are a result of yielding in shear between grains (Sections 2.1.3.4 and 2.7.1). The yielding may be due to frictional sliding or breaking of bonds between grains (Risnes 2001). Processes that reduce the cohesion between chalk grains or reduce friction between grains, should therefore also reduce the tensile and shear strength of the chalk matrix.

Megawati et al. (2013) showed that sulphate (SO_4^{2-}) will adsorb to the calcite surface creating a negative surface charge (Megawati et al. 2013). This negative surface charge can give rise to a disjoining pressure when two charged surfaces approach each other (Megawati et al. 2013). The amount of adsorbed sulphate increases with injected concentration and decreases with temperature (Megawati et al. 2013). The repulsive disjoining pressure will reduce the cohesive forces near grain contacts (Megawati et al. 2013), which was suggested to reduce the yield point of tested chalk cores (Megawati et al. 2013). Injection of seawater (rich in sulphate) could therefore increase the disjoining pressure at grain contacts, reducing the fluid pressure required to cause failure between the chalk grains. The injection tests used to determine fracture initiation pressures in Section 4.2 utilize fresh water, and the effective fracturing differential pressure when injecting seawater should therefore be lower than the 600 psi determined in Section 4.2.2. The increased disjoining pressure may also increase the likelihood of shear failure near the injection well.

Fjær et al. (2008) indicated that the thermal front moves at 30-50 % of the rate of the flood front (Section 2.2.1.6). Megawati et al. (2013) showed that sulphate adsorption is approximately two times higher at 130 ^{o}C than at 50 ^{o}C. As the reservoir is cooled around the injection well, the disjoining pressure induced by sulphate adsorption is expected to decrease, and the fracturing differential pressure may therefore over time approach the 600 psi determined in Section 4.2.2.

In addition, Røyne et al. (2015) examined nanometer-scale adhesive forces between calcite crystals in water-glycol mixtures at ambient temperature. The fraction and value of adhesive measurements decreased with increased water concentration (Røyne et al. 2015). Based on this, Røyne et al. (2015) concluded that there are strong, short-range repulsive forces between calcite crystals in water, which can be attributed to water adsorption. Assuming that similar effects can be observed at reservoir temperature, these results indicate that increased water saturations in the reservoir may reduce the cohesion between chalk grains (Røyne et al. 2015), reducing the tensile, shear and yield strength of the chalk (Risnes 2001, Megawati et al. 2013). Water is injected in the minifrac Step Rate Tests (Section 3.2), and whether water adsorption effects are present in the fracture initiation pressure measurements in Section 4.2.2, will therefore depend on the time-dependency of the water

adsorption. The experiments by Røyne et al. (2015) were conducted on the same fragments with only 10 min between fluid exchange, indicating that the adsorption is fast. This is supported by Nermoen et al. (2015) who suggested that adsorption reactions are fast time-independent reactions, which indicate that disjoining pressure due to water adsorption should be measured in the results in Section 4.2.2. The results should then correctly represent the fracture initiation pressure near water injectors.

Studies conducted by Zimmermann et al. (2015), Megawati et al. (2011) and Gautier et al. (2001), showed that dissolution can lead to rounding of the calcite minerals in the chalk matrix. Megawati et al. (2011) proposed that grain rounding may decrease the intergranular friction between chalk grains, potentially reducing the tensile, shear and yield strength of the chalk (Risnes 2001). However, mineral dissolution is associated with precipitation (Madland et al. 2011, Nermoen et al. 2015, Zimmermann et al. 2015), and precipitation could result in increased intergranular friction (Megawati et al. 2011). Studies by Feazel (2007) of cores from the K-9 A injector drilled on the Ekofisk Field (Section 2.6), showed evidence of dissolution grain rounding, but limited precipitated minerals (Feazel 2007). As dissolution and precipitation are time-dependent processes (Nermoen et al. 2015), dissolution grain rounding could result in reduced tensile and shear strength around injection wells over time.

5.4.3 Compaction

Subsidence and compaction monitoring on the Ekofisk Field have shown continued compaction and subsidence despite reservoir repressurization (Hermansen et al. 1997, Doornhof et al. 2006, Nermoen et al. 2015). The continued compaction after repressurization has been attributed to water weakening of the chalk (Jensen et al. 2000, Doornhof et al. 2006, Nermoen et al. 2015). Nermoen et al. (2015) referenced several authors, who indicated that subsidence rates in zones in contact with the injected seawater were only reduced to ~1/3 the rate prior to waterflood implementation. An observation well on the Ekofisk Field supported the indications, showing that most of the compaction following repressurization was concentrated in zones contacted by seawater (Doornhof et al. 2006).

Megawati et al. (2013) and Korsnes et al. (2008) indicated increased water weakening induced creep and compaction with increasing temperature. Personal communication with Merete Madland (2016) outlined that several experiments on chalk cores have indicated a critical transition temperature for water weakening around 50 – 60 ^{o}C. As outlined in Section 2.2.1.6, the thermal front around the injection well will move at 30 – 50 % of the rate of the waterfront (Fjær et al. 2008). Due to the thermal dependency of the water weakening, there may be several zones with local variations in compaction rate between the injector and the producer. Following the indications by Doornhof et al. (2006), the zone of high temperature water between the thermal and waterfronts should show highest compaction rates. These effects may lead to local stress arching in the overburden above the reservoir.

The area around the injection wells is exposed to the largest volumes of seawater (source of injected seawater), and should therefore show largest cumulative compaction due to water weakening. In addition, concentration of some specific ions in the injected water will impact the compaction rate (Hiorth et al. 2011, Nermoen et al. 2015). The concentration will be highest at the injection well and reduce as ions interact further into the reservoir (Hiorth et al. 2011). These effects could potentially lead to a local partial overburden stress release near the injection well, reducing the horizontal stress as outlined in Section 5.1.

However, Doornhof et al. (2006) also showed that pore pressure was important for the compaction rate, with reduced compaction rate for increased pore pressure. This is natural as increased pore pressure reduces the effective stress on the rock matrix (Equation 2.4, Section 2.1.2) (Nermoen et al. 2015). Pore pressure decreases from the injector towards the producer, with the pore pressure gradient as a function of reservoir permeability. Higher gradients are observed in lower permeability parts of the reservoir. High pore pressure gradients will counteract some of the described water weakening compaction effects, and local stress arching may therefore be less important in lower permeability parts of the reservoir. With maximum permeability of ~4 mD in B-8 B (Section 4.4.1) and ~0.5 mD in B-22 (Section 4.4.2.2.3), local stress arching should be more prominent in the area around B-8 B. The permeability increase over time around B-8 B (Section 4.4.1.2.4), also indicates that local stress arching effects could increase with time due to reduced pore pressure gradients.

5.4.4 Permeability Development

Nermoen et al. (2015) reported the results of a 1072 day flooding experiment conducted on a Liège outcrop chalk core during mechanical compaction at 130 ^{o}C (Ekofisk reservoir temperature (Madland et al. 2002)). The experiment examined volumetric strains, porosity and permeability development during long term flooding of nonequilibrium brines. The permeability development in particular showed abnormal evolution (Nermoen et al. 2015). After 112 days of flooding the permeability was reduced from ~0.6 mD to a minimum of ~0.1 mD. Nermoen et al. (2015) explained this as a result of porosity reduction from ~40 % to ~30 %, due to rapid pore collapse and compaction caused by sulphate adsorption (Section 5.4.2) (Megawati et al. 2013, Nermoen et al. 2015). Following the permeability reduction, the permeability increased slightly to ~0.15 mD after ~400 days total experiment time (Nermoen et al. 2015). Nermoen et al. (2015) explained this as an indication of dissolution rather than compaction controlling the permeability dynamics, as despite volumetric creep the porosity increased from ~30 % to ~35 % during the same period. From 400 days until the end of the experiment, the permeability remained relatively constant, despite increase in porosity to ~40 % after 1072 days. Nermoen et al. (2015) suggested forming of secondary minerals with larger specific surface area could explain the stable permeability after 400 days.

The results by Nermoen et al. (2015) are of interest when discussing the results from the analysis of B-8 B and B-22 (Sections 4.4.1 and 4.4.2, respectively). Neither B-8 B nor B-22 observe an initial fast permeability decrease due to early pore collapse, as seen in the experiment by Nermoen et al. (2015). Both B-8 B and B-22 are initially flooded with porosities in the range of 31-35 %, suggesting that adsorption controlled pore collapse may and should have already occurred (Nermoen et al. 2015). Following the results by Nermoen et al. (2015), the permeability dynamics around B-8 B and B-22 should then be controlled by dissolution and precipitation. As discussed in Section 4.4.3.2, B-22 shows close to constant permeability when correction for viscosity effects. This is in line with the stable permeability seen after 400 days in the experiments by Nermoen et al. (2015), and could indicate a dissolution and precipitation maintained permeability around B-22.

However, B-22 is situated on the flank of the Eldfisk Bravo structure (Figure 8.1, Appendix A), and pore pressure is increasing around the well (Figure 4.35, Section 4.4.2.4). Compaction and subsidence rates are lowest on the flanks of the reservoir structure (Nagel 1998, Krivonogov 2016), and increased pore pressure will further reduce the compaction rate (Doornhof et al. 2006). Maintained permeability in B-22 could therefore, opposite to the previous, be interpreted as an indication of very limited dissolution, and therefore not the porosity increase seen in the experiments by Nermoen et al. (2015). This interpretation corresponds well with the results by Feazel (2007), who showed only limited dissolution and precipitation in the chalk matrix only 50 m (165 ft) from a ~200 MMBBL seawater injection well on the Ekofisk Field (Section 2.6). Hiorth et al. (2011) indicated significant chemical reactions from Ekofisk produced water analysis. The interpretation of limited dissolution, could then be suggested as another indication that the majority of chemical alterations in the reservoir occur in the vicinity of the natural fracture network, rather than the chalk matrix (Section 2.6).

B-8 B also showed maintained permeability after ~12 MMBBL of injected seawater (Section 4.4.1.2.4). This corresponds with the results by Nermoen et al. (2015), but conclusions on controlling mechanisms are not possible as permeability variations are also a function of fracture aperture in the area around the well (Section 5.1).

Another important indication from the results by Nermoen et al. (2015), is that injection into unflooded sections of the reservoir could potentially lead to early rapid pore collapse. This pore collapse can in turn lead to a significant loss in permeability in the flooded section around the well (Nermoen et al. 2015). This would lead to a reduction in well injectivity and increase of the pore pressure gradients around the wellbore. Higher pore pressure gradients will increase the near wellbore pore pressure, which was suggested in Section 5.1 to prevent expansion of the natural fracture networks around B-

22. As B-8 B and B-22 were drilled in flooded sections of the reservoir, these trends could not be seen in the analyzed datasets.

As referenced in Section 2.6, Madland et al. (2015) showed during seawater injection in fractured chalk cores, that chemical alterations were concentrated in and around the fracture networks. These alterations may lead to partial filling of the fractures influencing the reservoir conductivity (Madland et al. 2015). As earlier mentioned (Section 5.1), this may explain the maintained permeability in B-8 B after the effective stresses become compressional. B-8 B was flooded at the time of drilling (Appendix B: B-8 B CPI), but Hiorth et al. (2011) showed that chemical alterations will continue as more seawater is injected. The enhanced fracture aperture around B-8 B may therefore experience extensive chemical alterations which could influence the fracture geometry and lead to partial fracture filling. The fracture aperture of the partially filled fractures would then be less sensitive to the compressional stresses caused by the decreased injection pressures (Teufel et al. 1993). As a consequence, fracture systems subject to seawater injection may have less stress dependent permeability during depletion. This also corresponds well with the indications in Sections 4.4.1.2.4 and 5.1.1, which suggested that the permeability enhancement in B-8 B was a function of the position of the flood front. Madland et al. (2015) also showed a concentration of silicates in the fracture networks, suggesting that local variations in concentration of non-carbonate minerals may influence the filling of the fractures. Variations in non-carbonate mineral content could then potentially influence the stress dependency of the reservoir conductivity during seawater flooding.

Furthermore, Section 2.6 also referenced experiments conducted by Madland et al. (2015) on fractured chalk cores with tensile fractures created with a Brazilian cell. Seawater flooding resulted in a complete closure of the formed fracture by precipitated minerals (Madland et al. 2015). This suggests that chemical alterations in natural fracture systems could also lead to reduced fracture permeability. However, as referenced in Section 2.6, Teufel et al. (1993) outlined that most of the natural fractures in the Ekofisk Field, and therefore likely in the Eldfisk Field, were formed through shear failure. As discussed in Section 2.1.3.4, shear failure, unlike tensile failure, causes a sliding along the fracture plane. This will prevent overlapping of asperities and can give a larger open fracture aperture than tensile fractures. Complete closure as seen in the experiments by Madland et al. (2015), should therefore be less likely in the natural fracture networks seen in the reservoir. This conclusion is also supported by the results of the analysis in B-8 B (Section 4.4.1), which throughout the injection period shows permeability clearly enhanced by open natural fracture networks.

5.5 Dual Porosity Systems

Naturally fractured reservoirs, such as the Eldfisk chalk field are often referred to as dual porosity systems (Abdassah and Ershaghi 1986). The primary conduits of flow in the reservoir are the natural fractures, while the primary storage of oil is in the chalk matrix. Flow towards the wellbore is through the fractures with oil displaced from the matrix into the fractures through imbibition. The consequence of this dual porosity system is a significant pressure contrasts between the high permeability fractures and low permeability matrix. As the matrix makes up the majority of the system, the matrix fluid pressure will govern the stress equilibrium in the system. The higher pressure in the fractures should therefore promote natural fracture network expansion.

In falloff and flow responses in dual porosity systems, the initial early response is from the higher permeability fractures (Abdassah and Ershaghi 1986). As seen from the falloff responses from B-8 B and B-22, no dual porosity behavior is visible, confirming that the fracture volume in the chalk is very small compared to the matrix volume. This is illustrated in Figure 5.3, where a dual porosity system with matrix storage volume 1000 times higher, and matrix permeability 1000 times lower than the fractures, gives a good match of the falloff response in B-8 B. Falloff responses should therefore quickly exhibit a response representative of flow capacity and pressure of the rock bulk. The determined reservoir pressure from falloff analysis should therefore give good estimates of fracture closure pressure, while natural fracture networks will allow for propagation of the wellbore pressures.

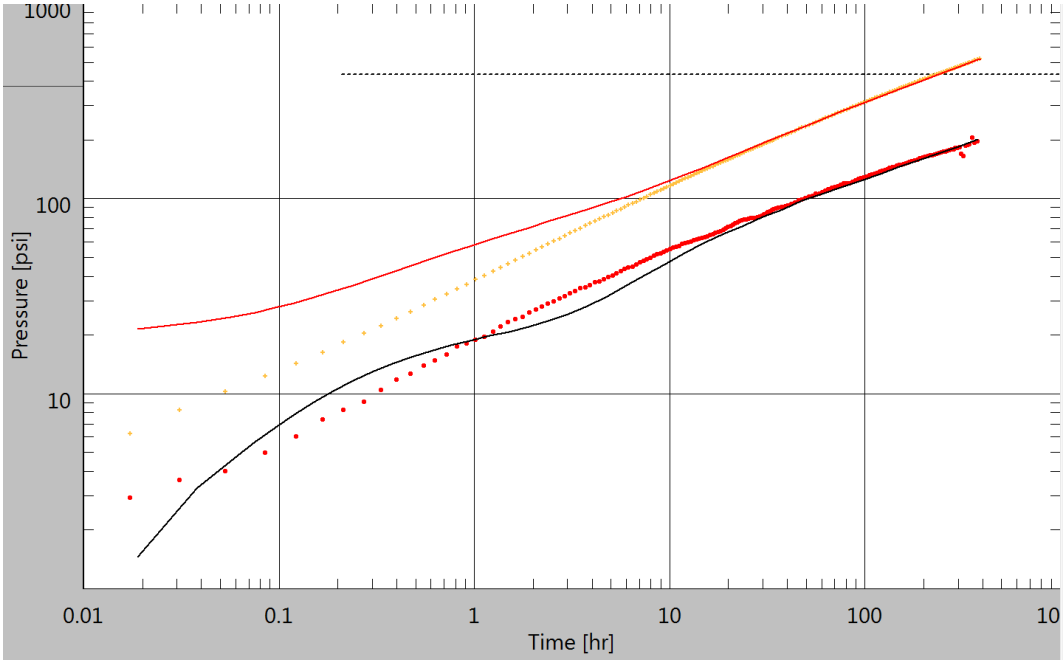

Figure 5.3: The figure shows a model match of the B-8 B falloff in February 2015 using a dual porosity model. Pressure drops are shown in orange points, semilog derivatives in red points and model match in red and black lines, respectively. The model has matrix storage volume 1000 times higher and matrix permeability 1000 times lower than the fracture network. This illustrates that falloff responses on Eldfisk should quickly be representable of bulk reservoir properties and pressures. Plot generated with Saphir, Kappa Engineering © 2016.

5.6 Eldfisk-Ekofisk Differences

The results in Section 4.1.2 showed that the calculated depletion stress path for the Eldfisk data in this thesis was higher (0.28) than the stress path determined for the Ekofisk Field (0.2). Teufel (2007) underlined that due to significant inelastic deformation induced by pore collapse in chalk, the measured stress path will deviate from theoretical uniaxial-strain deformation stress paths. The stress path followed by the reservoir will in addition to the elastic properties of the reservoir rock, also depend on (Teufel 2007):

- Boundary condition of the reservoir
- Size and geometry of the reservoir (Goulty 2003)
- Reservoir depth
- Poroelastic properties and deformation behavior of the bounding formations
- Rock-fluid interactions (Risnes 2001, Madland 2005, Omdal 2010, Megawati et al. 2011)
- Inelastic deformation effects

The Ekofisk and Eldfisk fields have significantly different reservoir geometry, and the Ekofisk waterflood is significantly more mature than the Eldfisk waterflood (Section 1.3.1). A difference in depletion stress path, as shown by the results, is therefore to be expected. The results indicate that the narrower and less water weakened Eldfisk reservoir, shows a greater change in effective horizontal stress as a function of change in effective overburden stress than the Ekofisk reservoir.

Madland et al. (2002) indicated that Poisson's ratio and therefore uniaxial stress path, decreases with increasing water saturation, potentially relating some of the differences to waterflood maturity. However, as results from Teufel and Rhett (1991) match the 0.2 Ekofisk model stress path (Section 4.1.2), the measured Ekofisk depletion stress path has not changed significantly from 1991-2014. This suggests that waterflood maturity is not important for the Ekofisk-Eldfisk difference, or that trends primarily determined from oil zones indicate that water weakening can only lead to localized stress changes in the contacted zone.

The stress path variations between Eldfisk and Ekofisk, could then primarily be attributed to the difference in reservoir structure. As the Eldfisk reservoir is significantly narrower than the Ekofisk reservoir, stress arching will be more pronounced on the Eldfisk Field (Nagel 1998). However, as most of the datapoints are sampled from crestally located wells, this should lead to a stress release and therefore decrease in minimum horizontal stress (Sections 2.4.2 and 5.1). This is opposite of the observed trend (Figure 4.1, Section 4.1.1), but matches the observations by Teufel (2007), which indicated a measured Eldfisk depletion stress path of 0.16. This could also indicate, that most of the new analyzed wells show flank stress characteristics, and that the definition of flank stress regions

stretches further towards the crest of the reservoir structure than that applied in Section 4.1.3.4. Considering the discussion in Section 4.1.2, this may also indicate that the pumped fluid volumes in minifrac injection tests in horizontal wells, are inadequate to accurately measure the correct minimum in-situ stress (discussed in Section 2.2.1.5). The 0.16 stress path measured from vertical well data analyzed by Teufel (2007), could therefore be more correct. However, Zoback and Zinke (2002) reported a depletion stress path of 0.3 on the crest of the Valhall chalk field, and Hillis (2001) reported a 0.27 stress path from exploration wells within a 50 km radius of the Ekofisk Field (Goulty 2003). The 0.28 depletion stress path determined for the Eldfisk Field (Section 4.1.1) is therefore well within the regional variations.

5.7 Fracture Mechanics

The Pressure Transient Analysis of minifrac Step Rate Tests in Section 4.3 have shown the impact of high pressure injection on reservoir chalk formations. High rates injected into thin stimulation zones at high pressures, seem to form single extensive fractures. These may limit the area exposed to acid in the following acid stimulation, as acid may be preferentially channeled through the previously formed fracture (Omdal et al. 2008). Longer perforated zones show strong conductivity response, potentially indicating natural fracture network expansion, but also indicating multiple induced tensile fractures. Multiple induced tensile fractures could potentially be preferential for the acid stimulation as more of the perforated length is exposed to the acid. The analysis is limited, as reservoir properties cannot be thoroughly assessed with only 5 analyzed datasets. The results may however indicate that there is a relationship between the injection rate, perforation length, and the number of formed tensile fractures. The number of formed tensile fractures is also expected to be sensitive to pore pressure distribution, borehole imperfections and natural fracture densities.

Evaluating mechanisms controlling the number of fractures can be important for optimizing acid stimulation treatments. Variations in the number of formed fractures will result in variations in fracture dimensions. When water injection wells inject through all zones this may lead to an uneven distribution of the injection water, increasing the risk of reduced sweep efficiency.

5.8 Biot Stress Coefficient

As shown in Section 2.3, Omdal et al. (2009) showed variation in Biot stress coefficients in chalk core experiments under hydrostatic loading with constant differential stress ($\sigma_{ext} - p_f$). Hydrostatic loading is similar to an isotropic loading process in the sense that the magnitude of all stresses are changed uniformly. If the results by Omdal et al. (2009) are assumed applicable for isotropic repressurization, which was postulated by Teufel and Rhett (1992) at the water injection front, it could indicate a significant decrease in Biot stress coefficient at the injection front. The effect would be most

prominent in high porosity chalk (Omdal et al. 2009). From the uniaxial strain relation derived in Equation 2.20 (Section 2.4.1), a reduction in Biot stress coefficient at the waterfront would lead to a significant reduction in closure stress. This would indicate that lower pressures are required for natural fracture network expansion and tensile fracturing at the waterfront. This may in part be supported by the analysis results for B-8 B (Section 4.4.1), which indicate that the permeability enhancement is a linear function of the injected volume, and therefore a function of the waterfront position.

However, if the repressurization at the waterfront is assumed isotropic, the change in all effective stress magnitudes will be equal, resulting in a repressurization stress path K (Section 2.4.3) equal to 1 (Teufel and Rhett 1992). Under these conditions Equation 2.20 (Section 2.4.1) would give a slope 0, such that $\Delta\sigma_h = 0$. Under isotropic conditions at the waterfront, an increase in pore pressure would not lead to an increase in closure stress. Compared to a trend following the depletion stress path K (Section 2.4.3) of 0.28 determined in Section 4.1.1, isotropic repressurization would therefore lower the pressures required for natural fracture network expansion and tensile fracturing at the waterfront.

5.9 Injection Regulation to Control Reservoir Conductivity

The findings from B-8 B and B-22 indicate that sandface injection pressure relative to the fracture closure pressure may control the observed conductivity increase. This would also indicate that conductivity enhancement can be controlled by varying the sandface injection pressure relative to the changes in near wellbore reservoir pressure. The analysis for B-8 B (Section 4.4.1) showed that injecting before stimulation lead to sandface injection pressures significantly exceeding the closure pressure. In B-22 low reservoir permeability led to fast near wellbore pressure buildup, which prevented exceeding of closure stress even at high initial injection rates (Section 4.4.2). In order to achieve a conductivity enhancement in low permeability flank wells such as B-22, injection pressures would then need to be increased very early, or initial injection be conducted prior to reservoir stimulation. Alternatively, addition of friction reducers to the injection water would also increase the sandface pressure.

6 Conclusions

Analysis of Eldfisk pre-acid stimulation tests have shown that the Eldfisk closure stress conforms to a linear trend as a function of formation pore pressure. A new model has been proposed for closure stress prediction on Eldfisk, and estimates that the Eldfisk reservoir follows a depletion stress path K equal to 0.28 with a model intercept of 0.31 psi/ft. The Eldfisk closure pressures deviate from the 0.2 stress path for the Ekofisk Field, and indicate higher minimum in-situ stress (σ_h) than on Ekofisk. The linear closure stress trend is seen despite significant inelastic deformation reflected in pore collapse during depletion. This suggests that the collapsed chalk continues to act as an elastic material with properties corresponding to the new porosity. An analysis of old Eldfisk stimulation data for vertical wells is recommended to validate that the determined closure stress deviations are not due to high inclination horizontal wellbores. Any deviation due to wellbore inclination would indicate that the pumped volumes in the minifrac tests are too small to properly orient the induced fracture.

Analysis of minifrac Step Rate Tests have shown that the difference between fracture initiation pressure and fracture closure pressure is on average 600 psi within ±150 psi. The difference is independent of pore pressure, and indicates that fracture initiation pressure in perforated zones is controlled by a relatively constant stress concentration around the wellbore. This constant difference means that a reliable estimate of the reservoir fracture gradient can be made from pore pressure estimates and the new closure stress model. Discussions in Section 4.4.3.3 have also indicated that the fracture initiation pressure is expected to be representable for the fracture reopening pressure after acid stimulation.

Results from Pressure Transient Analysis of minifrac Step Rate Tests have indicated that valuable information can be obtained from analysis of short Step Rate Tests. The results show significant uncertainty, but still indicate important aspects of fracture mechanics. Perforation length seems to be an influencing factor in the conductivity and skin development around the stimulated zones. Longer stimulation zones appear to see multiple fracture growth reflected in significant conductivity growth. Shorter stimulation zones show constant reservoir conductivity, suggesting growth of larger single fractures.

Pressure Transient Analysis of B-8 B and B-22 have shown no significant tensile fracture growth. B-8 B showed ~4-times increase in reservoir conductivity over 9 months of injection after the acid stimulation. A closure pressure based conceptual model that accounts for stress arching, has shown that the B-8 B permeability increase could be explained by expansion of the natural fracture networks. The stress arching correction is an estimate, and should be validated with Eldfisk overburden modelling. Expansion of natural fracture networks occur once the minimum stress in the near wellbore

area becomes tensile. B-8 B permeability is maintained after the 9 months of increase, despite calculations indicating compressional effective stresses. Chemical alterations as a result of seawater injection are proposed as a potential mechanism controlling the maintained permeability. Mobilization of silicates and precipitation of magnesium-bearing minerals and anhydrite, could lead to partial filling of the opened fractures (Madland et al. 2015), preventing closure when pressures are reduced.

B-22 has shown decreasing matched permeability in the Pressure Transient Analysis, which is explained as an actual indication of reservoir cooling and water viscosity increase. The closure stress based conceptual model with increased flank overburden stress due to stress arching, suggests that injection pressures in B-22 have been too low to see natural fracture network expansion. The results indicate that permeability improvement could potentially be achieved on the reservoir flanks if injection pressures are increased early.

The conclusions on closure stress for B-8 B and B-22 are very sensitive to the estimated reservoir pressure. The pressure will be uncertain, and future assessments could potentially be improved by finite element modelling to estimate near wellbore pore pressure during injection.

Shear failure is not ruled out as a mechanism explaining the permeability development in B-8 B and B-22. A shear failure model adds significant complexity due to the dependency on stress history, inelastic effects and water weakening. Results have suggested that stress arching may not be significant on the Eldfisk Field (Section 4.1.3.4), which then would require shear failure to explain the permeability increase in B-8 B. Without stress arching B-22 sees extensional stresses, and it is therefore suggested that closure stress influenced by stress arching is a better model for explaining the development in the two wells.

Detailed PTA of interaction between B-8 B and a nearby producer, has indicated strong communication between the two wells. Collapse in the nearby producer due to massive water breakthrough is explained by strong fault interaction seen in the B-8 B flowing response. The fault interaction is a temporary effect seen as increased conductivity in the area contacted by B-8 B. The fault communication is limited to a period of 5-6 months, and disappears once the producer is lost. These results may indicate that natural fault networks, rather than induced tensile fractures, represent the most prominent risk of undesired injector-producer communication.

The results in this thesis have highlighted that closure stress together with Pressure Transient Analysis can increase our understanding of how seawater injection impacts chalk reservoirs. The results are based on a relatively limited number of data, and will as a consequence be uncertain. PTA of more injection wells and addition of stimulation data from older wells, are therefore recommended to evaluate and potentially validate the indications in this project.

7 References

Aadnoy, B. and R. Looyeh (2011). *Petroleum rock mechanics: drilling operations and well design*, Gulf Professional Publishing.

Abdassah, D. and I. Ershaghi (1986). "Triple-porosity systems for representing naturally fractured reservoirs." *SPE Formation Evaluation* **1**(02): 113-127.

Aronofsky, J. and R. Jenkins (1954). "A simplified analysis of unsteady radial gas flow." *Journal of Petroleum Technology* **6**(07): 23-28.

Barree, R., V. Barree and D. Craig (2007). Holistic Fracture Diagnostics. Paper SPE 107877 presented at the SPE Rocky Mountain Oil and Gas Techology Symposium, Denver, Colorado, 16-18 April.

Barree, R. and H. Mukherjee (1996). Determination of Pressure Dependent Leakoff and its Effect on Fracture Geometry. Paper SPE 36424 presented at the SPE Annual Technical Conference and Exhibition, Denver, 6–9 October, ISBN 978-1-55563-423-0.

Beal, C. (1946). "The viscosity of air, water, natural gas, crude oil and its associated gases at oil field temperatures and pressures." *Transactions of the AIME* **165**(01): 94-115.

Biot, M. A. (1941). "General theory of three-dimensional consolidation." *Journal of applied physics* **12**(2): 155-164.

Carey, M. A., S. Mondal and M. M. Sharma (2015). *Analysis of Water Hammer Signatures for Fracture Diagnostics*. SPE Annual Technical Conference and Exhibition, Society of Petroleum Engineers.

Charlez, P. A. (1991). "Rock Mechanics, Volume 1, Theoretical Fundamentals." *Éditions Technip, Paris*.

ConocoPhillips (2013). Workflow-Fracture Closure Analysis. ConocoPhillips Norway**:** 29.

ConocoPhillips (2015). Geotap Pressure Analysis Report. ConocoPhillips.

ConocoPhillips and D. D. Cramer (2015). Reexamining DFIT Interpretation Methods. SPE Gulf Coast Section Completions & Production Study Group Luncheon.

Detournay, E. and R. Carbonell (1997). "Fracture-mechanics analysis of the breakdown process in minifracture or leakoff test." *SPE production & facilities* **12**(03): 195-199.

Doornhof, D., T. G. Kristiansen, N. B. Nagel, P. D. Pattillo and C. Sayers (2006). "Compaction and subsidence." *Oilfield Review* **18**(3): 50-68.

Economides, M. J. and K. G. Nolte (2000). *Reservoir stimulation*, Wiley Chichester.

Eltvik, P., T. Skoglunn and A. Settari (1992). *Waterflood-induced fracturing: water injection above parting pressure at Valhall*. SPE Annual Technical Conference and Exhibition, Society of Petroleum Engineers.

Feazel, C. (2007). K-09A_SEM_views (ConocoPhillips internal document). ConocoPhillips.

Fekete. (2014). "Minifrac Test Analysis." Retrieved February 4, 2016, from http://www.fekete.com/san/webhelp/welltest/webhelp/Content/HTML_Files/Analysis_Types/Minifrac_Test_Analyses/Minifrac_Test_Analyses.htm.

Fjær, E., R. M. Holt, A. Raaen, R. Risnes and P. Horsrud (2008). *Petroleum related rock mechanics*. Oxford, UK, Elsevier.

Gautier, J.-M., E. H. Oelkers and J. Schott (2001). "Are quartz dissolution rates proportional to BET surface areas?" *Geochimica et Cosmochimica Acta* **65**(7): 1059-1070.

Goulty, N. (2003). "Reservoir stress path during depletion of Norwegian chalk oilfields." *Petroleum Geoscience* **9**(3): 233-241.

Guk, V., M. N. Bychina, D. S. Wolcott and M. J. Economides (2014). *A Fracture Injection Test Design and Interpretation for the Determination of Reservoir Permeability*. SPE Annual Technical Conference and Exhibition, Society of Petroleum Engineers.

Gutierrez, M., L. Øino and K. Høeg (2000). "The effect of fluid content on the mechanical behaviour of fractures in chalk." *Rock Mechanics and Rock Engineering* **33**(2): 93-117.

Hagoort, J., B. D. Weatherill and A. Settari (1980). "Modeling the propagation of waterflood-induced hydraulic fractures." *Society of Petroleum Engineers Journal* **20**(04): 293-303.

Havmøller, O., F. Engstrøm, H. Christensen and N. Foged (1996). Project 4.1: Review of Rock Mechanical Data. Joint Chalk Research Phase IV.

Heggheim, T., M. Madland, R. Risnes and T. Austad (2005). "A chemical induced enhanced weakening of chalk by seawater." *Journal of petroleum science and engineering* **46**(3): 171-184.

Hermansen, H., L. Thomas, J. Sylte and B. Aasboe (1997). *Twenty five years of Ekofisk reservoir management*. SPE Annual Technical Conference and Exhibition, Society of Petroleum Engineers.

Hillis, R. R. (2001). "Coupled changes in pore pressure and stress in oil fields and sedimentary basins." *Petroleum Geoscience* **7**(4): 419-425.

Hiorth, A., Ø. Bache, E. Jettestuen, L. M. Cathles, R. W. Moe, E. Omdal, R. Korsnes and M. V. Madland (2011). *A simplified approach to translate chemical alteration in core experiments to field conditions*. Paper SCA2011-09 presented at the International Symposium of the Society of Core Analysts held in Austin, Texas, USA 18-21 September.

Howard, G. C. and C. Fast (1957). *Optimum fluid characteristics for fracture extension*. Drilling and Production Practice, American Petroleum Institute.

Jensen, T., K. Harpole and A. Østhus (2000). *EOR screening for Ekofisk*. SPE European Petroleum Conference, Society of Petroleum Engineers.

Jonhson, J., D. Rhett and W. Siemers (1989). "Rock Mechanics of the Ekofisk Reservoir in the Evaluation of Subsidence." *SPE* **17854**.

Korsnes, R., M. Madland and T. Austad (2006b). "Impact of brine composition on the mechanical strength of chalk at high temperature." *Multiphysics Coupling and Long Term Behaviour in Rock Mechanics. Taylor & Francis, London*: 133-140.

Korsnes, R., S. Strand, Ø. Hoff, T. Pedersen, M. Madland and T. Austad (2006a). "Does the chemical interaction between seawater and chalk affect the mechanical properties of chalk? ." *EUROCK 2006-Multiphysics Coupling and Long Term Behaviour in Rock Mechanics, Taylor & Francis Group, London*.

Korsnes, R. I., M. V. Madland, T. Austad, S. Haver and G. Røsland (2008). "The effects of temperature on the water weakening of chalk by seawater." *Journal of Petroleum Science and Engineering* **60**(3-4): 183-193.

Krivonogov, T. (2016). Eldfisk Subsidence Modelling and Monitoring (Personal Communication), ConocoPhillips.

Liteanu, E., C. Spiers and J. de Bresser (2013). "The influence of water and supercritical CO 2 on the failure behavior of chalk." *Tectonophysics* **599**: 157-169.

Liteanu, E. and C. J. Spiers (2009). "Influence of pore fluid salt content on compaction creep of calcite aggregates in the presence of supercritical CO 2." *Chemical geology* **265**(1): 134-147.

Madland, M. (1999). "Capillary effects in high porosity chalk." *Thesis for the siv. ing. degree. Stavanger University College, Norway*.

Madland, M. (2005). "Water weakening of chalk. A mechanistic study." *Petroleum Engineering. Stavanger, University of Stavanger*.

Madland, M. (2016). Temperature Dependency of Water Weakening in Chalk (Personal Communication). University of Stavanger.

Madland, M., A. Hiorth, E. Omdal, M. Megawati, T. Hildebrand-Habel, R. Korsnes, S. Evje and L. Cathles (2011). "Chemical alterations induced by rock–fluid interactions when injecting brines in high porosity chalks." *Transport in porous media* **87**(3): 679-702.

Madland, M., K. Midtgarden, R. Manafov, R. Korsnes, T. Kristiansen and A. Hiorth (2008). *The effect of temperature and brine composition on the mechanical strength of Kansas chalk*. International Symposium SCA.

Madland, M., A. Nermoen, A. Hiorth, E. Jettestuen, J. Vinningland, T. Hildebrand-Habel, R. Korsnes, S. Evje, J. Pedersen, P. Andersen and W. Wang (2015). JCR7 Final Report, Water Weakening of Chalk at Realistic Reservoir Conditions (unpublished work). Petromaks-Joint Chalk Research Phase VII**:** 348-353.

Madland, M., E. Omdal, H. Breivik, R. Korsnes, A. Hiorth and T. Kristiansen (2009). *Investigation of the Effective Stress Relation for Outcrop Chalk*. Ling HI, Smyth A, Betti R (eds), Poromechanics IV, 4th Biot Conference on Poromechanics. New York, DEStech Publication: 429-434

Madland, M. V., R. I. Korsnes and R. Risnes (2002). *Temperature effects in Brazilian, uniaxial and triaxial compressive tests with high porosity chalk*. SPE Annual Technical Conference and Exhibition, Society of Petroleum Engineers.

McClure, M. W., H. Jung, D. D. Cramer and M. M. Sharma (2016). "The Fracture-Compliance Method for Picking Closure Pressure From Diagnostic Fracture-Injection Tests." *SPE Journal*.

Megawati, M., P. Andersen, R. Korsnes, H. Hiorth and M. Madland (2011). "The effect of aqueous chemistry ph on the time-dependent deformation behaviour of chalk experimental and modelling study." *Pore2Fluid IFP Energies nouvelles Paris, Nov*: 16-18.

Megawati, M., A. Hiorth and M. Madland (2013). "The impact of surface charge on the mechanical behavior of high-porosity chalk." *Rock mechanics and rock engineering* **46**(5): 1073-1090.

Megawati, M., M. Madland and A. Hiorth (2015). "Mechanical and physical behavior of high-porosity chalks exposed to chemical perturbation." *Journal of Petroleum Science and Engineering* **133**: 313-327.

Mondal, S. (2010). *Pressure transients in wellbores: water hammer effects and implications for fracture diagnostics*. Master of Science in Engineering, University of Texas at Austin.

Nagel, N. (1998). "Ekofisk Field Overburden Modelling." *Society of Petroleum Engineers* **SPE 47345**.

Nermoen, A., R. I. Korsnes, A. Hiorth and M. V. Madland (2015). "Porosity and permeability development in compacting chalks during flooding of nonequilibrium brines: Insights from long-term experiment." *Journal of Geophysical Research: Solid Earth* **120**(5): 2935-2960.

Nolte, K. G. and M. B. Smith (1981). "Interpretation of fracturing pressures." *Journal of Petroleum Technology* **33**(09): 1,767-761,775.

NPD. (2016). "Eldfisk." Retrieved March 22nd, 2016, from http://factpages.npd.no/factpages/Default.aspx?culture=no.

Okoroafor, R. E., A. Nkanga, F. Okoli, F. Babatunde, I. Danison and T. Akinnagbe (2015). *From Exploration to Development: The Value of Formation Pressure While Drilling Applications*. SPE Nigeria Annual International Conference and Exhibition, Society of Petroleum Engineers.

Omdal, E. (2010). *The mechanical behavior of chalk under laboratory conditions simulating reservoir operations*. PhD, University of Stavanger.

Omdal, E. (2016a). Stress Magnitudes Ekofisk Overburden Modelling (Personal Communication). ConocoPhillips.

Omdal, E. (2016b). Viscoplastic Deformation of Chalk under Reservoir Conditions (Personal Communication). ConocoPhillips.

Omdal, E., E. Dirdal, K. Ormark, K. Vorland, R. Korsnes, T. Kristiansen, T. Knutsen, T. Hildebrand-Habel and M. Madland (2008). *Induced Geometry in Chalk during Hydrochloric Acid Stimulation*. 3rd International Symposium GeoProc'2008, Wiley.

Omdal, E., M. Madland, H. Breivik, K. Næss, R. Korsnes, A. Hiorth and T. Kristiansen (2009). *Experimental investigation of the effective stress coefficient for various high porosity outcrop chalks*. 43rd US Rock Mechanics Symposium & 4th US-Canada Rock Mechanics Symposium, American Rock Mechanics Association.

Omdal, E., M. Madland, T. Kristiansen, N. Nagel, R. Korsnes and A. Hiorth (2010). "Deformation Behavior of Chalk Studied Close to In Situ Reservoir Conditions." *Rock mechanics and rock engineering* **43**(5): 557-580.

Omdal, E., M. Madland, R. Renli, T. Kristiansen, A. Hiorth, R. Korsnes and T. Hildebrand-Habel (2009). "Laboratory observations with implications for depletion of chalk reservoirs." *Poromechanics IV. DEStech Publications, Lancaster*: 953-958.

Ozoglu-Topdemir, S. (2016). Using Injection Falloffs to Determine Near Well Reservoir Pressure (Personal Communication). ConocoPhillips.

Pong, C., P. Singh, H. Halvorsen and S. York (1992). "Fractured reservoir characterization through injection, falloff, and flowback tests." *SPE formation evaluation* **7**(03): 241-246.

Risnes, R. (2001). "Deformation and yield in high porosity outcrop chalk." *Physics and Chemistry of the Earth, Part A: Solid Earth and Geodesy* **26**(1): 53-57.

Risnes, R., H. Haghighi, R. Korsnes and O. Natvik (2003). "Chalk–fluid interactions with glycol and brines." *Tectonophysics* **370**(1): 213-226.

Risnes, R., M. Madland, M. Hole and N. Kwabiah (2005). "Water weakening of chalk—Mechanical effects of water–glycol mixtures." *Journal of Petroleum Science and Engineering* **48**(1): 21-36.

Risnes, R. and V. Nygaard (1999). "Elasticity in high porosity outcrop chalk." *Second euroconference on rock physics and rock mechanics, Heriot-Watt University, Edinburgh, Scotland*.

Rod, M. and O. Jørgensen (2005). *Injection Fracturing in a Densely Spaced Line Drive Waterflood–The Halfdan Example (SPE94049)*. 67th EAGE Conference & Exhibition.

Røyne, A., K. N. Dalby and T. Hassenkam (2015). "Repulsive hydration forces between calcite surfaces and their effect on the brittle strength of calcite-bearing rocks." *Geophysical Research Letters* **42**(12): 4786-4794.

Schlumberger. (2016). "pressure-transient analysis." Retrieved March 17th, 2016, from http://www.glossary.oilfield.slb.com/Terms/p/pressure-transient_analysis.aspx.

Scholle, P. A. (1977). "Chalk diagenesis and its relation to petroleum exploration: oil from chalks, a modern miracle?" *AAPG Bulletin* **61**(7): 982-1009.

Shchipanov, A. (2014). Advanced PTA/PDG methodology: Potential for Eldfisk on the example of well B-8 B. IRIS**:** 37.

Shchipanov, A., R. Berenblyum and L. Kollbotn (2014). *Pressure Transient Analysis as an Element of Permanent Reservoir Monitoring*. SPE Annual Technical Conference and Exhibition, Society of Petroleum Engineers.

Singh, P., R. Agarwal and L. Krase (1987). *Systematic design and analysis of step-rate tests to determine formation parting pressure*. SPE Annual Technical Conference and Exhibition, Society of Petroleum Engineers.

Snow, S. and M. Brownlee (1989). *Practical and Theoretical Aspects of Well Testing in the Ekofisk Area Chalk Fields*. SPE Annual Technical Conference and Exhibition, Society of Petroleum Engineers.

Terzaghi, K. v. (1923). "Die berechnung der durchlassigkeitsziffer des tones aus dem verlauf der hydrodynamischen spannungserscheinungen." *Sitzungsberichte der Akademie der Wissenschaften in Wien, Mathematisch-Naturwissenschaftliche Klasse, Abteilung IIa* **132**: 125-138.

Teufel, L. and D. Rhett (1991). *Geomechanical evidence for shear failure of chalk during production of the Ekofisk field*. SPE Annual Technical Conference and Exhibition, Society of Petroleum Engineers.

Teufel, L. and D. Rhett (1992). *Failure of chalk during waterflooding of the Ekofisk field: SPE paper 24911, presented at 67th Soc*. Petr. Eng. Ann. Tech. Conf.

Teufel, L., D. Rhett, H. Farrell and J. Lorenz (1993). *Control of fractured reservoir permeability by spatial and temporal variations in stress magnitude and orientation*. SPE Annual Technical Conference and Exhibition, Society of Petroleum Engineers.

Teufel, L. W. (2007). Geomechanics Approach for Characterization and Simulation of Naturally Fracture Reservoirs (Course Material). ConocoPhillips.

Teufel, L. W. and N. R. Warpinski (1990). Laboratory determination of effective stress laws for deformation and permeability of chalk, Sandia National Labs., Albuquerque, NM (USA).

Wade, J., E. Hough, T. Harrington, J. Valdal and S. Pedersen (1998). *Case history of oil well performance monitoring and production optimization in the Eldfisk and Ekofisk Fields, Norwegian North Sea*. SPE International Oil and Gas Conference and Exhibition in China, Society of Petroleum Engineers.

Walls, J. D., J. Dvorkin and B. A. Smith (1998). *Modeling seismic velocity in Ekofisk Chalk*. Society of Exploration Geophysicists Technical Programme and Expanded Abstracts.

Walsh, J. (1981). *Effect of pore pressure and confining pressure on fracture permeability*. International Journal of Rock Mechanics and Mining Sciences & Geomechanics Abstracts, Elsevier.

Warpinski, N. and L. Teufel (1987). "Influence of geologic discontinuities on hydraulic fracture propagation (includes associated papers 17011 and 17074)." *Journal of Petroleum Technology* **39**(02): 209-220.

Zangiabadi, B., R. Korsnes, T. Hildebrand-Habel, A. Hiorth, I. Surtarjana, A. Lian and M. Madland (2009). *Chemical water weakening of various outcrop chalks at elevated temperature*. Poromechanics IV: Proceedings of the 4th Biot Conference on Poromechanics.

Zimmermann, U., M. V. Madland, A. Nermoen, T. Hildebrand-Habel, S. A. Bertolino, A. Hiorth, R. I. Korsnes, J.-N. Audinot and P. Grysan (2015). "Evaluation of the compositional changes during flooding of reactive fluids using scanning electron microscopy, nano-secondary ion mass spectrometry, x-ray diffraction, and whole-rock geochemistry." *AAPG Bulletin* **99**(5): 791-805.

Zoback, M. D. and J. C. Zinke (2002). Production-induced normal faulting in the Valhall and Ekofisk oil fields. *The Mechanism of Induced Seismicity*, Springer**:** 403-420.

8 Appendix

8.1 Appendix A: Eldfisk Bravo Structure Map

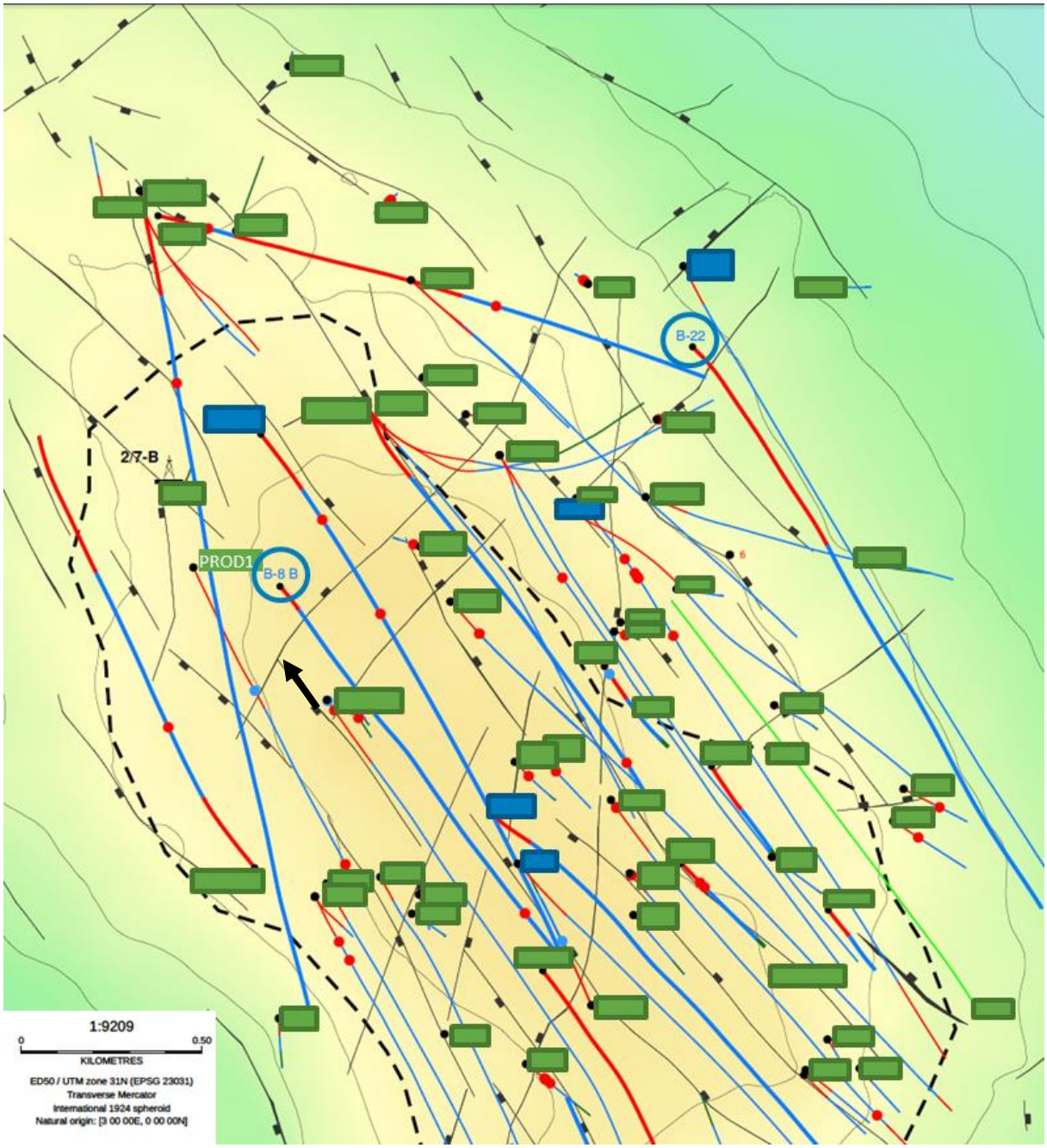

Figure 8.1: Map of the Eldfisk Bravo structure (Figure 1.1, Section 1.3.2). The map is near top chalk. Producers are marked in green, injectors in blue. Blue well tracks are in the Tor Formation, red well tracks in the Ekofisk Formation. The two studied injectors in this thesis are B-8 B and B-22, which are highlighted on the map. PROD1 to the west of B-8 B collapsed after a major water breakthrough from B-8 B. This is understood as water injection from B-8 B entering the fault connection the two wells (marked with a black arrow).

8.2 Appendix B: B-8 B CPI

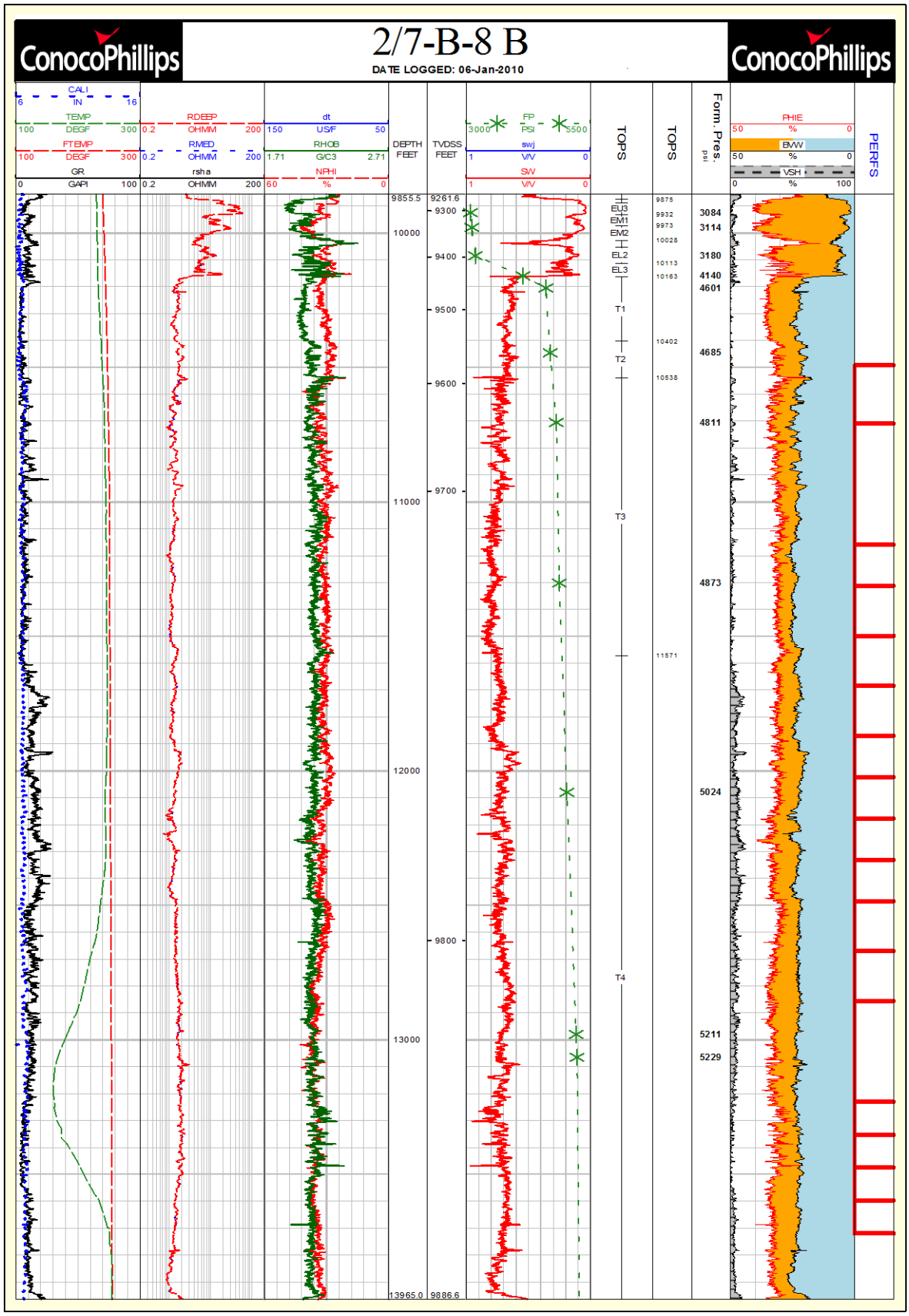

Figure 8.2: B-8 B CPI (ConocoPhillips, 2016). Formation nomenclature: T1-4 (Tor Formation), EL1-3 (Lower Ekofisk Formation (EL)), EM1-2 (Middle Ekofisk Formation (EM)) and EU1-3 (Upper Ekofisk Formation (EU)).

8.3 Appendix C: B-22 CPI

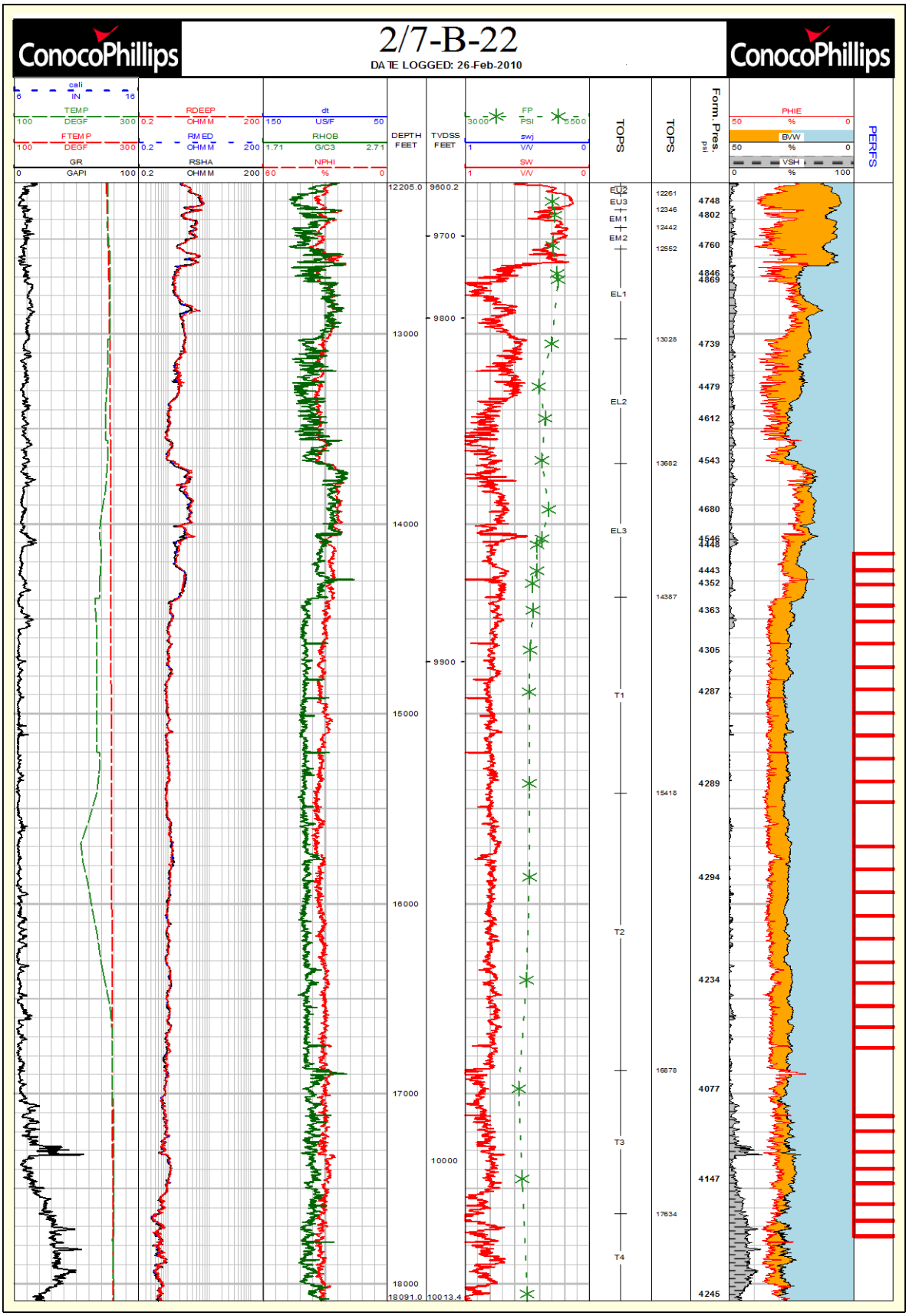

Figure 8.3: B-22 CPI (ConocoPhillips, 2016). Formation nomenclature: T1-4 (Tor Formation), EL1-3 (Lower Ekofisk Formation (EL)), EM1-2 (Middle Ekofisk Formation (EM)) and EU1-3 (Upper Ekofisk Formation (EU)).